This electronic thesis or dissertation has been downloaded from the King's Research Portal at https://kclpure.kcl.ac.uk/portal/

KING'S College LONDON

Directly Estimating the 3-D Orientation of Single Fluorescent Molecules by Defocused Optical Microscopy

Kwakwa, Kwasi Amoako

Awarding institution:
King's College London

The copyright of this thesis rests with the author and no quotation from it or information derived from it may be published without proper acknowledgement.

END USER LICENCE AGREEMENT

Unless another licence is stated on the immediately following page this work is licensed

under a Creative Commons Attribution-NonCommercial-NoDerivatives 4.0 International

licence. https://creativecommons.org/licenses/by-nc-nd/4.0/

You are free to copy, distribute and transmit the work

Under the following conditions:

- Attribution: You must attribute the work in the manner specified by the author (but not in any way that suggests that they endorse you or your use of the work).
- Non Commercial: You may not use this work for commercial purposes.
- No Derivative Works - You may not alter, transform, or build upon this work.

Any of these conditions can be waived if you receive permission from the author. Your fair dealings and other rights are in no way affected by the above.

Take down policy

If you believe that this document breaches copyright please contact librarypure@kcl.ac.uk providing details, and we will remove access to the work immediately and investigate your claim.

Download date: 06. May. 2023

Directly Estimating the 3-D Orientation of Single Fluorescent Molecules by Defocused Optical Microscopy

Kwasi Amoako Kwakwa
of King's College London

A dissertation submitted to the King's College London
for the degree of Doctor of Philosophy

Abstract

Defocused wide field fluorescence imaging is a relatively simple procedure for measuring the 3-D orientation of single fluorescent molecules illuminated via wide-field illumination and imaged through a slightly defocused ($\approx 1\,\mu m$) high NA objective unto a highly sensitive CCD camera.

The technique relies on the anisotropic nature of the photon distribution emitted by a fluorophore. This distribution is best described by the shape of the electromagnetic field produced by a vibrating electric dipole. The imaged intensity pattern can therefore be modelled in terms of the field produced by an arbitrarily oriented dipole close to the interface between two materials with differing refractive indices and then imaged by a defocused objective. A least-squares fitting routine is then applied to match experimentally obtained patterns with their closest fitting computationally predicted counterparts to arrive at the best estimate for the 3D orientation of the fluorophore (usually $\pm$ 2.5° for the majority of the experiments performed in this thesis). Since the pattern fitting algorithm also locates the central pixel of the matched pattern, a welcome side effect of determining the molecular orientation by this technique is to provide superresolution position estimation of the fluorophores to within the space represented by a single pixel. A discussion of ways to make the algorithm more precise is also included.

The project documented in this thesis begins with the construction of a microscope system capable of reliably imaging single fluorescent molecules. The system and the technique are both then simultaneously validated by being applied to obtain the orientations of single fluorescent molecules embedded in polymer and lipid thin films.

Experiments and simulations are also performed to quantify the physical limits of the technique in order to understand the level of uncertainty inherent in all the obtained measurements. The simulations showed that for a system with injected background noise, the signal only needs to be 3%-5% of the noise to produce position information accurate to 1 pixel and orientation information accurate to $\pm 5°$.

A means of acquiring the defocused patterns from single molecules in relatively densely labelled samples is proposed, verified on a dense sample of dye molecules embedded in PMMA and then applied to lipid nanostructures produced by Dip-Pen Nanolithography densely labelled with rhodamine-functionalized lipids. The results show a preferential polar angle orientation similar to existing predictions, and suggest a possible horizontal orientation in line with the direction of creation of the nanostructures. A variation of the technique is also applied to validate the superresolution position estimation properties of the technique, isolating molecules to within a 64 nm $\times$ 64 nm pixel.

A proof-of concept experiment is also performed to show the possibility of imaging the orientations of single $DilC_{18}(3)$ molecules embedded in cell membranes. The molecules show preferential orientation close to the horizontal plane, as is predicted by other approaches.

Acknowledgements

In completing this project, I have had a lot of help from several people I would like to thank. Primarily my advisors Professor David Richards and Dr. Deb Roy for their advice and support throughout the project and Professor Jörg Enderlein for his advice and the use of his MATLAB pattern generation and recognition program.

Additionally, the National Physical Laboratory funded my PhD and provided the lab and equipment used in all my experiments. I would like to specifically thank Dr. Alex Knight for advice, encouragement and direction, Dr. Jascindra Ravi and Dr. Paulina Rakowska for their assistance with the process of creating lipid bilayers, Nilofar Farqui for culturing cells, Naresh Kumar for the general cheer and encouragement he provided. Additionally, I would like to thank Dr. Helen Sharman as well as the Surface Analysis and Biotechnology teams at NPL for making my 3 years with them a pleasure.

Dr. Michael Hirtz of the Karlsruhe Nano Micro Facility also donated his time and expertise to provide me with nanoscale lipid bilayer structures for my research, for which I am very grateful.

I'd also like to thank Dr. Mark Green for providing me with quantum dots and the Experimental Biophysics & Nanotechnology group at King's College London for listening and asking good questions when I needed them.

"Kwasi and Sylvia Kwakwa, Kwabena Kwakwa, the Danquahs and the Tagoes for all the support and encouragement. Thanks for not giving up on me"

Contents

List of Abbreviations

APD Avalanche Photodiode, page 3

CCD Charge Coupled Device, page 3

DilC 1,1′-dioctadecyl-3,3,3′, 3′-tetramethylindocarbocyanine perchlorate, page 59

DOPC 1, 2-Dioleoyl-sn-glycero-3-phosphocholine, page 88

DPPC (1, 2-dipalmitoyl-sn-glycero-3-phosphocholine), page 73

DPPE 1,2- dipalmitoyl-sn-glycero-3-phosphoethanolamine, page 88

FIONA Fluorescence Imaging with One Nanometre Accuracy, page 14

LED Light Emitting Diode, page 3

NA Numerical Aperture, page 28

PALM Photoactivated Localization Microscopy, page 6

PMMA Poly(methyl methacrylate), page 59

R6G ethyl 2-[(6Z)-3-ethylamino-6-ethylimino-2,7-dimethyl-xanthen-9-yl]benzoate hydrochloride, page 88

SNOM Scanning Near-Field Optical Microscopy, page 6

SPAD Single-Photon Avalanche Diode, page 22

STED Stimulated Emission Depletion microscopy, page 21

STORM Stochastic Optical Reconstruction Microscopy, page 6

TIRF Total Internal Reflection Fluorescence, page 6

Chapter 1.

Introduction

There are several competing accounts of who created the first compound microscope, including Galileo Galilei, Hans Lippershey and Zacharias and Hans Jansen. Regardless of who its original inventor was, the invention of the microscope led to Antoine Van Leeuwenhoek making the first observations of individual cells, thereby inventing the field of optical microscopy. Ever since then, optical microscopes have been used to enhance the abilities of the human eye to observe phenomena too small to be seen by the naked eye. Microscopy has become an incredibly necessary part of the toolkit of techniques used to understand the behaviour of nature on the small scale. While it has undergone substantial technical improvements since then, especially with the introduction of fluorescent markers, it still remains an important way to nondestructively observe the very small.

1.1. Fluorescence Microscopy

About a century and a half after the invention of the microscope, the first recorded discovery of fluorescence was by John Herschel in 1845. He observed a glass full of quinine solution glow faintly when exposed to sunlight, especially in the blue part of the spectrum. The phenomenon of fluorescence was then named and described in detail by Stokes in 1852[1] and then Jablonski in 1933. Further experimentation into the nature of fluorescence resulted in the development of fluorescent dyes,

beginning with the discoveries of Nichols and Merrit.[2] This discovery quickly led to the combination of fluorescent dyes and optical microscopes to create the field of fluorescence microscopy.

In its simplest form, fluorescence microscopy involves the use of specific fluorescent dyes to stain objects that are under investigation. The dyes are then excited by a light source that emits in the range of wavelengths they absorb.Light sources are generally lasers, Light Emitting Diodes (LEDs) or mercury lamps. Optical filters are then used to separate the excitation light from the longer wavelength light emitted by the dyes as they fluoresce. The fluorescence is then recorded by means of highly sensitive detectors (Photomultiplier Tubes(PMT), several kinds of Charge Coupled Devices (CCD) or Avalanche Photodiodes (APD)). The captured light allows the stained objects to be examined in great detail. An example of fluorescence imaging can be seen in Figure 1.1.

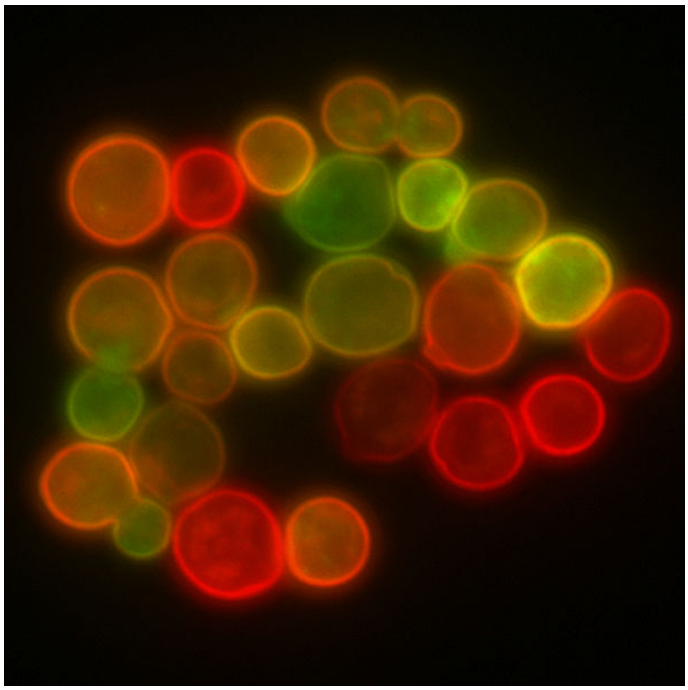

Figure 1.1.: An example of fluorescence microscopy used to image yeast cells with fluorescent molecules embedded in their membranes[3]

Fluorescent dyes have been used to image cell structures, polymers, lipids,[4] solid surfaces and individual protein molecules.[5] Examining the polarisation of

the fluorescence can also be used to probe the bulk viscosity of the medium that has been stained with the dye.[2]

1.1.1. The Physics of Fluorescence

The phenomenon of fluorescence occurs in molecules that have electrons in bonds or orbitals where there is an energy gap between the Highest Occupied Molecular Orbitals (HOMO) and the Lowest Unoccupied Molecular Orbitals (LUMO) that is of the magnitude of the energy of a photon of visible light. This will result in photons of the appropriate energy being absorbed by that electron which will then be promoted to the higher orbital. Part of the energy is generally lost in non-radiative processes in the molecule, meaning that when the electron decays back to its ground state and releases a photon, that radiated photon will have lower energy than the absorbed photon.[6] This can be illustrated in Figure 1.2. Fluorescence usually occurs on time scales in the ≈1 ps - 1 µs range.[7]

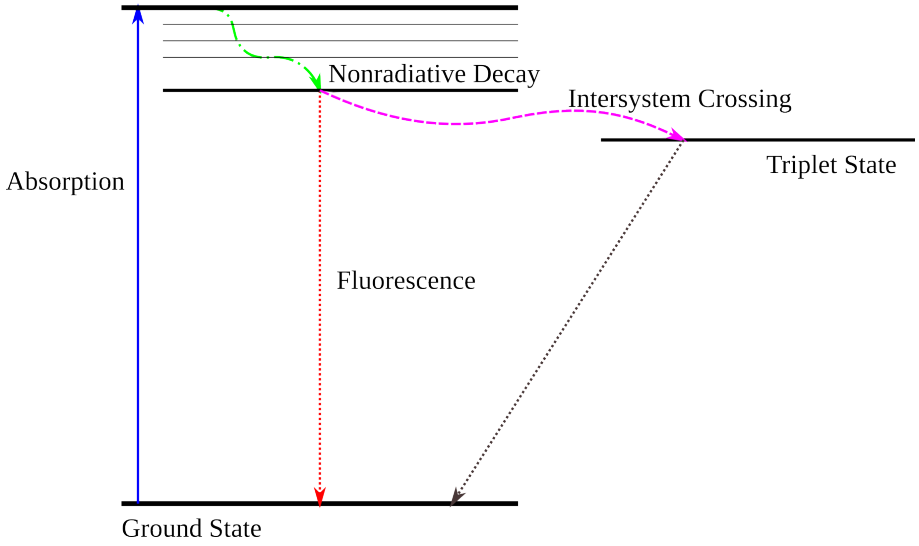

Figure 1.2.: A Jablonski diagram showing photon absorption, nonradiative decay and fluorescence as well as the alternative pathway back to the ground state through a triplet state. Fluorescence occurs on nanosecond time scales while phosphorescence occurs on millisecond - second time scales.

It is also possible, but significantly less statistically likely, that the excited electron will, in the process of nonradiative decay, transition to a lower energy state where its spin changes. In that case, it will no longer be able to directly return to its ground state. This results in the formation of a triplet state from which the electron eventually decays back down to the ground state. If it does so radiatively, the resulting photon emission is characterised as phosphorescence rather than fluorescence.[6] Because radiative decay from a triplet state to the ground state is statistically less likely, phosphorescence tends to occur on far slower time scales than fluorescence (between $\approx$1 ms and 1 s). This can also be seen in Figure 1.2. The time between excitation and emission provides an intrinsic limit on the number of photons that can be emitted by a molecule in a given time. Also, the molecule's surroundings (solvent in which it is dissolved, molecules to which it is attached) can affect the conformation of the molecule and thus the relative energies of its orbitals. This can in turn affect the rate at which fluorescent molecules emit photons and how long it takes for them to be bleached out.

1.1.2. Single Molecule Fluorescence

While standard fluorescence microscopy remains an important technique, there are limitations to staining samples densely with fluorescent markers. In a lot of cases the information obtained that way represents an averaging of spatially and temporally distributed changes taking place all over the stained sample, which may appear homogeneous but be a lot more complex on a smaller scale. By observing the fluorescence of single molecules, it becomes possible to observe changes confined to single molecules or volumes of a few cubic nanometres. The need for higher resolution information of this kind led to the creation of single molecule fluorescence spectroscopy.

The first single molecule detection experiment involved the detection of the absorption spectrum of single pentacene molecules embedded in a p-terphenyl crystal cooled by liquid Nitrogen.[8] A year later, the same experiment was performed on a similar system, but at room temperature.[9] Single molecule emission detection started with the use of confocal microscopy to observe the fluorescence of

picomole concentrations of dye molecules in microfluidics systems.[10] Afterwards, there seemed to be an explosion of single molecule measurements by means of confocal microscopy, Scanning Near-Field Optical Microscopy (SNOM), prism and objective Total Internal Reflection Fluorescence (TIRF), and wide field illumination (all illustrated in Figure 1.3).[11] A large part of what has made especially wide field single molecule fluoresce detection possible has been the improvements in the types of CCD cameras and their sensitivity to the incredibly low number of photons emitted by single fluorophores.[12]

In the years since single molecule fluorescence spectroscopy became a more widespread part of the microscopy toolkit, it has has seen a wide variety of uses. This includes investigating the behaviour of individual dye molecules in different media to track differences in fluorescence lifetime, changes in spectrum and quantum yield.[13,14] It has also been used to track changes in molecule position in cell membranes[15,16] and polymers.[17–19] Additionally, tracking changes in the fluorescence lifetimes of two close (less than 10 nm) dye molecules by Förster Resonance Energy Transfer (FRET) can allow the use of single molecule fluorescence to provide precise distance measurements ($<$10 nm) between the two fluorescent molecules and the structures they are attached to.[13]

One of the most interesting advances in single molecule spectroscopy has been the ability to sidestep Abbe's diffraction limit and locate single fluorescent molecules at distances on the order of tens of nanometres or less rather than a spot of light with diameter $\approx$300 nm. There are several methods used to isolate the fluorescence from a single molecule in a densely labelled sample (Photoactivated Localization Microscopy (PALM), Stochastic Optical Reconstruction Microscopy (STORM) and their derivatives), but the location estimation is achieved by fitting a 2D Gaussian curve to the diffraction limited spot produced by the fluorophore in order to estimate the centre of the spot.[20] The ability to more accurately track changes in molecule position can be used to estimate the localised viscosity of the material/fluid it s embedded in. By attaching dye molecules to other single molecules, we can then track the changes in position of those molecules they are attached to.[21] Several reviews of single molecule fluorescence exist and can provide more details.[20,22–24]

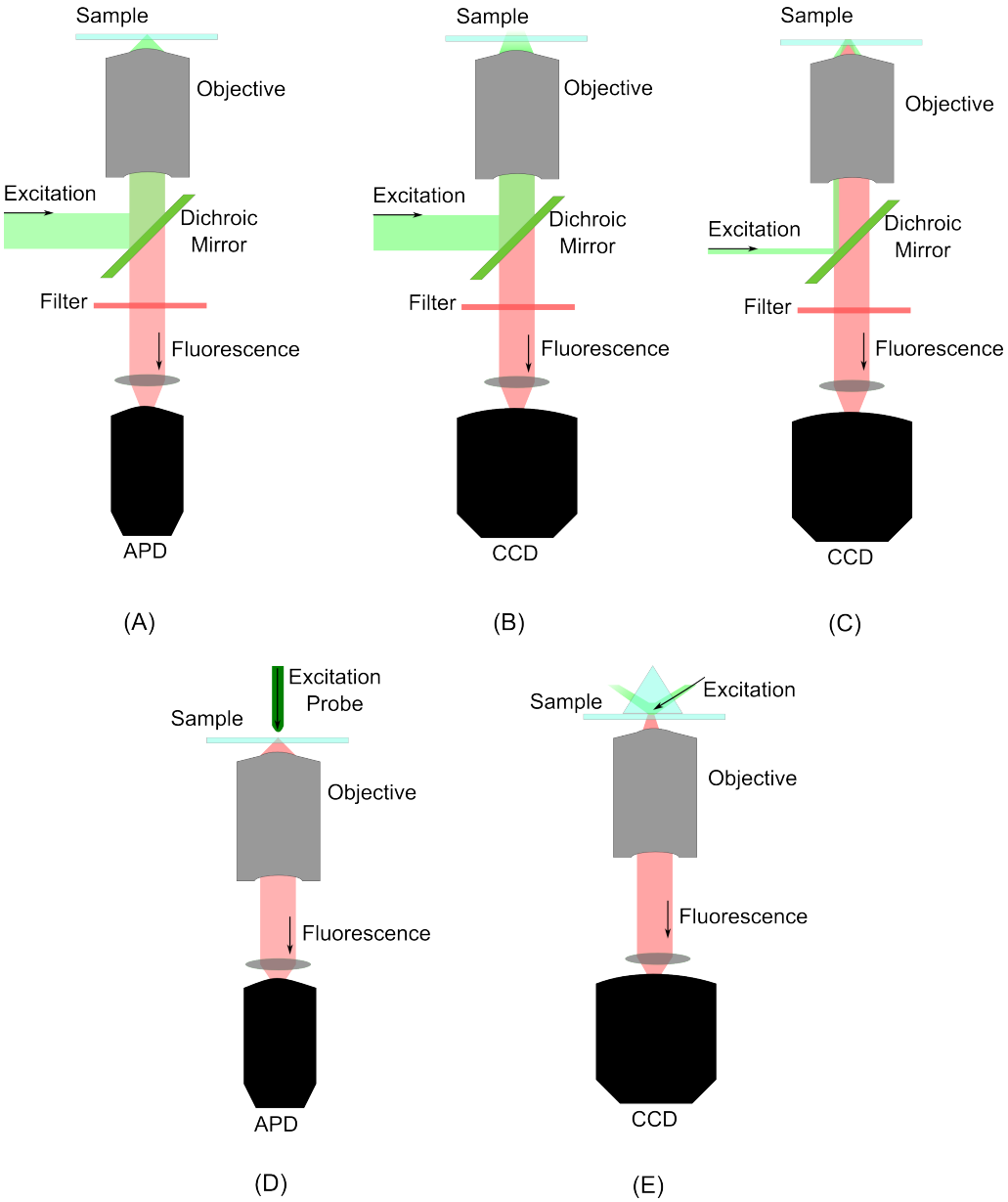

Figure 1.3.: Various system setups for single molecule fluorescence systems. (A)Confocal Fluorescence, (B)Wide-Field fluorescence, (C)Objective TIRF, (D)Near-Field Fluorescence, (E)Prism TIRF

1.1.3. Single Molecule Orientation

In summary, the process of improving the amount of information we can obtain from tagging materials with fluorescent dyes has now led to single molecule microscopy techniques. They are built around tracking the position and intensity of single dye molecules to provide more spatially and temporally fine grained information about their surroundings. The next logical step in obtaining more information is to develop the ability to track changes in the 3D orientation of dye molecules. This provides us with an extra piece of information from single molecule observations. Changes in orientation can be indicative of localised differences in viscosity or ordering in the immediate vicinity of the probe molecules. In cases where the dye is fixed to another molecule, the changes in orientation can be used to track changes in molecular conformation that may be occurring with too little lateral movement to be tracked any other way.

Naturally, due to the diffraction limit, it is impossible to directly observe changes in molecular orientation. Dye molecules are 2-3 orders of magnitude smaller than the diffraction limited spots that can be directly observed, making any attempts to extract orientation data without the use of x-rays or electron guns impossible using the previously discussed techniques.

This thesis is focused around what I have judged to be the most interesting and promising approach to determining the orientation of single fluorescent molecules, namely via analysing the spatial intensity distribution in the defocused fluorescence patterns produced by single molecules. My aim is to create a system capable of performing this measurement and then attempt to apply it to some interesting systems. At the same time, I also plan to investigate the limitations of the technique so it can be better understood on a more fundamental level.

1.2. Thesis Outline

In Chapter 2 the technique of defocused fluorescence imaging for orientation measurement shall be introduced and fully explained. All the available literature

shall also be reviewed covering all of the ways it has been used and what its known limitations are. In order to explain why this technique was chosen, a review shall also be performed of all the other existing approaches to measuring the 3D orientation of single molecules. For all of the techniques, I shall discuss the principles behind them, how they have been used and their limitations.

In the Chapter 3, a detailed overview shall be provided of the theoretical basis behind defocused wide-field fluorescence determination. The classical electrodynamics framework behind predicting the intensity pattern formed on a camera by a single defocused fluorophore will be explained in full. An overview shall also be provided of the pattern matching algorithm used to match the theoretical predictions to those obtained experimentally.

As a result of defocused fluorescence orientation measurement being a fairly recent technique, very little work has been done on its physical limitations. Questions about the the minimum number of photons required to provide an accurate image, the accuracy of the finally determined position and orientation data etc. have not yet been examined in anything approaching a comprehensive fashion. Since the work for this thesis is being performed in a metrology lab, and these are all questions that must be answered to determine the reliability of any obtained data, this chapter shall also include an attempt to improve on the body of knowledge in this area by modelling the experimental system computationally and examining all its possible parameters.

Since a substantial part of this project involved the construction of a new microscope system, Chapter 4 shall be a description of the microscope and all its attached parts after construction. A detailed description shall also be provided of software used to control the camera, lasers and attached hardware as well as acquire and analyse data.

Chapter 5 deals with experiments performed on thin film samples. The first step involves the validation of both the imaging system and the technique by measuring the orientation of single fluorophores embedded in polymer thin films and continuous synthetic lipid bilayer films. While measuring the orientation of thin films, the opportunity was also taken to compare different modes of illumination

and beam polarisation. The results obtained here are primarily meant to show that all the hardware and software are in working order, but also manage to be interesting in their own right. Next, I experimentally estimate reasonable integration times for producing easily detectable samples with low error levels. Finally a novel illumination and imaging system for acquiring orientation information with shorter integration times is proposed and investigated experimentally.

The technique is then modified in Chapter 6 for imaging the orientations of individual molecules in samples so densely labelled that the light from individual molecules overlap and therefore can not be individually isolated. This modification is adapted from existing single molecule techniques and then tried out on densely labelled polymer thin film samples to confirm that it works. Afterwards it is applied to imaging the orientations of fluorescent molecules embedded in nanoscale lipid bilayer structures constructed using Dip-Pen Nanolithography.

The superresolution position estimation capability of the technique is also investigated in Chapter 7. Here samples are created specifically for the purpose of confirming the technique's ability to provide an estimate for the location of fluorescent molecules that occupies a space smaller than that of the diffraction limit.

In Chapter 8, the first recorded defocused fluorescence measurements are made of dye molecules embedded in cell membranes. This is done primarily as a proof of concept to show that it is possible to make these measurements, since the majority of the work that has been done in literature involves the application of defocused fluorescence orientation measurement to various forms of thin films.

In Chapter 9, possible directions for further research that have come to light as a result of the work contained in this thesis shall be discussed. Some speculations concerning the nature of the technique and its possible limitations shall also be discussed.

Chapter 2.

Defocused Fluorescence Orientation Imaging

2.1. Introduction

The idea behind defocused orientation imaging involves measuring the orientations of single fluorescent molecules by calculating their defocused intensity patterns. Those patterns are produced by performing wide field fluorescence imaging on them with a slightly defocused objective. They are then compared to predicted patterns created from a theoretical model of the light produced by single fluorescent molecules. This idea was first proposed by Bohmer and Enderlein.[25] The technique relies on the fact that single fluorescent molecules do not emit light evenly in all directions, but rather their intensity patterns can be modelled in terms of the electromagnetic field distribution produced by a single dipole. By calculating how the uneven intensity would appear on a camera after being imaged through a defocused, high NA objective unto the pixels of a camera, it is possible to predict what patterns will be produced by molecules of varying orientations. These predictions can then be compared to the patterns produced experimentally by imaging single molecules and the results are used to predict the orientations of those fluorophores.

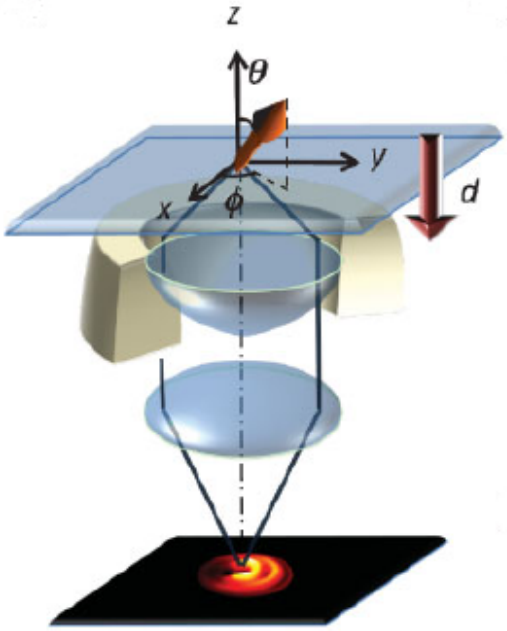

Figure 2.1.: Figure of defocused fluorescence equipment setup. θ and ϕ represent the 3D orientation of the emitting dipole and d represents the distance by which the objective is moved towards the sample[26]

Bohmer and Enderlein first imaged a dilute solution of Cy5 dye spin-coated on a glass cover slip and illuminated using circularly polarised laser light normal to the surface of the cover slip (Experimental setup shown in Figure 2.1, example of results shown in Figure 2.2). The fluorescence image was defocused by moving the objective a specific distance (usually $\approx$1 µm) closer to the object. The defocusing is necessary because it spreads the photons from the dipole over a large enough area of the CCD camera ($\approx$1 µm in diameter) to make the pattern distinguishable. Gathering enough photons from the fluorescence to produce proper images took $\approx$3 s. A least squares pattern fitting algorithm was then employed to match the calculated patterns to those obtained experimentally. The exact pattern matching algorithm was designed by Patra, Gregor and Enderlein.[27,28]

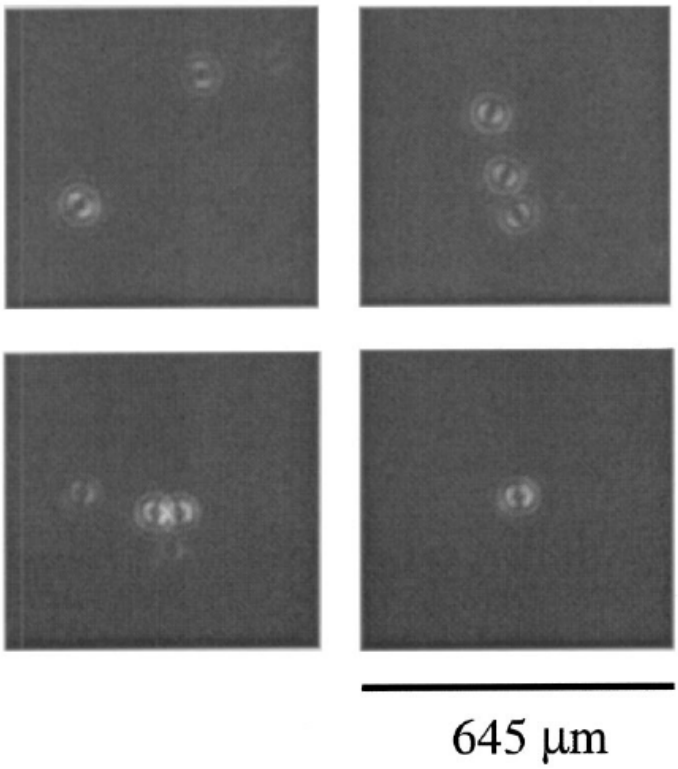

Figure 2.2.: Defocused fluorescence image of single Cy5 dye molecules immobilized in air on a glass surface. The objective was defocused by 1 µm towards the slide and the image was captured for 3 s[25]

2.1.1. Applications

In the 9 years since it was proposed, defocused fluorescence imaging has been used to measure the orientation of single fluorophores in several systems in order to measure various properties. The first and probably most common use of defocused fluorescence imaging is in examining the behaviour of polymer thin films. This has been achieved by embedding low levels of dye ($\approx 1 \times 10^{-10}$ mol) in PMMA layers at different temperatures and then observing changes in orientation at different temperatures to observe the heterogeneous nature of changes in viscosity by speed of rotation of those molecules.[29,30] The ordering of those PMMA layers has also been investigated by comparing the orientation of embedded dye molecules before and after annealing.[31] The same kinds of experiments have also been performed using dye-labelled polymer molecules.[32,33] In that case, the changes of orientation

of dye molecules directly tracks the movement of the polymer chains they are attached to. The ordering of individual chains in organic electronic thin films is also investigated to quantify their effectiveness.[34,35]

Another common use is to examine the characteristics of synthetic lipid monolayers and bilayers. The ordering of these lipid structures is investigated for different kinds of dye molecules, both attached to lipid molecules or just introduced into the layer. Ordering is also investigated for lipid layers with different sterol molecules introduced at different concentrations.[36–38] Fluorescent molecules are also used to mention the order of lipid monolayers in order to confirm that they are not changed drastically by vapour depositing a thin layer of polymer over the monolayers to keep them safe.[39]

Defocused imaging has also been used in conjunction with FIONA (Fluorescence Imaging with One Nanometre Accuracy) to simultaneously image the position and orientation of molecular motors.[40] This has been applied to Rhodamine labelled myosin-VI molecules[41] and quantum dot labelled myosin-V molecules.[42,43] By focusing the image to measure position, and then immediately defocusing the image to measure orientation, the movements of the molecular motors can be very accurately tracked.

Two-colour defocused fluorescence imaging has also been used to examine the mechanics of how the relative orientation of two different molecules affects Förster Resonance Energy Transfer (FRET) at the single molecule level.[44] Since the relative orientations of the donor and acceptor molecules is predicted to affect the rate of energy transfer between them at $<10\,\text{nm}$ distances, this experiment allows more precise measurements of relative orientation and fluorescence lifetime.

In addition to fluorescent molecules, several people have performed proof of concept experiments to show that defocused imaging can be applied to both quantum dots[45–47] (as shown in figure 2.3) and metal nanorods.[48,49] In both cases, the new markers can be imaged as a single dipole (nanorods) or a combination of orthogonal dipoles (quantum dots). Chiral fluorescent molecules are also shown to be made up of multiple emission dipoles, in this case, two orthogonal dipoles.[50]

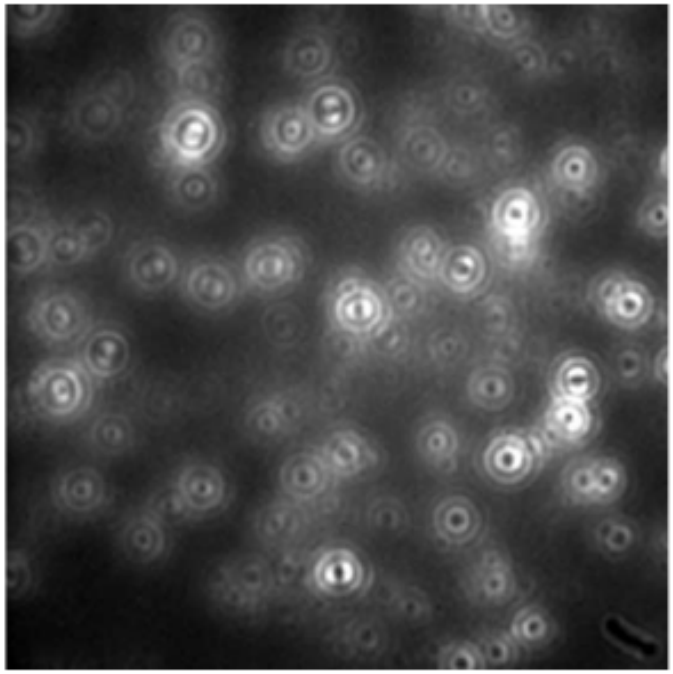

Figure 2.3.: Defocused (≈750nm) fluorescence image of single quantum dots[46]

2.1.2. Limitations

There does not appear to be anything resembling a significant amount of error analysis done with respect to defocused fluorescence orientation imaging in any of the literature, beyond assurances about the error in the measurement of orientation. The closest thing to analysis is the assertion that there is an uncertainty of 10°-15° for an exposure time of 0.6 s.[42] There is no explanation provided for that assertion though, it is simply presented as fact. Across all the experiments performed, time taken to acquire an image has varied between 50 s[50] and 200 ms[29]

There has been no real discussion of what would constitute either the ideal defocus distance or pixel size to image the fluorophores. This is important because some defocusing is necessary to produce distinct patterns for imaging, but the larger the defocus distance, the larger the area the photons from the molecules are distributed over and thus the longer it takes to create clear images. A similar issue exists with pixel size. A smaller effective pixel size makes the patterns easier

to distinguish, but also distributes photons over more pixels and again increases integration time. Defocus distances have ranged between 500 nm-1000 nm. Pixel sizes are rarely mentioned, but since the objectives in all the discussed experiments have 100× magnification, and some of them then used beam expanders further magnify the images, we can reasonably assume pixel sizes between 40 nm and 160 nm.

2.2. Other Approaches to Defocused Fluorescence Imaging

Several other methods of determining the orientation of single fluorescent molecules have been attempted in the past. Since this project clearly made a choice among them, it is worth examining all the other attempts that have been made in order to better understand this technique appeared to be the best possible approach to measuring orientation. Much like defocused fluorescence imaging, they all make use of the model of a fluorescent molecule as an anisotropic electromagnetic field produced by a vibrating dipole. Since the polarisation and spatial distribution of the field is anisotropic, it provides a means of detecting the orientation of the fluorophores.

All the detection methods that have been attempted fall into three main categories:

Polarisation Uses the polarisation of the fluorescence emitted by single molecules to determine their orientation

Scanning Fluorescence Imaging Scanning fluorescence imaging of a single molecule and using the pattern to determine the molecule's orientation.

Intensity Patterns Other techniques for imaging the intensity pattern of the fluorescence from a single molecule to determine its orientation.

2.2.1. Polarisation

Fluorescence Polarisation Microscopy is a technique for measuring the bulk orientation and rotation of fluorescent molecules by observing the changes in the bulk fluorescence emitted by a dye-labelled sample over time by measuring the intensity of the polarisation in two orthogonal directions using a polarising beamsplitter and two CCD cameras.[51] It works primarily because the emission dipole of a fluorophore affects the polarity of the light that it produces when excited. A class of analogous techniques have been proposed and applied to determining the orientation dynamics of single fluorescent molecules.

In-plane single molecule polarisation is measured by first using a laser beam focused unto a diffraction limited spot to excite a single molecule. The emitted fluorescence is then separated using polarising beamsplitters and the fluorescence intensity of each beam read by an avalanche photodiode. An example of the setup can be seen in Figure 2.4. More complicated setups have been proposed and implemented for extracting z-axis orientation information from the molecules. There are also proposed systems that use wide field illumination and sensitive CCD cameras in place of confocal illumination and APDs.

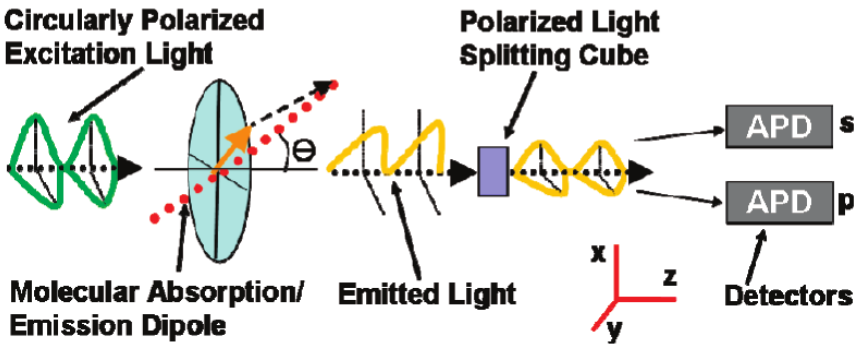

Figure 2.4.: Experimental setup for single molecule polarisation experiments[52]

Applications

As usual, one of the first and most consistent uses of this technique has been to investigate the behavior of polymer thin films, an example being the embedding of Rhodamine molecules in a PMMA thin film in order to observing changes in orientation at the glass transition temperature.[53,54] It has also been used to characterise polymer brushes and glycerol cooled to near its glass transition point by observing the spatial and orientational changes in dye molecules as they diffuse through them.[52,55] Single molecule polarisation has also been applied to track the changes in orientation orientation of fluorescently labelled myosin[56] and kinesin[57] molecules. All of these techniques primarily provide in-plane orientation.

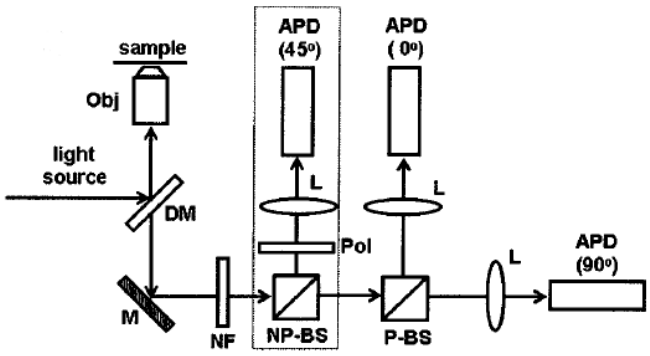

Figure 2.5.: Example of three-angle polarisation experiment setup with epifluorescence confocal scheme. The excitation light and the fluorescence collected by an objective (Obj) are separated by a dichroic mirror (DM). The fluorescence then passes through a mirror (M), and a notch filter (NF) and is then consecutively split by a nonpolarising (NP-BS) and a polarising beam splitter (P-BS). The linear polariser (Pol) is set at 45°. Each beam is finally focused by a lens (L) onto the APD detector[58]

One of the first attempts to expand single molecule polarisation imaging techniques to provide 3D information is by Fourkas et.al.[59] They suggest the use of beam splitters and polarisers to direct light at 0°, 45°, 90° and 135° into avalanche photodiodes to measure intensity at each of those polarities. A modified version of that system can be seen in Figure2.5. It only uses polarisers at 0°, 45° and 90° in order to provide the needed information. It claims the technique will allow for the monitoring of molecules at time scales approaching $\approx$100 µs. There is then some

analysis of the expected intensity to be observed relative to the orientation of the molecules. This system has been applied to examine the orientation of quantum dots, claiming to be able to create full frames at 16Hz.[60] A variation of the system proposed by Fourkas is also proposed that simply adds an annular beam splitter to the classical system for measuring the intensity of fluorescence produced at large angles (pictured in Figure 2.6) and then applied experimentally to a standard test system of single molecules immobilised on glass cover slips.[61,62]

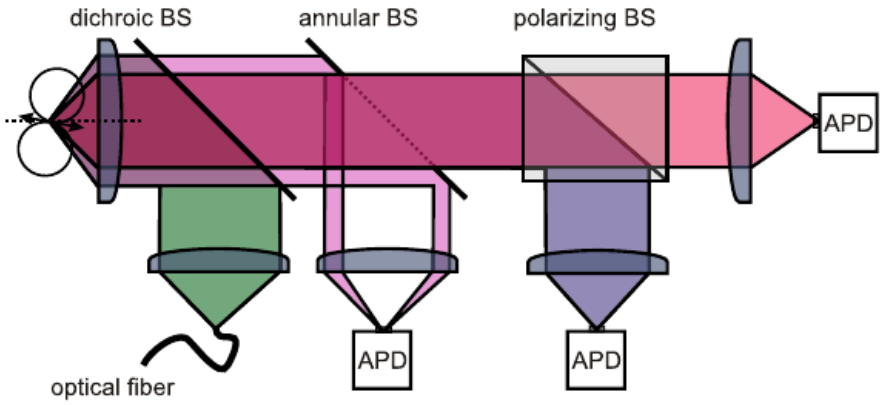

Figure 2.6.: Another proposed experimental setup for single molecule polarisation measurement. An annular beam splitter is used to isolate fluorescence produced at wide angles while a polarising bean splitter separates the 0° polarised light from the 90° polarised light before focusing them unto APDs[62]

In addition to the systems that were experimentally tested, there have also been several proposals for more complicated systems that would be capable of providing better 3-D orientation information, generally by utilising more complicated setups to provide finer-grained measurements of the polarisation produced by a single fluorophore.[63–66] A substantial amount of error analysis was also performed on these systems.

Limitations

For experimental measurements, the time required to obtain a single intensity reading was reported as between 20 ms and 2 s. The theoretical treatments of proposed systems claim to be able to reduce the integration time by several orders

of magnitude to a few hundred microseconds, but at the moment the expected time advantage over defocused imaging is at best an order of magnitude.

Lu and Vanden Bout[58] simulate the setup shown in Figure 2.5 with the fluorescence light split up along 0°,45° and 90° and each fed into a separate avalanche photodiode. The reconstruction algorithm proposed by Fourkas is then used to investigated using this method to discover its possible strengths and shortcomings. Shot noise is also added to the simulation in order to get a more accurate feel for the characteristics of the technique. The reconstruction algorithm appears to only really be accurate for θ in the 0 - $\frac{\pi}{2}$ range, and to become a lot less reliable as θ approaches each of those limits.[58] Hence it will not be reliable for measurements where accuracy is of supreme importance

In summary, the strength of this class of techniques lies in the fact that we are only interested in point intensities, not images, therefore avalanche photodiodes are used to give us significantly faster results than CCDs, and this can allow for the detection of molecule orientations on extremely short time scales. On the other hand, the technique is also only capable of being focused on a single molecule at a time, and only if it remains in the area under illumination by a diffraction-limited spot, and it only allows for the measurement of a small range of orientations. In theory, this issue could be circumvented by using wide field imaging and CCDs to simultaneously image multiple molecules, but that does not appear to have been tried yet. It also provides no means of superresolution position estimation.

2.2.2. Scanning Fluorescence Imaging

Single molecule orientations have also been measured using scanning confocal microscopy. In this case the general idea is to scan a focused laser beam across the position of a single fluorescent molecule and read the produced fluorescence with a photon detector. This results in a pattern whose spatial distribution is dependent on the orientation of the emission dipole of the molecule and the polarisation of the excitation laser. As with single molecule polarisation imaging, there are several proposed experimental setups for achieving this aim.

Applications

One of the proposed systems[67] involves the use of Stimulated Emission Depletion microscopy (STED) with a linearly polarised Gaussian beam for excitation and a linearly polarised donut mode beam for depletion. The beams are used to scan across isolated molecules of terylene diimide (TDI) embedded in a PMMA layer on a glass cover slip. No indication is given about the size of the scanned images, just that each pixel requires between 5-10 milliseconds of integration time.

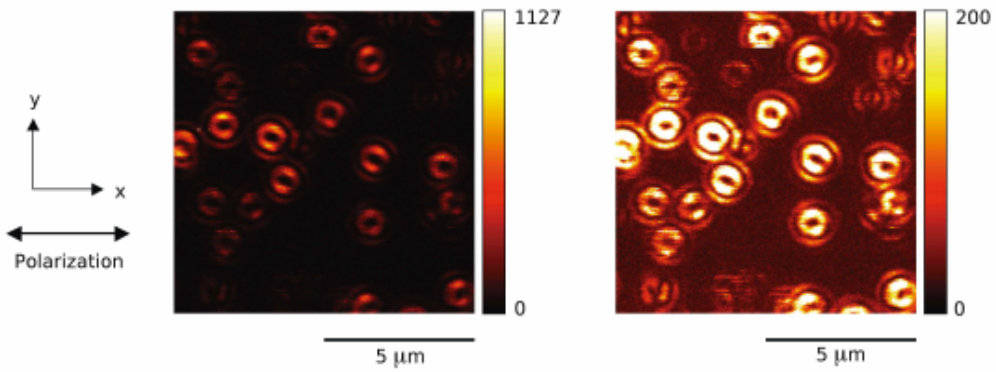

Figure 2.7.: Pattern distribution from STED imaging of single fluorescent molecules embedded in PMMA[67]

The distribution patterns produced can be seen in Figure 2.7 and are then compared to theoretically generated distribution patterns produced for molecules of differing orientations. Simulations of the system suggest that it is most sensitive to molecules close to the optical axis of the microscope and perpendicular to its input polarisation. Considering the depletion beam is linearly polarized parallel to the surface of the cover slip, vertically oriented beams would be less likely to be affected by them and thus more likely to be imaged, which is consistent with the observed result.

A similar system using annular illumination was first proposed theoretically[68] and then used experimentally a few years later.[69] The technique involves scanning single fluorescent molecules embedded in polymer thin films with a collimated laser beam with its centre blocked out and focused through a high NA objective. The fluorescence is then filtered and imaged using a Single-Photon

Avalanche Diode (SPAD). In the original publication, every pixel is about the size of a diffraction-limited spot (≈250 nm) and the collection time is on the order of 2 ms. The second publication specifies a scanning image of size 5 µm × 5 µm, a pixel size of 40 nm and a collection time of 25 ms. The predicted patterns are created by calculating the electromagnetic field distribution produced by a point dipole emitter at the interface between two materials with different dielectric properties.

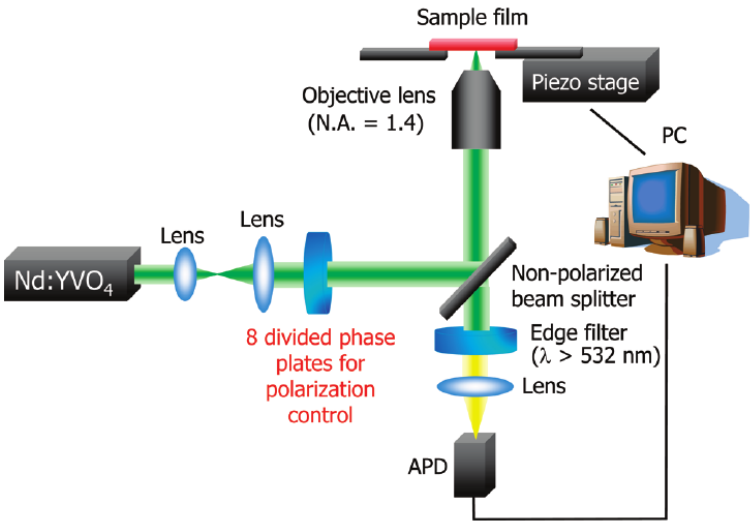

Figure 2.8.: The experimental setup for confocal orientation imaging of single fluorescent molecules[70]

Another proposed setup[70] involves the use of radially and azimuthally polarised lasers to perform the confocal scans on immobilised molecules in polymer layers (Figure 2.8). The beam is used to scan across the molecules and the fluorescence imaged by an APD. Each scanning image has a pixel size of 30 nm × 30 nm and a collection time of 10 ms per pixel. The different polarisation modes are generated by using a radial polariser created from 8 $\frac{\lambda}{2}$ plates (Figure 2.9). A vertically polarised beam sent through the polariser is converted into a radially polarised beam while a horizontally polarised beam is converted into an azimuthally polarised beam. The purpose of the differing polarisations is because they each provide angular resolution in orthogonal directions. Radial polarisation provides

good z-axis orientation resolution and azimuthal polarisation provides good x-y angular resolution.

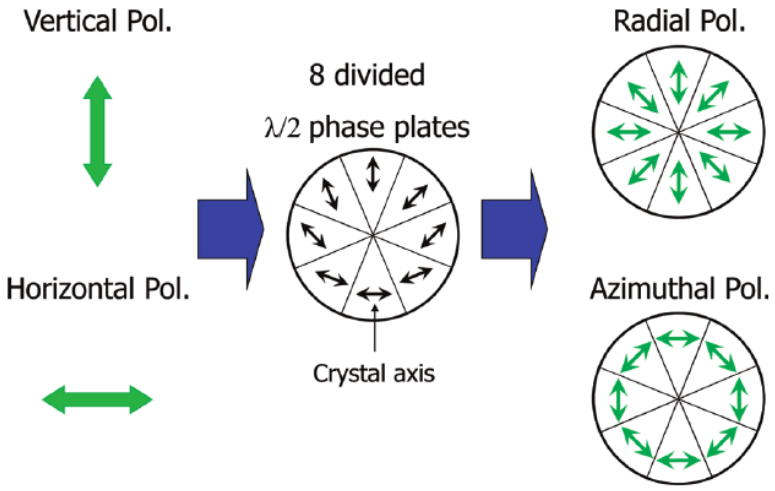

Figure 2.9.: The configuration of the radial polariser[70]

Limitations

There does not appear to have been any attempt at analysing any of this class of techniques to estimate the uncertainty in orientation measurement relative to integration time or photon count. It is therefore difficult to have a real idea how good this class of orientation measurement techniques are. The best we can assume is that since single pixel collection times of 2 ms to 25 ms, a 10×10 pixel space requires an integration time on the order of the shortest times required for defocused imaging.

Hence, there does not appear to be a speed advantage to this technique, especially when simultaneously imaging multiple molecules. There is also no talk of position measurement and we have no means of determining how accurate the orientation measurements are.

2.2.3. Intensity pattern

These methods are similar to the defocused fluorescence imaging technique discussed throughout this thesis. They all image fluorescent molecules and then compare the produced patterns to patterns predicted computationally. These techniques do not defocus the image though. Instead they all depend on different methods to create patterns large enough to make their features noticeable. It is worth discussing the strengths and drawbacks of these systems to understand why they are less preferable than defocused orientation imaging.

Applications

One approach[71–74] involves probing the sample using objective TIRF, but with the introduction of spherical aberrations by a very thin layer of water ($\approx$10 µm) on top of the immersion oil (example in Figure 2.10). The aberrated single molecule images are then compared to calculated images the intensity distribution for different dipole orientations. This technique allows for $\approx$100 ms time resolution in their experiments. The goodness of the least squares fit between the calculated images and the obtained ones is not discussed. The closest thing there is to error analysis is an assertion that the error for each measurement is significantly less than the magnitude of rotation.[72]

A similar technique[75] is used with a circularly polarised incident beam and appears able to obtain real time (40ms) data on the conformation changes of the molecules under investigation. In this case, the experimental setup appears exactly the same, modelled images are created for every 2° difference in θ and ϕ and the obtained images are compared to those. Again, there is no discussion of the goodness of the fit between the calculated and obtained images or whether the technique is more accurate over a certain range of dipole orientations. Without them it is difficult to tell what the potential weaknesses of the technique are.

Another technique is proposed by Lieb[76] and then a variation of it is actually experimentally applied,[61] as can be seen in Figure 2.11. It involves the confocal

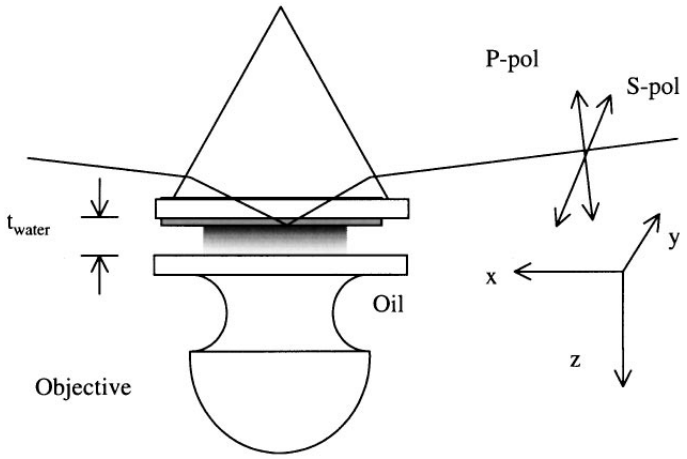

Figure 2.10.: Example of molecular orientation setup using TIRF with optical aberrations introduced by a thin layer of water[72]

imaging of stimulated molecular fluorescence. The fluorescence images are defocused using a Bertrand lens before they reach the CCD. The resulting intensity patterns are then compared to simulated versions of those same patterns. The molecules are excited with light polarised along the horizontal and vertical axes as well as radially polarised light.

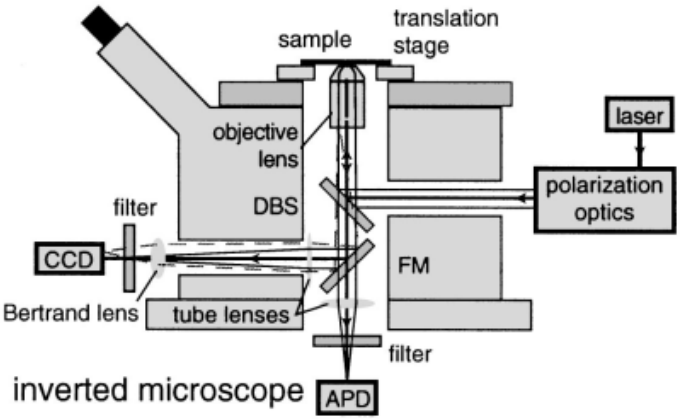

Figure 2.11.: Experimental setup consisting of an inverted microscope, a green excitation laser (532 nm), a polarisation optics box containing a half-wave plate, a quarter-wave plate, and a mode converter, DBS, dichroic mirror; FM, flip mirror; APD, avalanche photodiode; CCD, a cooled CCD camera.[76]

Limitations

Lieb's technique does have some error analysis associated with it. It requires roughly one second to obtain images, although it is suggested that reducing accuracy could reduce capture times to ≈20 ms. The included error analysis shows an error range of ≈1.7° in θ and ≈1.1° in ϕ. but the levels of error for θ also grow as ϕ approaches 2π, making the technique less effective for specific dipole orientations. There does not appear to have been any more error analysis done relative to orientation determination.

With respect to acquisition time, the fastest technique claims 40ms full frame acquisition time. This class of techniques are all interesting, but appear to have been even less well researched than defocused orientation, making it the most popular and well travelled method.

2.3. Summary

In this section, I have introduced and explained the technique of defocused fluorescence orientation imaging and the ways it has been used to investigate the ordering of static thin films, the inhomogeneity of melting films and the movement of molecular motors. In examining the limitations of the technique, I show that there has been very little investigation of the accuracy of the orientation measurements beyond an assertion that there is an uncertainty of 10°-15° for an exposure time of 0.6 s. The range of observed acquisition times varied between 50 s and 200 ms.

In order to explain my choice in techniques, I also summarise the other classes of single molecule orientation techniques (polarisation, scanning laser microscopy and other pattern matching techniques), discussed their uses in similar systems and why they appeared less promising choices. Single molecule polarisation appears to be at least an order of magnitude faster than defocused orientation measurements, but can only track one molecule at a time, has a very limited range of orientations over which it works and does not appear to have superresolution

position estimation. Scanning laser microscopy techniques also do not appear to have any error analysis and tend to require similar levels of acquisition time to defocused fluorescence imaging, again with no added superresolution benefits. Some of the other pattern matching techniques have faster acquisition times than defocused orientation imaging, but again there is no real error analysis and they have all been investigated to a much lower degree. Defocused fluorescence imaging appears to be the best technique to investigate, as it has fairly low acquisition times, does not require an overly complicated instrument setup.

Chapter 3.

Theory

3.1. Defocused Fluorescence Patterns

The central assumption of this technique is the idea that it is possible to model the emission dipole of a single fluorescent molecule as a classical oscillating electric dipole. The implication of this model is that the spatial distribution of photons produced by the fluorescing molecule will be equivalent to the angular distribution of the electromagnetic field produced by an oscillating dipole. Thus, the spatial distribution of photons produced by a molecule positioned close to the interface between two materials with differing dielectric properties will be the same as the angular distribution of the field produced by a dipole at the same interface.

By calculating the distribution of this pattern after being imaged through a high numerical aperture (NA) objective, it is therefore possible to predict the fluorescence pattern that would be imaged by a highly sensitive camera positioned at the image plane of the objective, which has been displaced by a small distance ($\approx$300 nm to 1000 nm) towards the dipole.

The first step in describing the field intensity imaged by the CCD involves describing the intensity distribution of the (P_∞) of the spatial pattern produced by the dipole when embedded in a homogeneous dielectric medium is described by Lukosz and Kunz[77–79] as

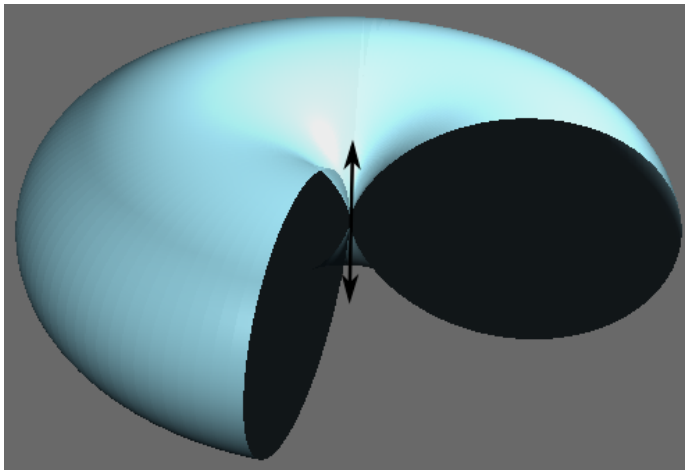

Figure 3.1.: An illustration of the field distribution produced by a dipole. It shows that the strength of the field produced by a dipole displays a $\sin^2\theta$ distribution, where θ is along the axis of the dipole

$$P_\infty^{(p)}(\alpha,\phi) = \frac{3}{8\pi}[\cos\theta\sin\alpha + \sin\theta\cos\phi\cos\alpha]^2 \tag{3.1}$$

$$P_\infty^{(s)}(\alpha,\phi) = \frac{3}{8\pi}\sin^2\theta\sin^2\phi \tag{3.2}$$

$$P_\infty = P_\infty^{(p)}(\alpha,\phi) + P_\infty^{(s)}(\alpha,\phi) \tag{3.3}$$

Where $P_\infty^{(p)}(\alpha,\phi)$ and $P_\infty^{(s)}(\alpha,\phi)$ are the p- and s- polarized components of the field and ϕ is the angle between the dipole axis and the z axis. For the case where $\phi = 90°$, the field distribution is shown in Figure 3.1. The $\sin^2\theta$ dependence of the field distribution can be easily seen. While light is actually emitted by a fluorophore in photons rather than as a continuous wave, the spatial distribution described this way still represents the spatial distribution produced after a large enough number of photons have been emitted.

In order to most easily model the field distribution, we represent the spherically symmetric field distribution in terms of plane waves using the Weyl representation. This is because the field produced by the dipole interacts with an interface that is a flat plane, making plane waves an easier way to calculate the field's interaction

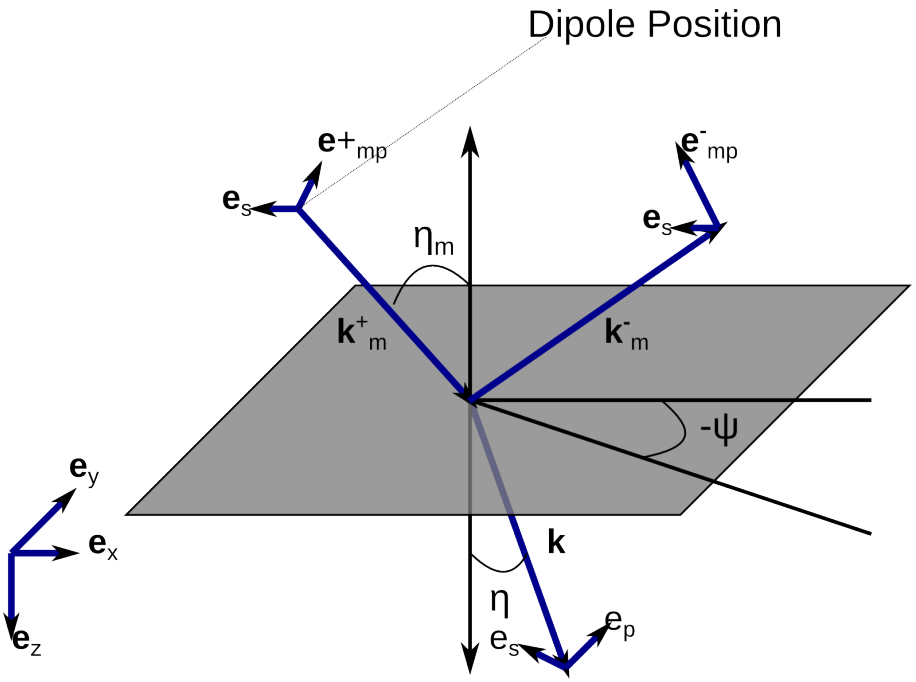

Figure 3.2.: Geometry of the plane waves ($e_p and e_s$) emitted by the dipole to reflect off and transmit through the interface between two different dielectrics with refractive indices $n_m$for the top layer and n for the bottom layer. $\mathbf{k}$ is the wave vector and η_m, η are the angles of incidence and refraction respectively

with the interface. The field produced by an oscillating dipole at a position $\mathbf{r}_0$ in a homogeneous medium m can be represented at the position $\mathbf{r}$ as a superposition of plane waves represented by:

$$E(r) = \frac{4\pi}{\epsilon_m} \int \frac{d^3\mathbf{k}}{(2\pi)^3} \frac{e^{i\mathbf{k}.\mathbf{R}}}{k^2 - \epsilon_m k_0^2} [\epsilon_m k_0^2 \mathbf{p} - \mathbf{k}(\mathbf{k} \cdot \mathbf{p})] \tag{3.4}$$

Where $\mathbf{R} = \mathbf{r} - \mathbf{r}_0$, ϵ is the dielectric susceptibility and $\mathbf{k}$ is the wave vector.

Next, the dipole is placed at the interface between two dielectrics with respective refractive indices n_m and n This has been done by Enderlein,[25,80–82] Lukosz and Kunz,[79] Hellen and Axelrod[83] and other sources.

The system is defined in cylindrical coordinates with the position of the dipole as the origin and the polar axis parallel to the interface. A visual representation of the system can be seen in Figure 3.2 and the field can be expressed as:

$$E = \frac{i}{2\pi\epsilon_m} \int \frac{d^2\mathbf{q}}{w_m} [k_m^2 \mathbf{p} - \mathbf{k}_m^{\pm}(\mathbf{k}^{\pm} \cdot \mathbf{p})] \exp(i\mathbf{q} \cdot (\tilde{\mathbf{n}} - \tilde{\mathbf{n}}_0) + i\mathbf{w}_m |z - z_0|) \tag{3.5}$$

Where $(\tilde{\mathbf{n}}_0, z_0)$ represents the position of the dipole and $(\tilde{\mathbf{n}}, z)$ represents the position at which the field is being observed. Also, $\mathbf{R} = (\tilde{\mathbf{n}} - \tilde{\mathbf{n}}_0, z - z_0)$, $\mathbf{k}_m^{\pm} = (\mathbf{q}, \pm w_m)$, $w_m = \sqrt{k_m^2 - q^2}$ and $k_m = \sqrt{\epsilon_m k_0}$. The + and - superscripts represents the direction of the plane wave either towards or away from the interface. The 2D vector q is the variable over which the integration is performed.

Equation 3.5 is now recast after splitting up the plane waves into their p- and s-components, giving:

$$E = \frac{ik_0^2}{2\pi} \iint \frac{d\mathbf{q}}{w_m} [e_{mp}^{\pm}(e_{mp}^{\pm} \cdot \mathbf{p}) + e_s(e_s \cdot \mathbf{p})] \exp[i\mathbf{q} \cdot (\tilde{\mathbf{n}} - \tilde{\mathbf{n}}_0) + iw_m |z - z_0|] \tag{3.6}$$

Where $\mathbf{e}_{mp}^{+}$, $\mathbf{e}_{mp}^{-}$ and $\mathbf{e}_s$ are the unit vectors of the p- and s- polarization orthogonal to the direction the plane wave propagates.

$$\begin{aligned}
\mathbf{e}_{mp}^{+} &= (\cos(\psi)\cos(\eta_m), \sin(\psi)\sin(\eta_m), -\sin(\eta_m)) \\
\mathbf{e}_{mp}^{-} &= (-\cos(\psi)\cos(\eta_m), -\sin(\psi)\sin(\eta_m), -\sin(\eta_m)) \\
\mathbf{e}_p &= (\cos(\psi)\cos(\eta), \sin(\phi)\sin(\eta), -\sin(eta)) \\
\mathbf{e}_s &= (-\sin(\psi), \cos(\eta), 0)
\end{aligned} \tag{3.7}$$

As can be seen in Figure 3.2, the η_m is the angle at which the incident waves arrive at the interface and η is the angle at which those waves are diffracted

according to Snell's law ($n_m \sin\eta_m = n \sin\eta$). Since the reflection and transmission of plane waves across an interface between materials with different dielectric properties are governed by Fresnel's formulas, it is also necessary to define the Fresnel transmission and reflection coefficients for p- and s- polarized waves $T_{p,s}$, $R_{p,s}$.

$$\begin{aligned} R_p &= \frac{w_m\epsilon - w\epsilon_m}{w_m\epsilon - w\epsilon_m}, & R_s &= \frac{w_m - w}{w_m + w} \\ T_p &= \frac{2n_m n w_m}{w_m\epsilon + w\epsilon_m}, & T_s &= \frac{2w_m}{w_m + w} \end{aligned} \tag{3.8}$$

Once we have these, we can use them and Equation 3.6 to represent fields reflected at (E_R) and transmitted through (E_T) the interface.

$$\begin{aligned} E_T = \frac{ik_0^2}{2\pi} \iint \frac{d\mathbf{q}}{w_m} &[\mathbf{e}_p T_p(\mathbf{e}_{mp}^+ \cdot \mathbf{p}) + \mathbf{e}_s T_s(\mathbf{e}_s \cdot \mathbf{p})] \exp[i\mathbf{q} \cdot (\tilde{\mathbf{n}} - \tilde{\mathbf{n}}_0) \\ &+ iw_m|z_0| + iwz] \end{aligned} \tag{3.9}$$

$$\begin{aligned} E_R = \frac{ik_0^2}{2\pi} \iint \frac{d\mathbf{q}}{w_m} &[\mathbf{e}_{mp}^- R_p(\mathbf{e}_{mp}^+ \cdot \mathbf{p}) + \mathbf{e}_s R_s(\mathbf{e}_s \cdot \mathbf{p})] \exp[i\mathbf{q} \cdot (\tilde{\mathbf{n}} - \tilde{\mathbf{n}}_0) \\ &+ iw_m|z_0| - iwz] \end{aligned} \tag{3.10}$$

In considering the orientation of the dipoles, the simplest way to represent the field produced by arbitrarily oriented dipoles (geometry shown in Figure 3.3) is in terms of combinations of fields produced by three orthogonal dipoles. A dipole oriented perpendicular to the interface and two perpendicular dipoles oriented parallel to the interface.

$$E(\eta, \psi) = \mathbf{e}_p[\cos\theta E_p^{\perp}(\eta) + \sin\theta E_p^{\parallel}(\eta)\cos\psi] + \mathbf{e}_s \sin\beta E_s^{\parallel}(\eta)\sin\psi \tag{3.11}$$

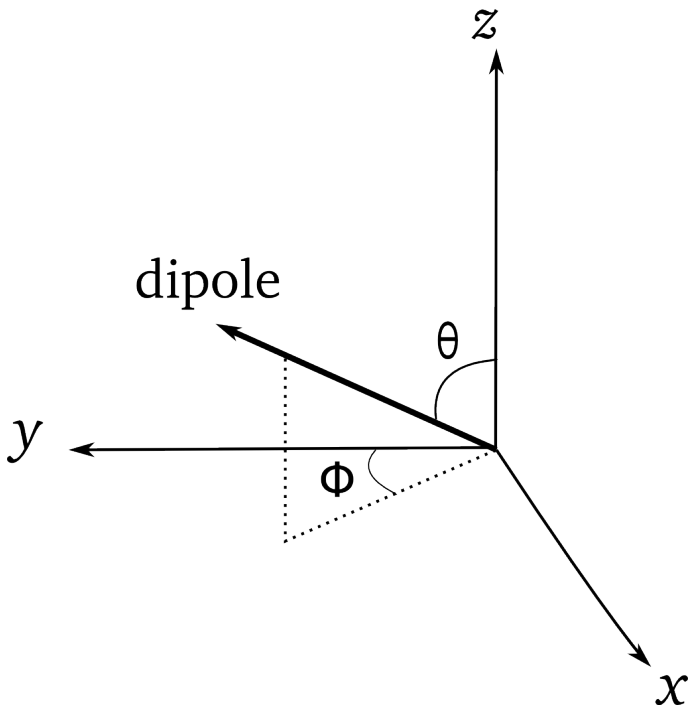

Figure 3.3.: Dipole orientation in terms of θ and ϕ

The expressions for these dipoles are produced by integrating Equation3.6 for the field transmitted below the interface along the **k** direction in a solid cone $\sin\eta, d\eta d\psi$

$$\begin{aligned} E_p^{\perp}(\eta) &= \frac{nw}{w_m}\frac{q}{n_m}T_p \exp(iw_m|z_m|) \\ E_p^{\parallel}(\eta) &= \frac{nw}{n_m}T_p \exp(iw_m|z_m|)\cos\psi \\ E_s^{\parallel}(\eta) &= -\frac{nw}{w_m}T_s \exp(iw_m|z_m|)\sin\psi \end{aligned} \tag{3.12}$$

Once the field distribution of an arbitrarily oriented dipole radiating through an interface has been established, its spatial distribution on a CCD chip after imaging through a high NA objective must then be calculated. The intensity distribution of light on the camera pixels will be the z-component of the Poynting vector of the field imaged through the objective.

$S = (c/8\pi)e_z \cdot (\mathbf{E} \times \mathbf{B}^*)$

The electric and magnetic field amplitudes as imaged through a perfect objective will take the form:[81,84]

$$\left\{ \begin{array}{c} E_j \\ B_j \end{array} \right\} = \int_0^{\acute{\eta}_{max}} d\acute{\eta} \sin\acute{\eta} \sqrt{\frac{\acute{\eta}\cos\acute{\eta}}{\eta\cos\eta}} \left\{ \begin{array}{c} e_j \\ b_j \end{array} \right\} \times \exp(ik\delta z \cos\eta) \tag{3.13}$$

Where:

$$\begin{aligned} \left\{ \begin{array}{c} e_x \\ e_y \end{array} \right\} =& \frac{i\sin\theta}{2} \left\{ \begin{array}{c} \cos\acute{\eta}(J_0 - J_2\cos 2\psi)E_p^{\parallel} + (J_0 - J_2\cos 2\psi)E_s^{\parallel} \\ -\cos\acute{\eta}J_2\sin 2\psi E_p^{\parallel} + J_2\sin 2\psi E_s^{\parallel} \end{array} \right\} \\ &+ i\cos\theta\cos\acute{\eta}J_1 E_p^{\perp} \left\{ \begin{array}{c} \cos\psi \\ \sin\psi \end{array} \right\} \end{aligned} \tag{3.14}$$

$$\begin{aligned} \left\{ \begin{array}{c} b_x \\ b_y \end{array} \right\} =& \frac{i\acute{n}\sin\theta}{2} \left\{ \begin{array}{c} J_2\sin 2\psi E_p^{\parallel} - \cos\acute{\eta}J_2\sin 2\psi E_s^{\parallel} \\ (J_0 - J_2\cos 2\psi)E_p^{\parallel} + \cos\acute{\eta}(J_0 - J_2\cos 2\psi)E_s^{\parallel} \end{array} \right\} \\ &+ i\cos\theta\acute{n}J_1 E_p^{\perp} \left\{ \begin{array}{c} -\sin\psi \\ \cos\psi \end{array} \right\} \end{aligned} \tag{3.15}$$

Where $J_{0,1,2}$ are Bessel functions of the first kind with argument $\acute{k}, \acute{\rho}\sin d\acute{\eta}$. The angles η and $\acute{\eta}$ are connected by the magnification of the objective M as shown by Abbe's law $n\sin\eta = M\acute{n}\sin\acute{\eta}$, where n is the refractive index of the glass and $\acute{n}$ is the refractive index of the medium between the objective and the CCD (assumed to be 1). The maximum value of $\acute{\eta}$ is thus a function of the NA of the

objective (arcsin$(NA/M\acute{n})$). The distance by which the objective is defocused is represented by δz

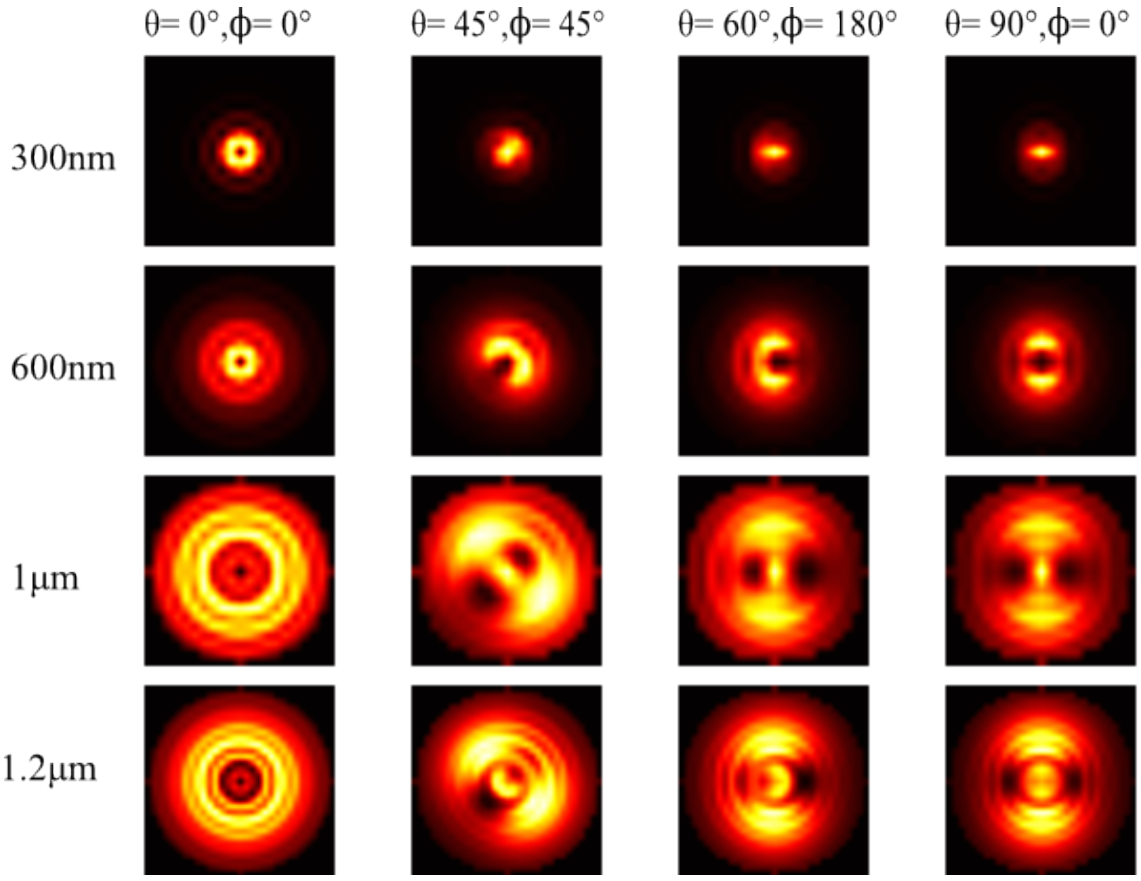

Figure 3.4.: Predicted intensity distribution patterns for different defocus distances and dipole orientations

Figure 3.4 is a clear example of the defocused patterns generated by a Python implementation of the algorithm created in the process of understanding it. The patterns are the modulus of the Poynting vector at the focusplane produced by a dipole at a polymer-glass interface imaged through a 100x, NA=1.4 oil objective for varying values of θ, ϕ and δz.

3.2. Comparing Predicted Images to Calculated Images

Once the defocused patterns have been calculated for different orientations, it then becomes necessary to compare them to experimentally obtained images from systems with a similar geometry to the simulation. Patra, Gregor and Enderlein[27] propose and describe in great detail a least-squares fitting technique for comparing theoretical images to all possible parts of the experimentally derived image.

The purpose of the algorithm is to locate all the patterns in an image and compare them to a set of R previously generated patterns. To begin with, we define x_{jk} as the intensity value of a pixel from the original image with coordinates j, k. Each pattern of the predefined patterns $p_{jk}^{(r)}$ is of the size$(2L+1) \times (2L+1)$ where $-L \leq j \leq l$, $-L \leq k \leq L$. The variable r represents one of the generated images($1 \leq r \leq R$).

Since the patterns under investigation are circular, but the defined areas are square, support matrices s_{jk}^{r} can be defined of the same size as the defined areas but using values of 1 and 0 to mask the defined areas. A uniform background b may also be superimposed on the patterns.

The algorithm works by choosing the pattern that yields the smallest least-squares fit for a given sub-area of the larger image x. This means for any given sub-area of the image with pixels $m - L \leq j \leq m + L$ and $n - L \leq k \leq n + L$, the algorithm finds two parameters $c_{mn}^{(r)}$ and $d_{mn}^{(r)}$ so that the least-squares error $e_{mn}^{(r)}$ is minimised.

$$e_{mn}^{r} = \sum_{j=-L}^{L} \sum_{k=-L}^{L} s_{jk}(s_{m+j,n+k} - c_{mn}^{(r)} p_{jk}^{(r)} - d_{mn}^{(r)} b_{jk})^2 \tag{3.16}$$

It is assumed that the patterns $p_{jk}^{(r)}$ and the background pattern b_{jk} are all square-normalised such that

$$\sum_{j=-L}^{L}\sum_{k=-L}^{L} s_{jk}(p_{jk}^{(r)})^2 = 1 \text{ and } \sum_{j=-L}^{L}\sum_{k=-L}^{L} s_{jk}(b_{jk}^{(r)})^2 = 1 \tag{3.17}$$

Differentiation with respect to $c_{mn}^{(r)}$ and $d_{mn}^{(r)}$, the results are the equations

$$\begin{aligned}\frac{\partial e_{mn}^{(r)}}{\partial c_{mn}^{(r)}} &= \sum_{j=-L}^{L}\sum_{k=-L}^{L} s_{jk}(x_{m+j,n+k} - c_{mn}^{(r)}p_{jk}^{(r)} - d_{mn}^{(r)}b_{jk})p_{jk}^{(r)} = 0 \\ \frac{\partial e_{mn}^{(r)}}{\partial b_{mn}^{(r)}} &= \sum_{j=-L}^{L}\sum_{k=-L}^{L} s_{jk}(x_{m+j,n+k} - c_{mn}^{(r)}p_{jk}^{(r)} - d_{mn}^{(r)}b_{jk})b_{jk} = 0\end{aligned} \tag{3.18}$$

With $1 \leq r \leq R$. By introducing the abbreviations

$$\begin{aligned}X_{mn} &\equiv \sum_{j=-L}^{L}\sum_{k=-L}^{L} s_{jk}x_{m+j,n+k}b_{jk} \\ Q_{mn}^{(r)} &\equiv \sum_{j=-L}^{L}\sum_{k=-L}^{L} s_{jk}x_{m+j,n+k}p_{jk}^{(r)} \\ P^{(r)} &\equiv \sum_{j=-L}^{L}\sum_{k=-L}^{L} s_{jk}p_{jk}^{(r)}b_{jk}\end{aligned} \tag{3.19}$$

those two equations can be rewritten in matrix form as

$$\begin{pmatrix} 1 & p^{(r)} \\ p^{(r)} & 1 \end{pmatrix} \begin{pmatrix} c_{mn}^{(r)} \\ b_{mn}^{(r)} \end{pmatrix} = \begin{pmatrix} Q^{(r)} \\ X_{mn} \end{pmatrix} \tag{3.20}$$

Leading to the solution

$$\begin{pmatrix} c_{mn}^{(r)} \\ b_{mn}^{(r)} \end{pmatrix} = \begin{pmatrix} 1 & P^{(r)} \\ P^{(r)} & 1 \end{pmatrix}^{-1} \begin{pmatrix} Q_{mn}^{(r)} \\ X_{mn} \end{pmatrix} = \frac{1}{\sqrt{1-(P^{(r)})^2}} \begin{pmatrix} 1 & -P^{(r)} \\ -P^{(r)} & 1 \end{pmatrix}^{-1} \begin{pmatrix} Q_{mn}^{(r)} \\ X_{mn} \end{pmatrix} \tag{3.21}$$

Assuming that there are no negative pixel values and at least one of them has a positive value results in $0 < P^{(r)} < 1$ where the solution is real and well-defined.

The least-square error is calculated as

$$e_{mn}^{(r)} = (X_{mn})^2 - \frac{(Q_{mn}^{(r)})^2 + (X_{mn})^2 - 2P^{(r)}Q_{mn}^{(r)}X_{mn}}{\sqrt{1-(P^{(r)})^2}} \tag{3.22}$$

with $(X^2)_{mn}$ as

$$(X^2)_{mn} \equiv \sum_{j=-L}^{L} \sum_{k=-L}^{L} s_{jk} x_{m+j,n+k}^2 \tag{3.23}$$

The minimum error $e_{mn}^{(r)}$ at each position (m, n) is chosen as the most likely pattern for that position. This leads to the generation of two images $\tilde{c}_{mn}$, $\tilde{e}_{mn}$ with the values of $c_{mn}^{(r)}$ and $e_{mn}^{(r)}$ for the minimum error value. Pattern positions are then localized by looking for positions where the ratio $\tilde{c}_{mn}/\sqrt{\tilde{e}_{mn}}$ exceeds an arbitrary threshold value k. A value ≈ 1 has been shown to provide good results.

Figure 3.5 is an example of the pattern recognition algorithm being applied to an experimentally obtained pattern. Its closest matching pattern is also shown.

Even though a Python script was used to generate the images in Figure 3.4, Georg Enderlein's MATLAB program was used to generate them for the purposes of experiment and also provided an implementation of the pattern matching

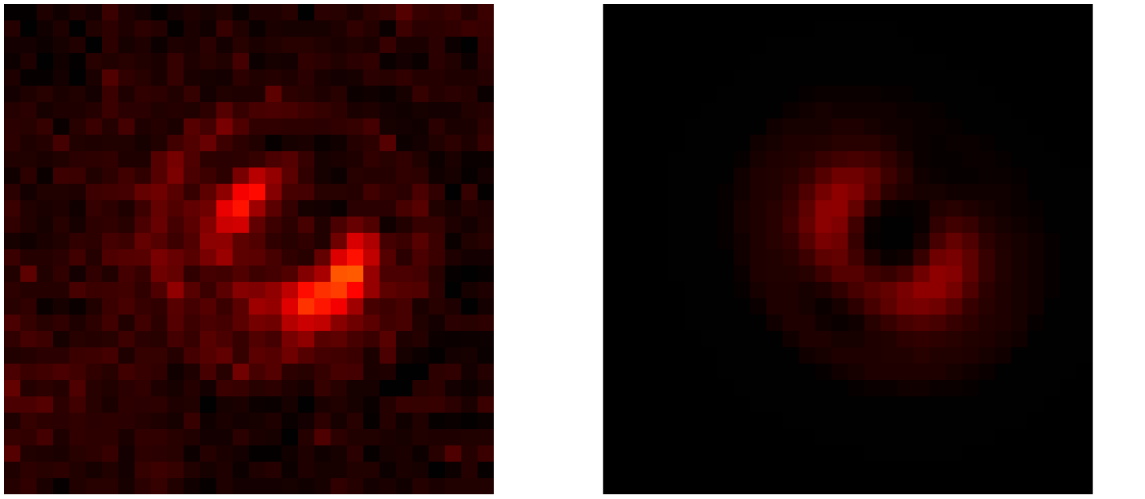

(a) Defocused Image (b) Corresponding Pattern

Figure 3.5.: Defocused image of a fluorescent molecule compared to the identified pattern

algorithm used in all of the experiments. More details about the exact nature of the MATLAB program can be seen in Appendix A. In order to save the data and perform analysis on the results, I was required to modify the original program and add more MATLAB and Python code.

3.3. Physical Limits Of Orientation Measurements

Each defocused pattern is produced by photons emitted stochastically from a single molecule and absorbed by an array of pixels on a CCD camera. The final image is therefore made up of the photons absorbed from the molecule as well as noise both from the camera and the microscope.The pattern recognition algorithm is being employed to resolve a statistically generated pattern against a noisy background and fit it to perfect theoretically generated patterns in order to provide an estimate on its position and orientation.

It is therefore important to try to quantify the physical limitations of the experimental system used to observe these patterns as well as the limitations of the pattern recognition algorithm to determine the minimum number of photons

required to create a pattern whose position and orientation can be accurately predicted. In order to achieve this aim, a computational model will be used to investigate the limits of the system and the algorithm.

This approach to determining the physical limitations of the system has been employed in the examination of various single molecule superresolution location techniques.[58,62,85–89] It involves creating a virtual camera, sample and imaging system then simulating the process of obtaining and fitting a defocused pattern. The entire system was simulated in MATLAB making use of Georg Enderlein's pattern generation and matching algorithm. The random emission from single molecules was modelled arriving at the pixels of the CCD camera both with and without noise sources to provide an estimate of how many photons are required to provide a clear enough intensity pattern for an accurate fit to be performed against the generated library.

This approach is fairly complicated because of the number of free parameters that can be varied. The exact nature of a defocused orientation measurement will depend on the sample under investigation (number, thickness and refractive indices of the layers of the sample), the imaging system (magnification and NA of the objective, pixel size of the camera) and the pattern matching algorithm (accuracy desired in terms of θ and ϕ)

Since it was not possible to cover every single permutation of those parameters, a target system exactly like the one used experimentally was defined and used as the sample system. The sample was therefore represented as a single fluorescent Dil molecule (emission wavelength of 633 nm) embedded in a 10 nm thick PMMA layer on top of a 170 µm thick glass cover slip. It was then imaged via an oil immersion objective defocused towards the sample and imaged on the pixels of a CCD camera. The imaging system was defined for multiple values of Numerical Aperture (1.3, 1.4 and 1.5), defocus distance (300 nm, 600 nm and 1 µm) and effective pixel size (50 nm, 100 nm and 150 nm). Effective pixel size is, for our purposes, defined as CCD pixel size/microscope magnification. As for the pattern matching algorithm, intensity distribution images were generated at 10° intervals of both θ and ϕ.

The initial simulation was performed assuming a perfect system where neither the camera or the microscope added any noise. In order to provide a more accurate idea of the functionality of the system, the camera was also modelled as a more realistic EMCCD camera with a basic noise profile. CCD camera noise generally comes in the form of readout amplifier noise and dark current. In the case of the cooled EMCCD camera used for imaging defocused patterns, the $-90\,^{\circ}\mathrm{C}$ temperature the CCD chip is cooled to reduces the dark noise to negligible levels, However, the process of amplifying the initial CCD signal that make EMCCD cameras so sensitive is also a noise source. That noise is therefore added to the model. EMCCD readout noise is generally modelled as a 2-D Poisson distribution.[90] The Poisson distribution is a discrete probability distribution where the probability of finding any positive integer variable k in a distribution with mean λ is represented by the function

$$f(k;\lambda) = \frac{\lambda^k e^{-\lambda}}{k!}$$

I assumed a mean value of λ = 300 counts for the noise distribution. The noise simulations were therefore created by adding a background frame with randomly generated pixel values following the Poisson distribution discussed previously to the generated pattern before pattern recognition was applied. There was still an assumption of no other noise sources, so this was far from a perfect simulation, but still provided insight into the limitations of the pattern matching algorithm.

Each intensity distribution image was normalised and then used to generate a 2D probability map. Photons were randomly generated and added to the CCD in a manner determined by the probability map. A comparison of a predicted pattern against patterns produced by randomly generating photons and adding them to the probability map can be seen in Figure 3.6.

After every 1000 photons were added to the camera, the pattern matching algorithm was used to compare the randomly generated image to the pattern distribution library. Every time pattern matching was performed and a fit was found,

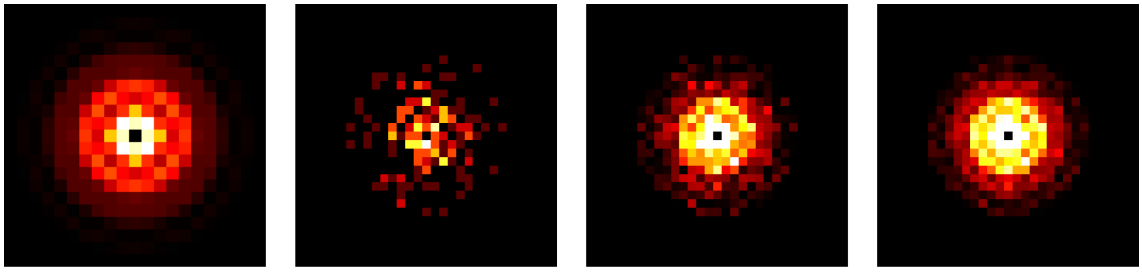

(a) Predicted Image (b) 200 Photons (c) 3200 Photons (d) 12800 Photons

Figure 3.6.: Calculated defocused pattern for a molecule with orientation $\theta = 0°$, $\phi = 0°$ on a 32x32pixel grid (a) vs patterns produced by randomly adding photons to the grid (b,c,d)

the position and orientation values of the detected pattern were recorded. The process was repeated until the randomly generated image matched the position and orientation of the library image perfectly or 100,000 photons had been added to the image. Each image was generated multiple times for every combination of θ and ϕ. All of the data was then collected and analysed. A more detailed explanation of the way the data was stored can be found in Appendix B.

Adding enough photons to the probability grid always resulted in a pattern that was matched to the closest theoretically generated pattern, which validated both the pattern matching algorithm and my process for generating 2D probability maps.

For the noiseless case, it proved impossible to obtain accurate results for the θ=0°, ϕ=0° within the photon budget. This did not prove to be an issue once noise was introduced. This resulted in the results for the noiseless cases all starting from θ=10°.

3.3.1. Investigating the azimuthal angle dependence of pattern matching

The first question I had about the simulation results was whether or not there was a significant ϕ dependency in the detection of fluorescence patterns. The orientation images in Figure 3.4 illustrate that, for a given θ, the patterns at different values

of ϕ are the same pattern, just rotated about the centre. This implies that pattern matching should be purely dependent of θ. If true, it would make data analysis easier as I would only have to analyse mean photon count data purely in terms of θ.

The parameters closest to those of the actual experimental system (NA=1.4, defocus = 600 nm, pixel size = 150 nm) were chosen and a simulation performed for both the noiseless and the noisy cases. In order to obtain enough data to make the analysis worthwhile, the simulations were performed 250 times for each permutation of θ and ϕ. Figure 3.7 shows the results of the simulations. The graphs represent the mean number of photons required to create a pattern matched accurately in terms of position (within a 150 nm pixel) and orientation ($\theta = \pm 5°, \phi = \pm 5°$,).

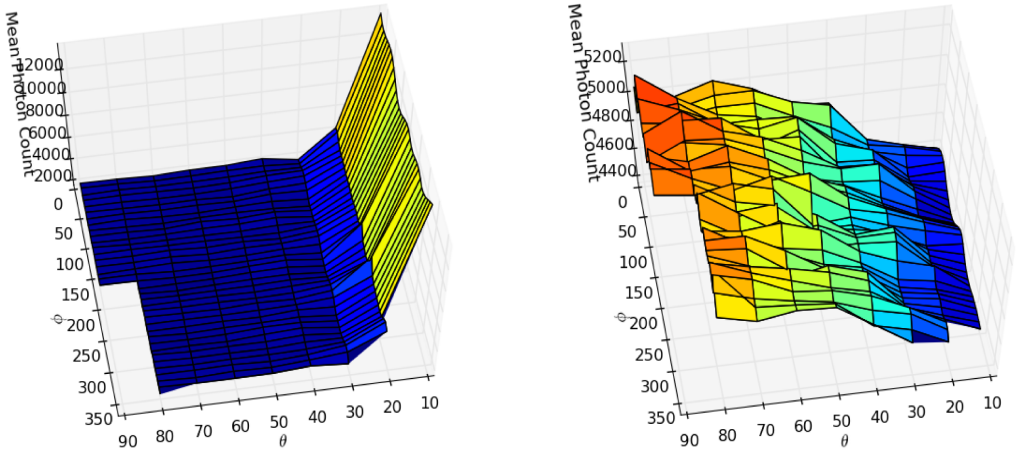

(a) No background noise (b) Background Noise

Figure 3.7.: Graphs of the mean photon number required to resolve a defocused pattern as a function of θ and ϕ for the case of zero background noise (a) and the case of Poisson readout noise with λ=300 (b)

The results showed, among other things, that the mean number of photons required to obtain a good fit are highly dependent on θ and not at all dependent on ϕ. The rest of the discussion about the relative shapes of the two graphs occurs in the next section.

3.3.2. Photon count in terms of polar angle, NA, defocus distance and pixel size

Since the mean values remain consistent across ϕ, mean photon numbers were therefore counted purely in terms of θ. Having established that, the simulations were then performed for all the other combination of NA, defocus distance and pixel size. At each set of parameters, the simulations were performed 25 times per given combination of θ and ϕ.

Figure 3.8 shows the mean number of photons required to provide a good fit relative to θ in the noiseless case for varying NA, defocus distance and effective pixel size. The first major observation that can be made from looking at the data is the difference between the mean for a defocus distance of 300 nm and a defocus distance of $\geq$ 600 nm.

For the longer defocus distances, the mean photon number distribution appears to suggest that, in the absence of any background noise, all patterns are about equally detectable when θ is between 30° and 90°. For values of θ between 10° and 30° there is a sharp rise in the mean number of photons required. There is also a sharp rise in the standard deviation as well. This sharp change in mean photon count at θ=30° is likely because the patterns at that angle are more circular and lack the more obvious asymmetries of the patterns at larger angles that make them easier to match.

For the 300 nm defocus distance though, the distribution of the mean photon count follows an entirely different trend. The counts remain very low, probably as a result of the majority of the photons being constrained within a small number of pixels, making the patterns visible sooner. Unlike for longer defocus distances though, the minimum is now for θ between 0° and 30° while the maximum occurs at 90°. As can be seen in Figure 3.4, the defocused 300 nm patterns appear substantially different from defocus patterns at longer distances, except for when θ = 0°. The difference in photon count distribution can therefore be most plausibly explained as in terms of the increased symmetry of the patterns as θ approaches

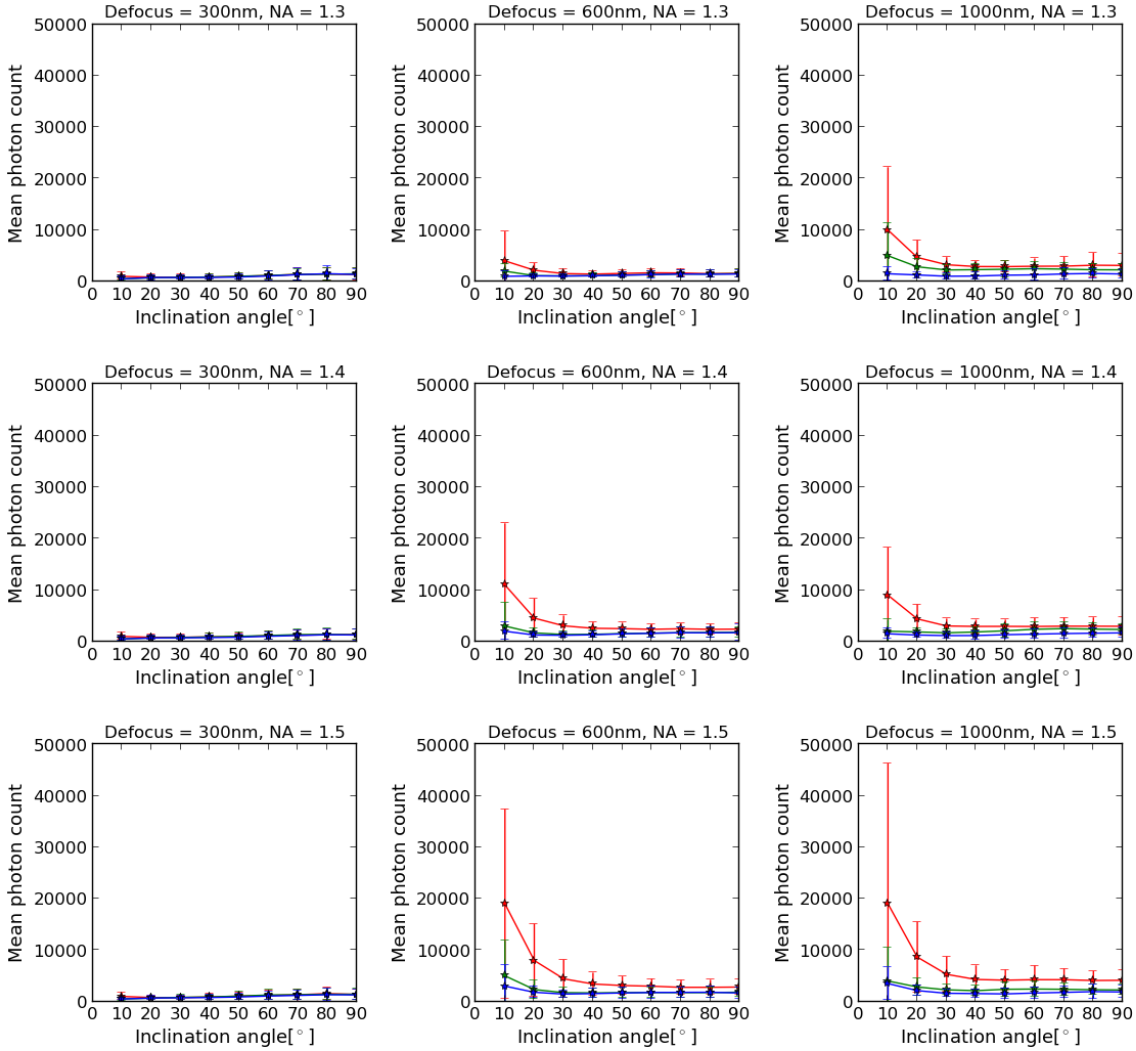

Figure 3.8.: Mean photon count relative to polar angle θ for an ideal system with no background noise. Effective pixel sizes are 50 nm (red), 100 nm (green) and 150 nm (blue)

90°. This explanation also supports the results obtained at small angles for longer defocus distances.

Reducing the effective size of each pixel means that the space occupied by the pattern spreads will cover a larger number of pixels. As a result, the number of photons hitting a single pixel will be reduced. It would therefore be reasonable to expect that more photons would be required to produce a pattern that can be

accurately matched. The gathered data seems to bear this out. Since reducing the effective pixel size also reduces the size of the area that the dipole emitter can be located in, assuming the position of the fluorophore is important, there will therefore be benefits that offset the increased photon count required.

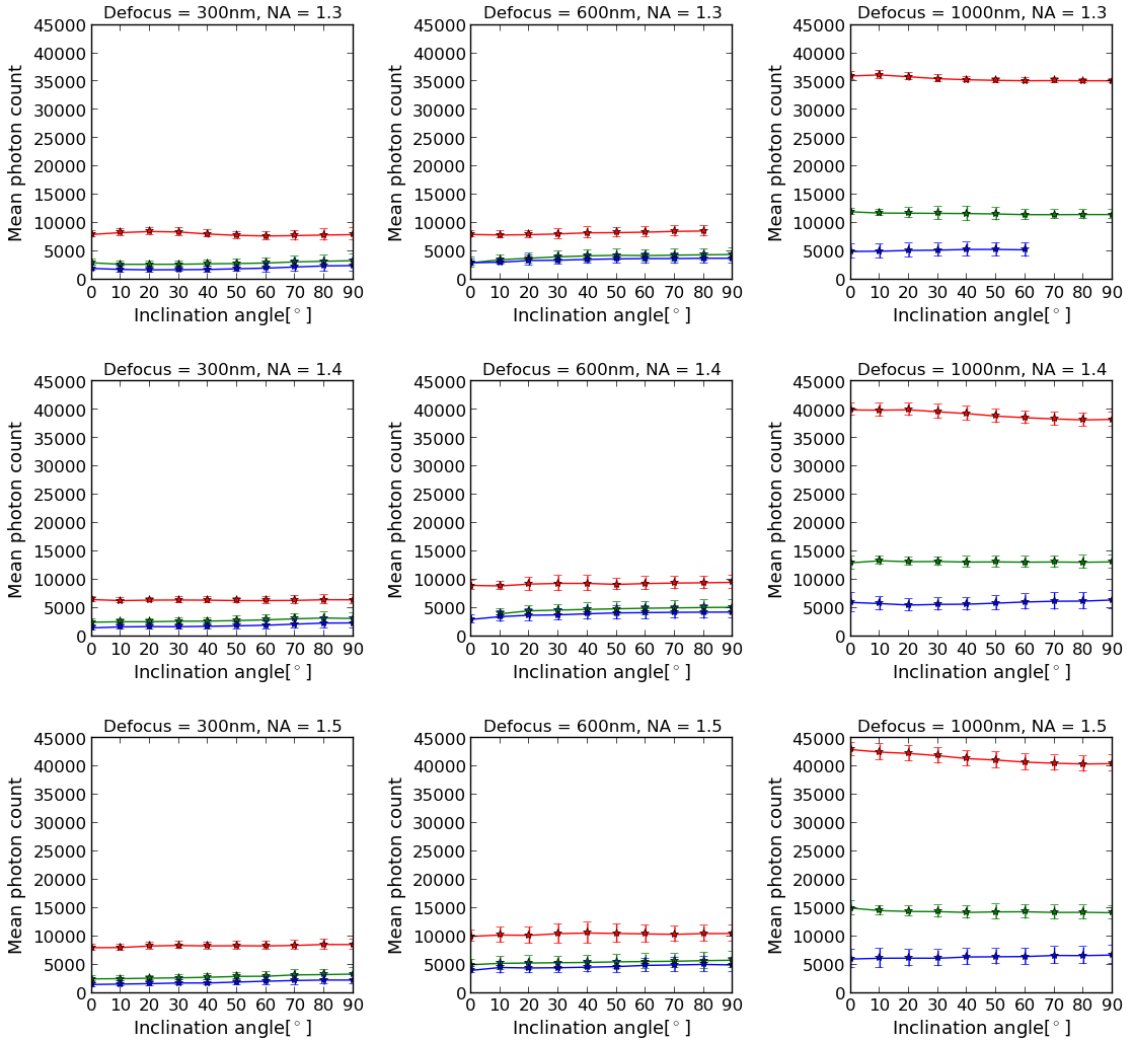

Figure 3.9.: Mean photon count relative to polar angle θ for an ideal system with Poisson distributed background noise. Pixel sizes are 50 nm (red), 100 nm (green) and 150 nm (blue)

The data also suggests a substantial difference between required photon counts for systems with a 50 nm effective pixel size and pixel sizes over 100 nm. This implies that unless accuracy in position estimation is needed to within a space smaller

than 100 nm, the photon budget for any experiment can be greatly improved by keeping the effective pixel size larger than 100 nm.

The addition of readout noise results in a differently distributed set of results that can be seen in Figure 3.9. There are two features of these results that immediately present themselves.

First, the distribution of the photon counts is substantially flatter when noise is introduced than in a noiseless system and the standard deviation remains fairly constant. The distribution reduces fairly linearly from a maximum at θ=90° to a minimum at θ=10° and the difference between the maximum value and the minimum shrinks from $\approx$ several thousands of photons to $\approx$1000 photons.

Second, the minimum number of photons required to obtain a good fit appears to become greatly dependent on the effective pixel size of the image. This is most likely a result of the need for a decent signal/noise ratio between the pattern and the readout noise. As the pixel size shrinks and the photons are therefore spread over a wider number of pixels, it takes a larger overall number of photons in order for those gathered at any one pixel to exceed the noise level by a large enough value to be detected by the pattern matching algorithm. This trend also holds true when discussing the defocus distance. Longer defocus distances tend to result in more photons being needed.

The threshold signal/noise ratio was calculated for all permutations of NA, defocus distance and pixel size as a simple ratio $\frac{n_s}{n_n}$ where n_s represents the average number of photons required to produce a recognisable pattern and n_n represents the number of noise photons in the same area, obtained by multiplying the mean of the Poisson distribution λ by the number of pixels covered by the square specified for pattern matching. For all cases the threshold ratio was between 3% and 5%. Anything above this would therefore be overkill as there would already be enough photons to fit to a pattern with positional accuracy of a single pixel and orientation accuracy $\theta, \phi = \pm 5°$.

It appears that a consequence of introducing noise into the simulation is to increase the minimum number of photons needed to create an image while sub-

stantially decreasing the difference between the number of photons required at θ=0° and 90°.

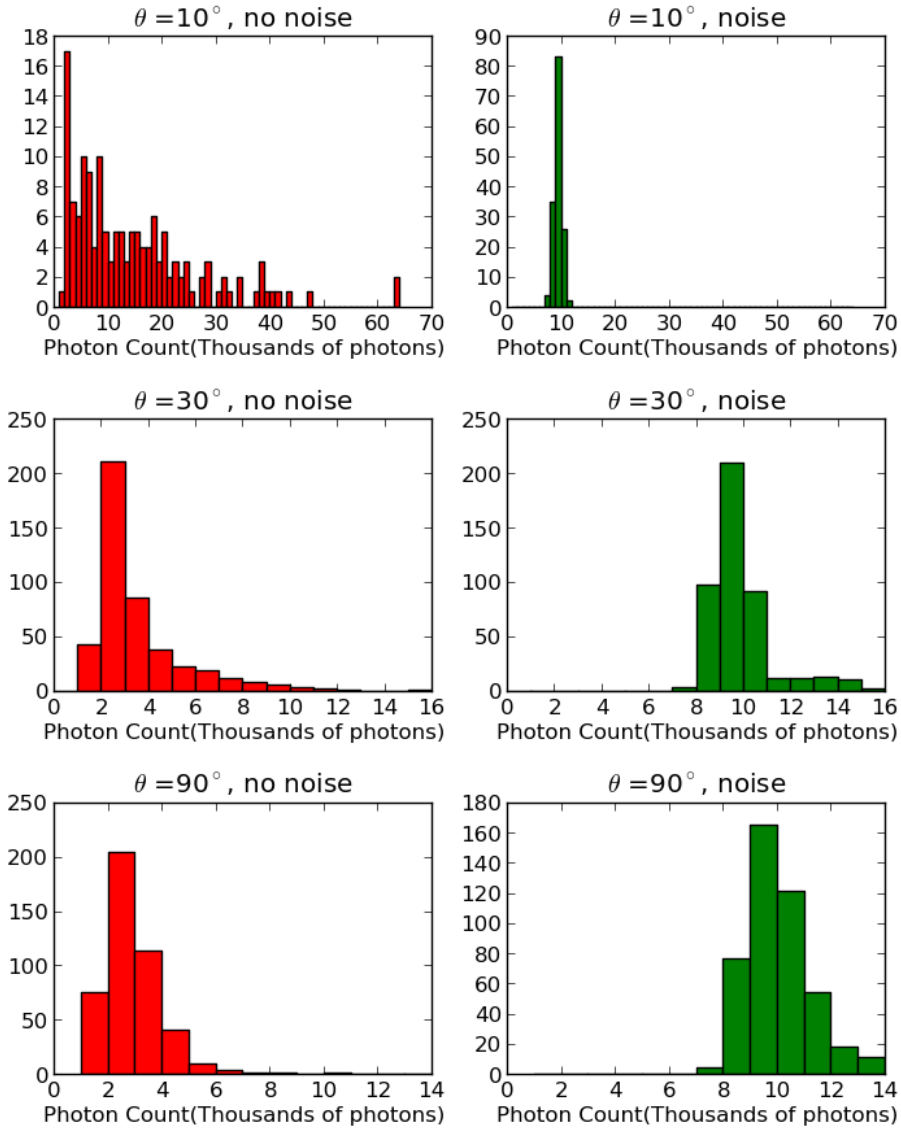

Figure 3.10.: Histogram of distribution of photon numbers required for detection of patterns representing molecules oriented at angle θ=10°, 30° and 90° when defocus = 600 nm, NA = 1.4 and effective pixel size = 50 nm

A graphical illustration of the difference between the noiseless and noisy systems can be seen in Figure 3.10, which shows histograms of the distribution of the minimum photons required for a good fit with generated patterns oriented

with θ=10°, 30° and 90° when defocus = 600 nm, NA = 1.4 and effective pixel size = 50 nm for both the noiseless and noisy cases. It can clearly be seen that there is a massive difference in photon distributions between the two cases. Adding noise clearly results in a substantial reduction in the size of the distribution of photon numbers, especially as θ approaches 0°.

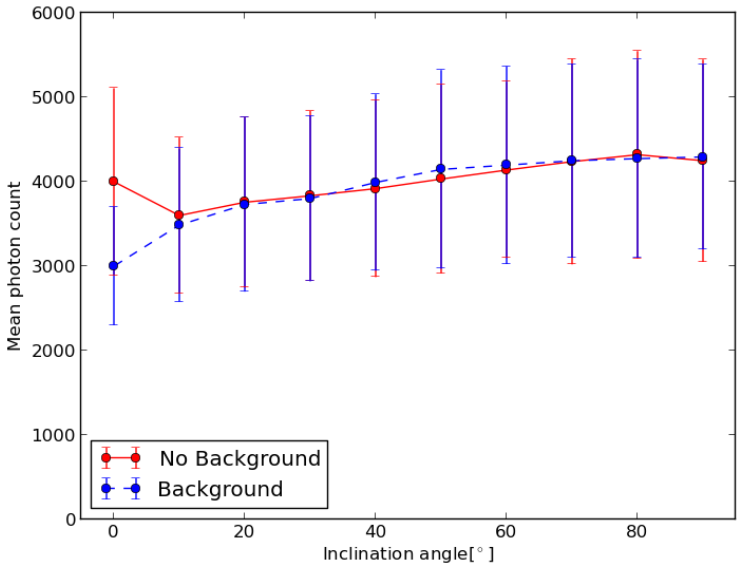

Figure 3.11.: Comparison between mean photon count relative to photon count on a noisy sample for an algorithm that explicitly corrects for background noise and another that doesn't

One possible explanation for the consistently small distributions regardless of θ value for the noisy case could be that the level of contrast required to sufficiently distinguish more circularly symmetric patterns is provided by the background noise. Another possible explanation considered was the fact that the pattern recognition algorithm used adds a flat background to every pattern when evaluating it.[27] This may make it easier to resolve patterns if they are on top of a source of noise. A comparison between data produced from simulations with and without the flat background (shown in Figure 3.11) showed that they produced almost indistinguishable results, ruling out the second explanation.

The most reasonable conclusion therefore seems to be that the background noise itself makes highly circularly symmetric patterns easier to detect with the algorithm that we are using.

3.4. Summary

First we introduced a treatment of the field produced by a vibrating dipole in a homogeneous dielectric, then showed how modelling the propagation of that field across a dielectric interface and through a high NA objective results in a pattern at the image plane that compares favourably to one produced by a single fluorescent molecule. A pattern recognition algorithm for comparing the predicted pattern to the experimentally obtained one was then introduced and explained.

The next step was to determine the effectiveness of the pattern matching algorithm by comparing randomly generated patterns to the predicted ones both in a completely noiseless case and one with readout noise from the camera included.

The implication of these simulations when it comes to photon budgets in real systems is that they shall be highly dependent on the level of noise present in the system. Provided the threshold signal/noise ratio is large enough for the pattern to be detected, the molecule's position will be within the central pixel and orientation will be within $\pm 5°$. Whether the S/N ratio and the minimum photon counts can be affected by changing the required angular accuracy or any of the other parameters held constant is a matter for further investigation.

Chapter 4.

Experimental Design

Investigating single molecule orientation required a substantial amount of experimental work. This chapter shall be devoted to describing the microscopes and attached equipment used for performing all the experiments. The software used for controlling the experimental system and analysing the data that is produced is also described in this chapter.

4.1. Microscope Design And Construction

Initially, it was proposed that the system for imaging the single molecule samples would be an Olympus Fluoview™ FV1000 confocal laser scanning system. Use of that system proved to be impractical since the project plan required the ability to change the polarisation of the incident laser beam between linear, circular and radial polarisation and there did not appear to be any convenient means of achieving that with the Olympus system, which was highly integrated and left very little room for modification.

An alternative system was therefore created by converting a Witec inverted microscope originally used as part of an objective TIRF/Tip-Enhanced Raman system. The system was equipped with both 514 nm and 633 nm lasers. The beam is deflected unto a dichroic beamsplitter that directed it through the back aperture of an Olympus 100x 1.4NA oil immersion lens unto the sample, which

was mounted on a PI movable stage. The collected light then went back though the objective and through the beamsplitter before passing through a low pass filter and being focused unto a highly sensitive cooled Andor Ixon+ EMCCD camera. The entire system was mounted on an active anti-vibration platform and enclosed in a box to keep out the light.

In the interests of creating a better, more flexible system for optical microscopy, confocal Raman and tip-enhanced Raman imaging, the Witec system was replaced by an entirely new system on which the vast majority of the single molecule orientation work was accomplished.

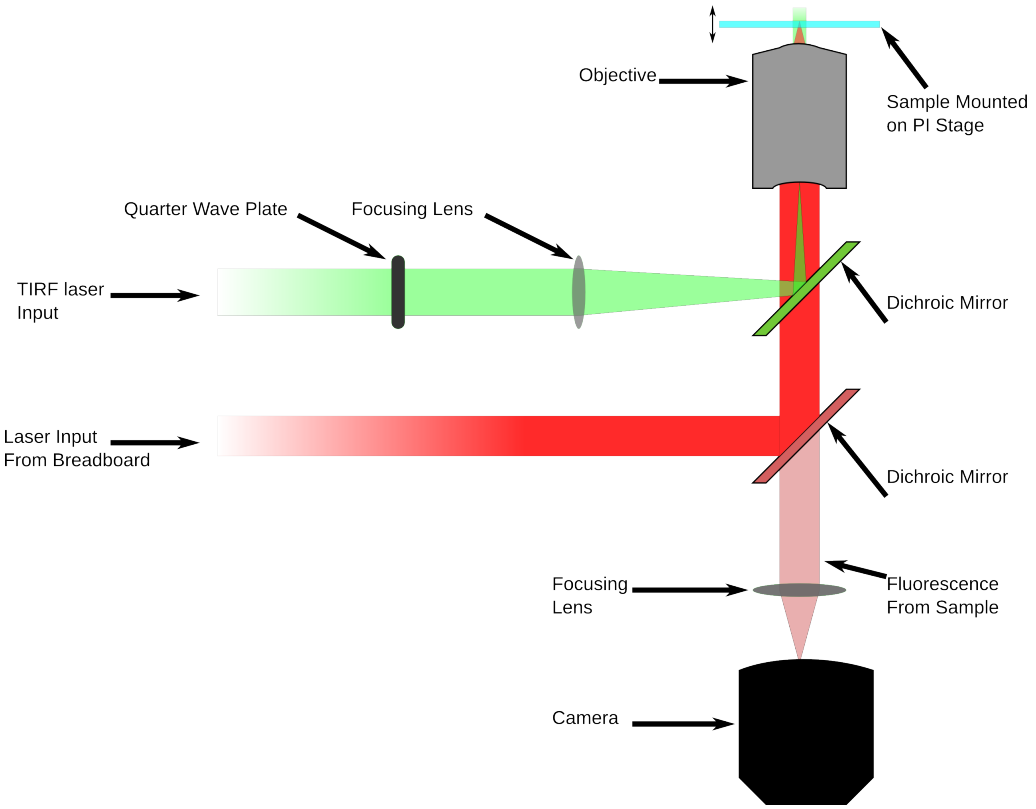

Figure 4.1.: Diagram of the most important parts of the new microscope system

The system was assembled in a new lab at NPL on a Thorlabs compressed air anti-vibration table with a custom metal shelf attached to the legs of the table to hold lasers and other pieces of equipment. The rest of the equipment is stored on a 19 inch rack positioned next to the table. A diagram of the most relevant parts of

the system can be seen in Figure 4.1 and an image of the setup on the table can be seen in Figure 4.2.

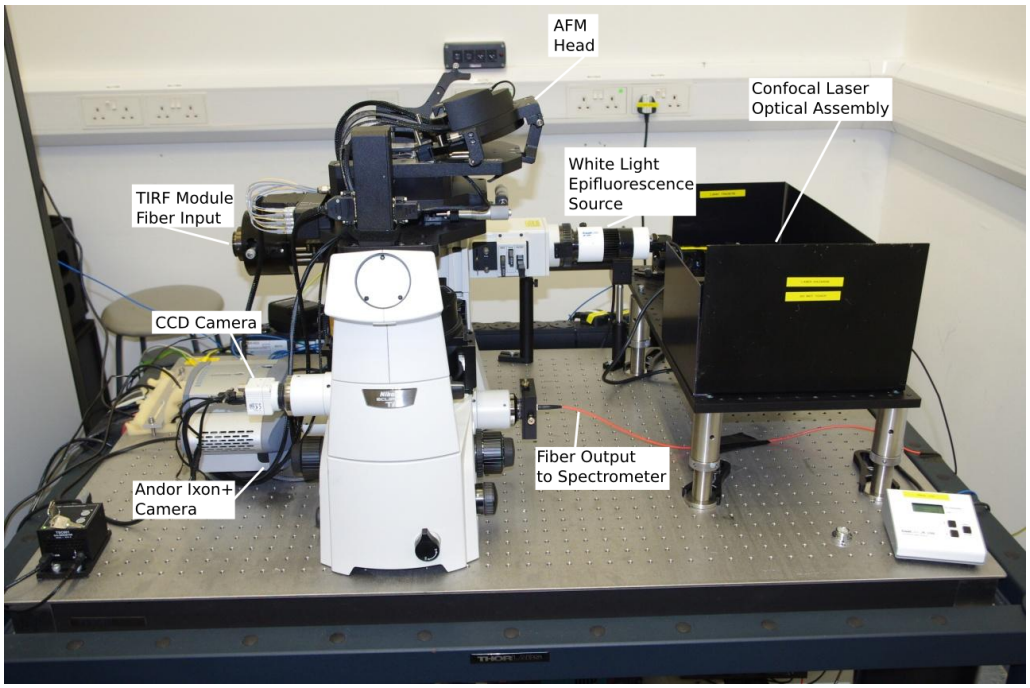

Figure 4.2.: An image of the final microscope setup

The core of the new system is a Nikon Eclipse Ti inverted microscope equipped with two input ports and four output ports. The upper input port on the microscope is coupled to a Nikon TIRF module(Figure 4.3) which has two inputs of its own. An adjustable threaded fibre input and a CoolLED PE-1000 LED white light epifluorescence source. The laser input on the TIRF module had three removable neutral density filters in place when it was received. Since the laser power was always meant to be regulated from the computer and we had already decided that we would need a circularly polarized beam, one of the neutral density filters has been replaced with a quarter wave plate carefully placed to convert the linearly polarized beam to a circularly polarized beam. The lower input port on the microscope is open and receives a collimated laser beam from optics on a raised breadboard positioned next to the microscope(Figure 4.4).

Figure 4.3.: The TIRF module attached to the back of the microscope

Although the microscope is equipped with a rotatable nosepiece equipped for 6 objectives, a PI objective scanner has been fitted to one of the objective ports and different objective lenses are fitted to that as needed. For defocused fluorescence imaging a Nikon Plan Apo 100x 1.49NA oil immersion objective is used, however, there is also access to a 60x, 1.2NA water immersion objective as well as 60x, 40x and 20x air immersion lenses. The objective scanner raised the height of the lens above the level of the nosepiece, where it would be expected to be. The focusing lens in the TIRF module was therefore replaced with one with a 200 mm longer focal length to add the extra distance.

Samples to be imaged are mounted on a PI movable stage mounted on top of the microscope. The stage also has an AFM head designed by AIST-NT attached to it.

Three of the four output ports on the microscope are in use. The left output port is coupled to the Andor camera, the right is coupled to a fibre for confocal and Raman imaging and the auxiliary port mated to the eyepiece is coupled to a Sentech STC-P63 analog CCD camera. The beams from each input port pass through either an upper or lower rotating filter cube holder. Both holders hold

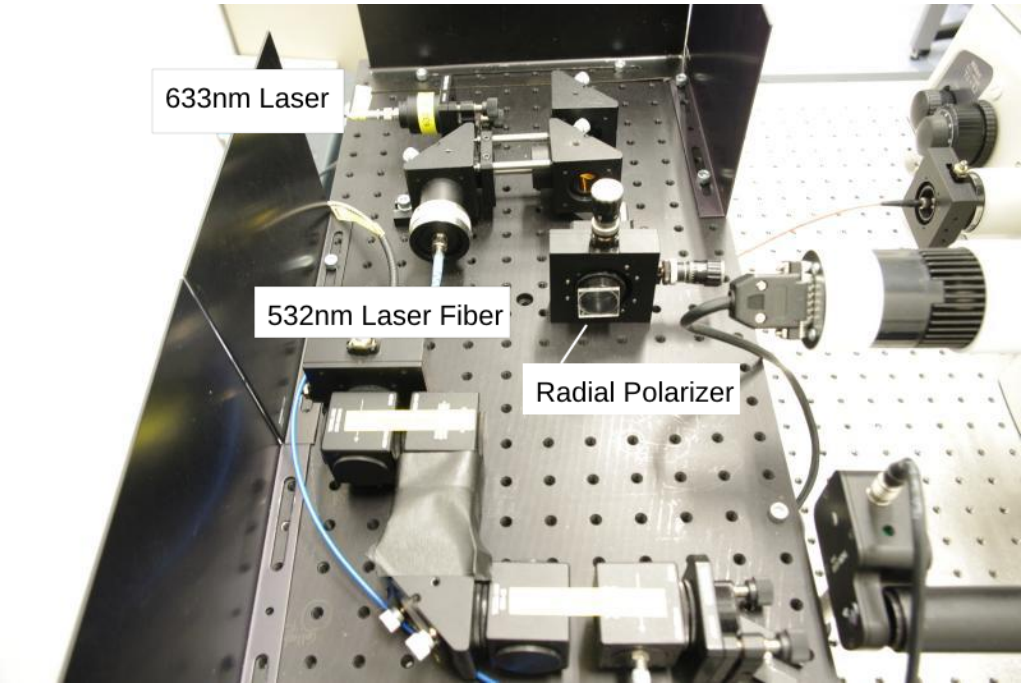

Figure 4.4.: Arrangement of input lasers on the breadboard by the microscope

one cube with 50:50 mirror and another holding both a Semrock BrightLine® 532 nm dichroic mirror and a Semrock RazorEdge® 532 nm low pass exit filter. Additionally, the lower cube holder holds a cube holding a 100% mirror and another holding a 633 nm dichroic mirror and a Semrock RazorEdge® 633 nm low-pass exit filter.

The raised breadboard (Figure 4.4) receives input from two mode-preserving fibres carrying a 532 nm laser beam and a 633 nm laser beam. The beams are individually collimated and cleaned up through Semrock StopLine® notch filters. Both beams are then sent along the same path to a scanning mirror placed behind the lower input port of the microscope.

The shelf below the table(Figure 4.5) provides space to mount a Compass 532 nm and a 633 nm He-Ne laser. The lasers are coupled by mode-preserving optical fibre to either the optics on the table or the TIRF module. The 532 nm laser is also connected to a National Instruments DAC box for controlling the laser power. The 633 nm laser doesn't have a control module and therefore can't be

controlled by computer Altering laser power is therefore achieved by manually opening and closing a shutter. The shelf also holds a spectrometer coupled to an Andor iDus cooled camera and an APD. The spectrometer receives its input from the fibre coupled to the right output port of the microscope.

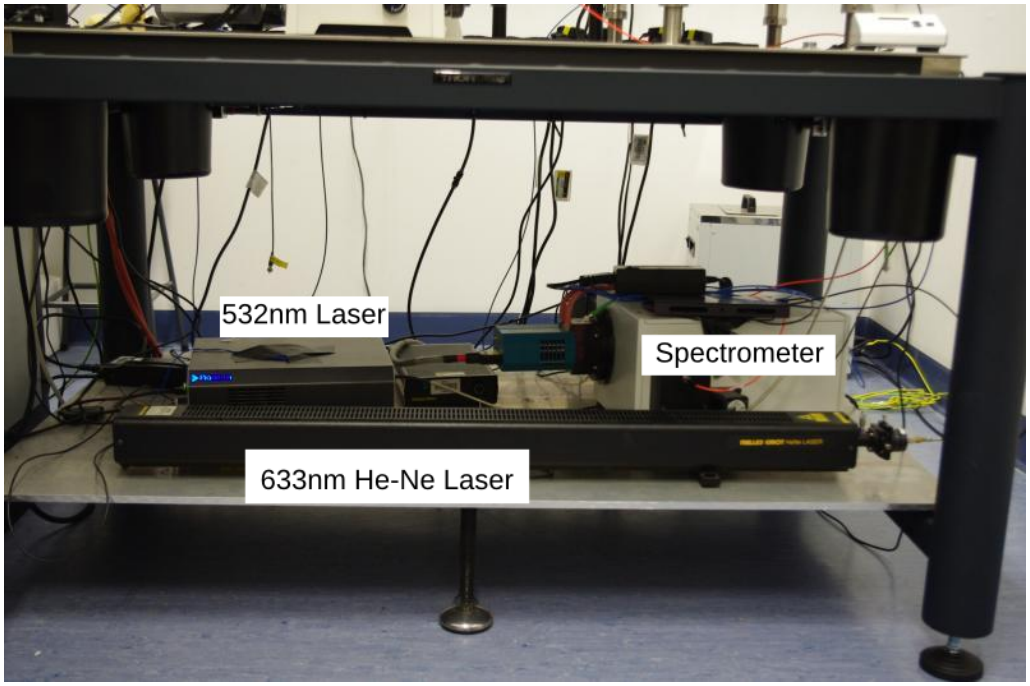

Figure 4.5.: Lasers and spectrometer on the shelf below the optical table

The majority of the equipment on the table is controlled from the 19″ rack next to the table. The PI scanning stage, objective scanner, scanning mirror and the AFM are all controlled from a rack mounted electronics module supplied by AIST-NT that is then connected by USB to the PC. The PC also contains interface cards for controlling the Andor camera and the spectrometer, a NI PCIe-6321 Data Acquisition card connected by an analog connector box to the 532 nm laser and a TV capture card connected to the Sentech CCD camera coupled to the microscope.

4.2. Software and Data processing

The PI stage, AFM head, scanning mirror, spectrometer and Sentech CCD camera were all controlled by the AIST-NT Spectraview software. The National Physical laboratory received one of their first ever on-microscope AFM systems and AIST-NT was required to integrate the existing cameras, APD and spectrometer into the software. The initial versions of the control software contained several bugs that required time and successive releases to correct. By the time the bugs were fixed, the software had also integrated all the hardware connected to the microscope.

The current AIST-NT software is capable of several AFM modes in both air and liquid, scanning confocal microscopy with both the PI stage and the mirror as well as regular and tip-enhanced Raman spectroscopy. The PI stage, objective stage and scanning mirror can also be moved by arbitrary amounts using the software. It is capable of receiving images from both the Andor and Sentech cameras but can not currently save images. There was rarely a need to save images from the Sentech camera, but on saving images from the Andor camera was crucial. This was usually achieved by running the Andor Solis software in parallel with the AIST-NT software to control the camera and saving either single images or image sequences from it.

The AIST-NT Spectraview software saves both the AFM scans and the Raman scans under a proprietary '**.aist**' file format. In order to export AFM data for processing in other software, it was therefore necessary to use Gwyddion,[91] an open source SPM data processing program. Since AIST-NT provides a Gwyddion plugin, it can import the data before processing and exporting it in other software. In the case of the Raman spectral data, it was exported in text form and processed using custom MATLAB scripts.

The 532 nm laser was controlled using a custom LABVIEW™ program adapted from a similar program written by Alex Knight of the National Physical laboratory. The program was used to turn the laser on and off as well as adjust its power levels(Figure 4.6).

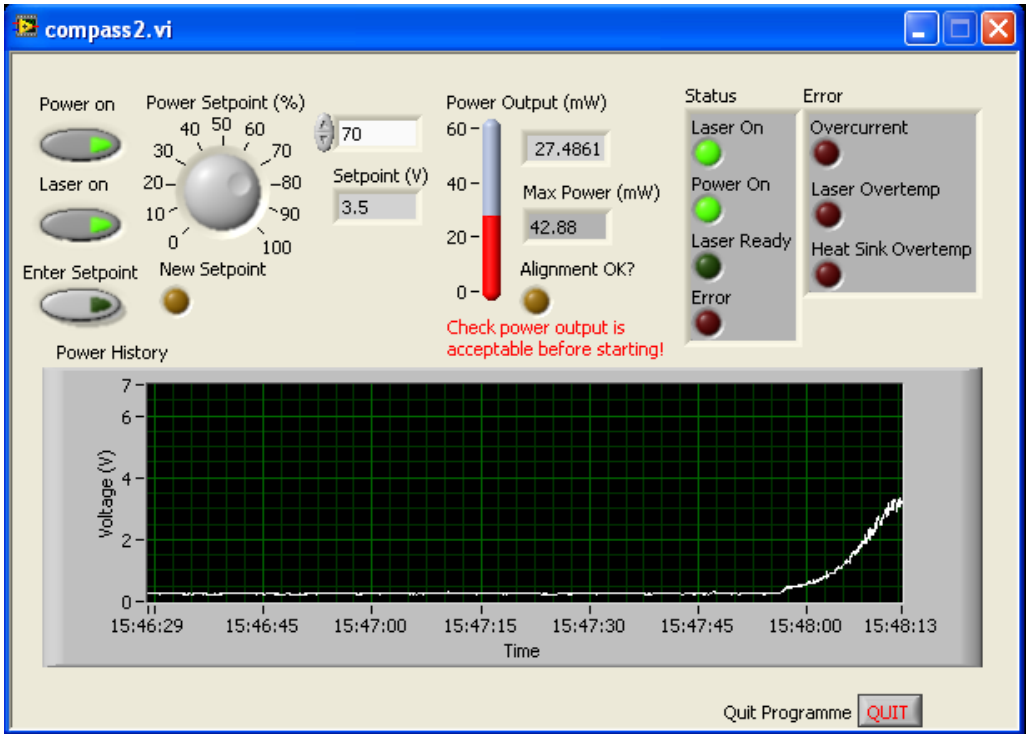

Figure 4.6.: The LABVIEW program controlling the Compass laser

In order to extract the position and orientation data from the fluorescence images, the image files were saved from the camera using the Andor '**.sif**' format. Those files were then opened using a plugin in the imageJ software,[92] background subtraction was performed and the final images were saved as '**.tiff**' images. Those images were then analysed using a MATLAB package obtained from Professor Joerg Enderlein. Details on the nature of the MATLAB package can be found in the Appendix. Once the images had been analysed, personally written MATLAB scripts were used to save an image of the detected images to disk. The position, orientation and least-squares error of the fit for each detected pattern were also saved to a tab-separated text file for further analysis. That analysis was performed using a mixture of MATLAB and Python scripts, with all graphs plotted using the Matplotlib[93] package.

Chapter 5.

Molecular Orientation in Polymer and Lipid Thin Films

5.1. Orientation Measurements In Polymer Thin Films

After completely assembling the microscope, the first order of business was to attempt to prove both that it was capable of defocused single molecule fluorescence imaging and that the workflow for using those defocused images to determine the orientations of individual molecules worked as expected. The initial set of experiments were performed by recreating the type of test sample most commonly used for initial tests of single molecule orientation techniques. These samples were all made up of ultra low concentrations of fluorescent dye embedded in thin polymer films.[29,61,67,68,76]

Immobilising the molecules in polymer thin film prevents them from moving or rotating so their individual orientations are assured to remain constant and can be measured.The polymer of choice was Poly(methyl methacrylate) (PMMA), a polymer chosen because it neither fluoresces nor has a strong Raman signal, so it does not interfere with the fluorescence from the molecules. The fluorescent dye of choice was DilC (DilC_{18}(3) or 1,1′-dioctadecyl-3,3,3′,3′-tetramethylindocarbocyanine perchlorate), a carbocyanine dye with an excitation

peak at 549 nm and an emission peak at 565 nm. Its absorption and emission curves made it ideal for the 532 nm excitation laser attached to the microscope. In addition it has already been used for this purpose in the past because of its strong photostability and high quantum efficiency.[67,68,76]

Making these samples required developing the ability to first reproducibly produce polymer thin films on the surface of a cleaned glass slide and then consistently embed a low enough concentration ($\approx 1 \times 10^{-10}$ mole) of highly dispersed molecules that they appear in the PMMA layer at least 1 µm apart. They need to be at least that far apart because each defocused pattern has a diameter of roughly 1 µm and the pattern matching algorithm fails when patterns overlap.

5.1.1. Making the PMMA layers

The first problem to be solved was working out a process to reliably spin coat PMMA on the surface of a glass cover slip in order to leave behind an even, thin (≈10-100 nm) polymer layer on its surface. This was a fairly well researched process as can be seen from the work of Hall et.al. and Walsh et.al.[94,95] Hall examines the thicknesses of PS (Polystyrene) and PMMA films produced by spin coating solutions of differing concentrations dissolved in chloroform, toluene and xylene while Walsh and Franses are purely interested in the case of PMMA dissolved in toluene.

Walsh and Franses[95] determined that the average thickness d_1 (in μm) of polymer films produced by spin coating could be described in the form of $d_1 = Ac^n\omega^{-m}$ where c is the percentage by weight of polymer dissolved in solvent and ω is the speed of spin coating in RPM. A, n and m are dependent on the polymer being used and the solvent it is dissolved in. Hence, for a given polymer dissolved in a specific solvent, the parameters responsible for film thickness are dependent on the concentration of the polymer in solution and the speed of the spin coater. For PMMA dissolved in toluene they found values of $A = 0.92$, $n = 1.56$, $m = 0.51$ provided the best fit to their data. Figure 5.1 shows the predicted film thicknesses for PMMA solutions of differing thicknesses spun with at 2000, 3000 and 4000RPM.

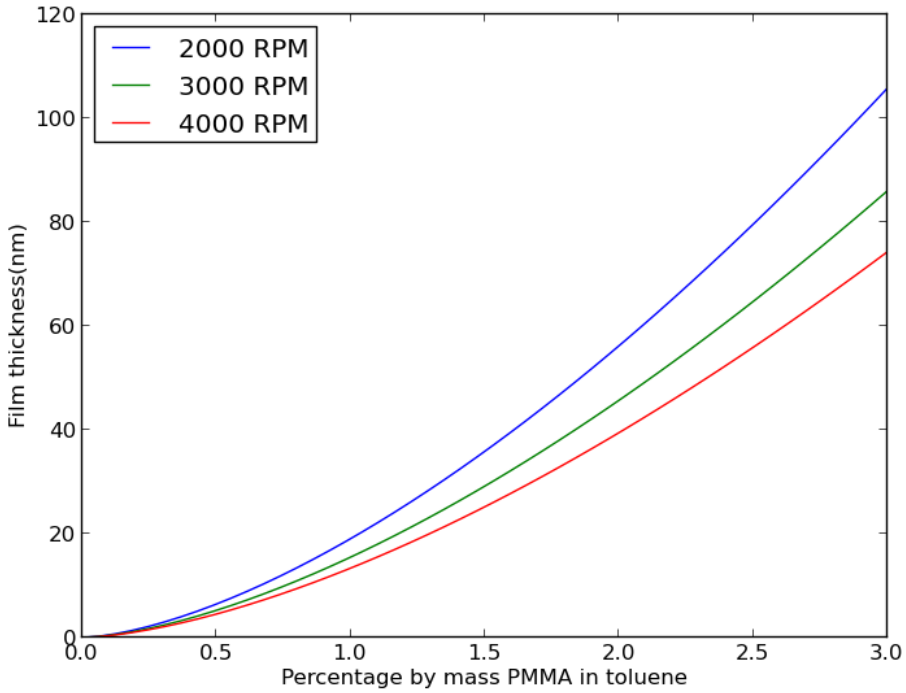

Figure 5.1.: A graph of the average film thickness of PMMA thin films spin coated to a smooth surface at speeds of 2KRPM, 3KRPM and 4KRPM as predicted by the formula $d_1 = 0.92c^{1.56}\omega^{-0.51}$, where c is the concentration by mass of PMMA in toluene and ω is the spin velocity.[95]

To confirm these numbers, low molecular weight PMMA (15,000Mw, Sigma-Aldritch) was dissolved with varying concentrations in toluene (0.5%, 1% and 5% by mass) and spun on 24 mm×24 mm Menzel-Glaser cover slips. The cover slips were first cleaned by immersion in a concentrated solution of KOH in ethanol and rinsed off successively in DI water and isopropanol. They were then dried in a stream of Argon gas. The slides were then placed in a Laurell WS-650Z-6NPP/LITE spin coater. To form the PMMA layer, 60 µl of dilute PMMA solution was pipetted on the surface of the slide and then spun at speeds of 2000, 2500, 3000 and 4000 RPM for 1 minute. Three slides were produced for every permutation of concentration and spin speed.

The samples were then characterised in a J. A. Woollam XLS-1000 ellipsometer. Readings were taken at inclination angles of 50°, 60° and 70°. The results were

analysed using the included software which compared them to a constructed model for the behaviour of a two layer dielectric with the properties of a PMMA film on a glass slide for light in the range of 300 nm-1400 nm. The mean results obtained for each set of parameters are shown in Table 5.1.

Table 5.1.: Mean film thickness (nm) across 3 slides each for different concentrations of PMMA at multiple spin coater speeds

	2K	2.5K	3K	4K
0.5%	11±1nm	8±1nm	7±1nm	6±1nm
1%	17±2nm	16±2nm	14±1nm	13±1nm
5%	178±1nm	169±2nm	163±1nm	156±1nm

It was decided that the slide used in the experiments would be a cleaned glass slide with a 10 nm thick PMMA layer spun on top of it. From Figure 5.1 and table 5.1, it can be seen that 1% by mass PMMA spun at 3KRPM for 1 minute should provide an appropriate sample, hence that became how all the slides were constructed.

5.1.2. Dispersing Dye Molecules

Once the process of creating the PMMA thin films had been established, the next step was to embed a low concentration of fluorescent dye in the PMMA layer for imaging. The ideal test sample was one with dye molecules sparsely and evenly distributed in the PMMA layer in a way that they could be individually resolved with a separation distance of $\approx 1\,\mu m$.

In order to perfect the process of embedding single fluorophores, triple shell quantum dots (CdSe\CdS\ ZnS) were obtained from Professor Mark Green of the King's College London physics department to be used in place of DilC molecules. The choice of quantum dots to begin with is because they provide brighter light sources than fluorescent molecules making them easier to image. Also, unlike single molecules, they can be easily imaged by AFM and thus confirm the relatively

even dispersion of the quantum dots on the PMMA surface. The samples are provided suspended in toluene at an undetermined concentration.

To make the samples, first the quantum dot solution was placed into a SIGMA 3K30 centrifuge and spun at 7000 RPM for 30 minutes to remove the clumps of quantum dots from the suspension. A pipette was then used to remove the top layer of the solution and multiple $^1/_{100}$ dilutions of that were made in 1% toluene/PMMA solution. The diluted solution was then sonicated for 30 minutes to properly disperse the quantum dots. These multiple dilutions were then spun on glass slides, mounted on the microscope and imaged with a 532 nm laser under TIRF until a sample showed an adequate level of dispersed quantum dots. An AFM image of one of the final samples clearly showing quantum dots dispersed and embedded in PMMA can be seen in Figure 5.2.

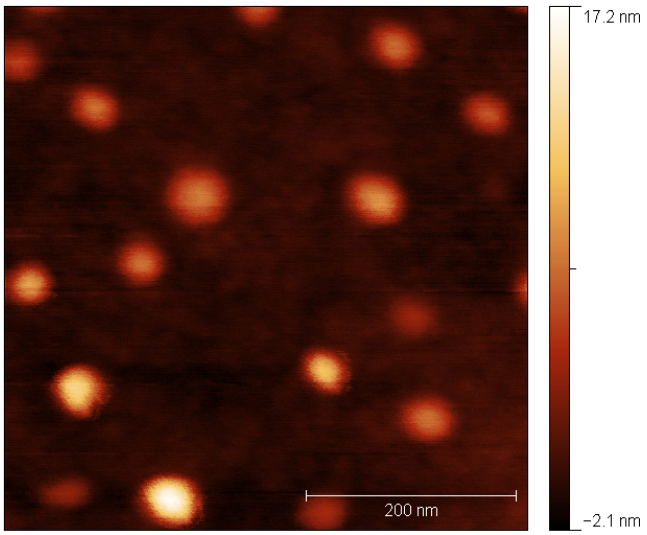

Figure 5.2.: An AFM scan of a test sample of CdSe\CdS\ZnS quantum dots embedded in a $\approx$ 10 nm thick PMMA thin film. The variation in spot size is mostly a function of how deeply embedded the quantum dots are in the PMMA film.

The images of dispersed quantum dots embedded in the PMMA layer confirmed that the process of dispersing single quantum dots in the PMMA layer was an effective one and could therefore be applied to DilC molecules. A crystalline version of DilC was obtained from Invitrogen and dissolved in toluene

at a concentration of 1×10^{-3} mol. As with the quantum dots sample, the DilC solution was diluted by $\frac{1}{100}$ increments with a PMMA solution in toluene, spun on a cleaned glass slide and imaged. Eventually it became clear that 1×10^{-11} mol of DilC dissolved in toluene along with the PMMA resulted in a sample with molecules dispersed far enough apart to make them ideal for examination.

5.1.3. Orientation of Dye Molecules in PMMA

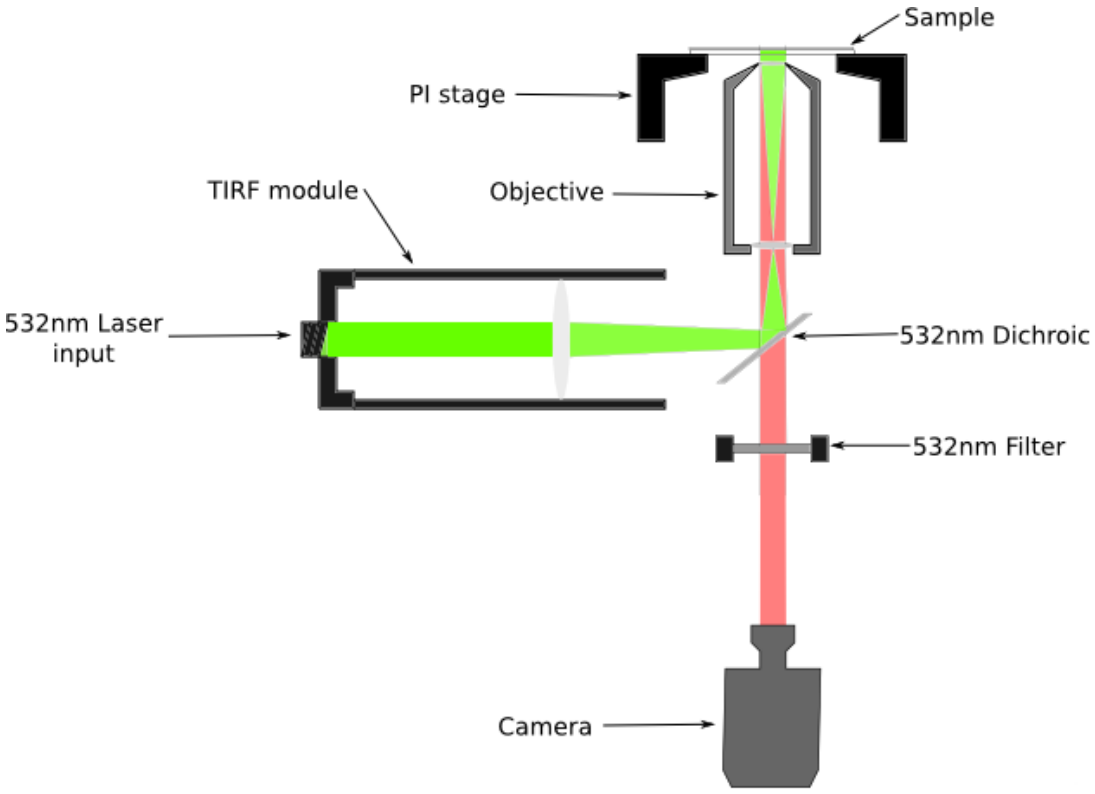

Figure 5.3.: System setup for defocused epifluorescence imaging

Once the process of creating the samples had been finalised, a new sample was made by spinning a PMMA\DilC solution on a 18 mm×18 mm Menzel-Gläser glass cover slip. The fluorescence from the individual molecules was then imaged. The system used for imaging the fluorescent molecules can be seen in Figure 5.3. A linearly polarised 532 nm laser beam was coupled by means of a mode preserving

fibre to the objective TIRF module attached to the microscope. The beam was then converted to a circularly polarised beam by use of a quarter wave plate. The TIRF module was adjusted to focus the laser off a 532 nm dichroic mirror to the centre of the back aperture of the objective, resulting in a collimated, circularly polarised beam arriving normal to the sample. The polarisation of the beam was confirmed by placing a polarising filter between the laser beam and a laser power meter, then changing the orientation of the filter and observing changes in the power of the laser. The sample was mounted on the PI stage over the objective.

The fluorescence from the excited molecules was then filtered through the dichroic and a 532 nm long pass filter before being focused on the EMCCD camera. After the images were manually brought into focus, the AITI software was used to defocus the image by moving the PI stage exactly 600 nm towards the objective. The Andor software was used to capture the defocused fluorescence images with integration times between 1 and 5 seconds.

The captured images were imported into MATLAB, background subtraction was performed and the pattern matching algorithm originally developed by Enderlein was used to compare the located patterns with those produced by the fluorescence from dipoles located at the interface between a glass cover slip and a 10 nm thick film with the same refractive index as PMMA (1.49) and defocused by 600 nm. Each pixel in the image was taken to represent a 160 nm square. The results of this can be seen in Figure 5.4 and serve as preliminary confirmation of both the microscope and the technique.

5.1.4. Exploring The Effects of Illumination Type and Polarisation

After establishing the effectiveness of the technique, the next step was to examine the different results that could be produced by altering the polarisation of the laser beam and to compare the results produced by illuminating a test sample via epifluorescence laser illumination as opposed to objective quasi-TIRF illumination.

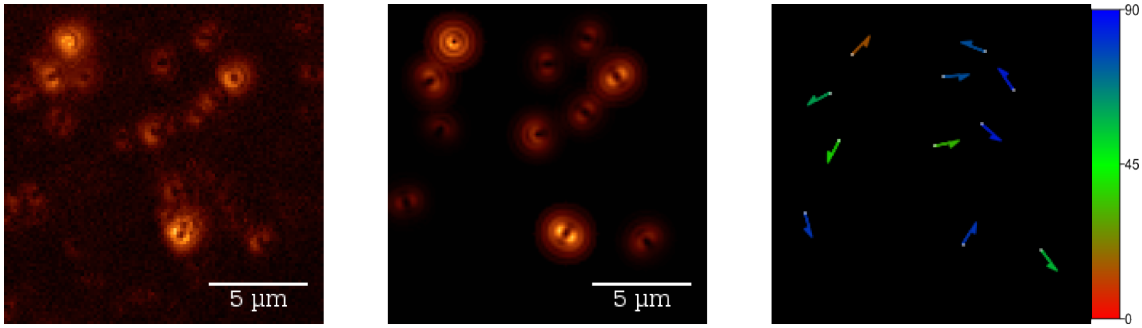

(a) Original Image (b) Reconstructed Image (c) Position and Orientation

Figure 5.4.: (a) Defocused images of single fluorescent molecules, (b) the patterns recognised by the image recognition routines and (c) a composite image with coloured arrows showing the individual positions and orientations of each fluorescent molecule. The direction of the arrow indicates the azimuthal angle ϕ and the colour of the article indicates the polar angle θ. The position of each molecule is localized to within a 160 nm $\times$ 160 nm pixel and orientation in both θ and ϕ has an uncertanty of $\pm 2.5°$

Figure 5.5 represents histograms for the θ and ϕ orientations of the molecules observed on the surface of a sample illuminated with linearly and circularly polarised epifluorescence respectively. In this case, the linearly polarised light was always p-polarised. Relative to the camera, the axis of a p-polarised beam would be oriented at $\phi = 90°$ and $270°$. Upon comparing the differences in ϕ orientation between the two figures, was expected that the circularly polarised laser would have resulted in evenly illuminated molecules across the range while the p-polarized beam would have resulted in distributions clustered about $\phi = 90°$ and $270°$. The experimental results defied expectation with the results from both sets of beams clustering around two peaks separated by $180°$, implying that the beam was not as circularly polarised as expected.

It has been shown[96] that the z-axis excitation achieved using epifluorescence excitation with the laser normal to the sample interface is not entirely uniform. This results in molecules oriented with their absorption dipoles parallel to the interface being more likely to be stimulated than molecules oriented with their dipoles perpendicular to the interface. Their three-laser solution is one possible solution to the issue, but is also unwieldy and complicated to set up. A simpler alternative is quasi-TIRF illumination, which can also improve the polar excitation.[30] Quasi-

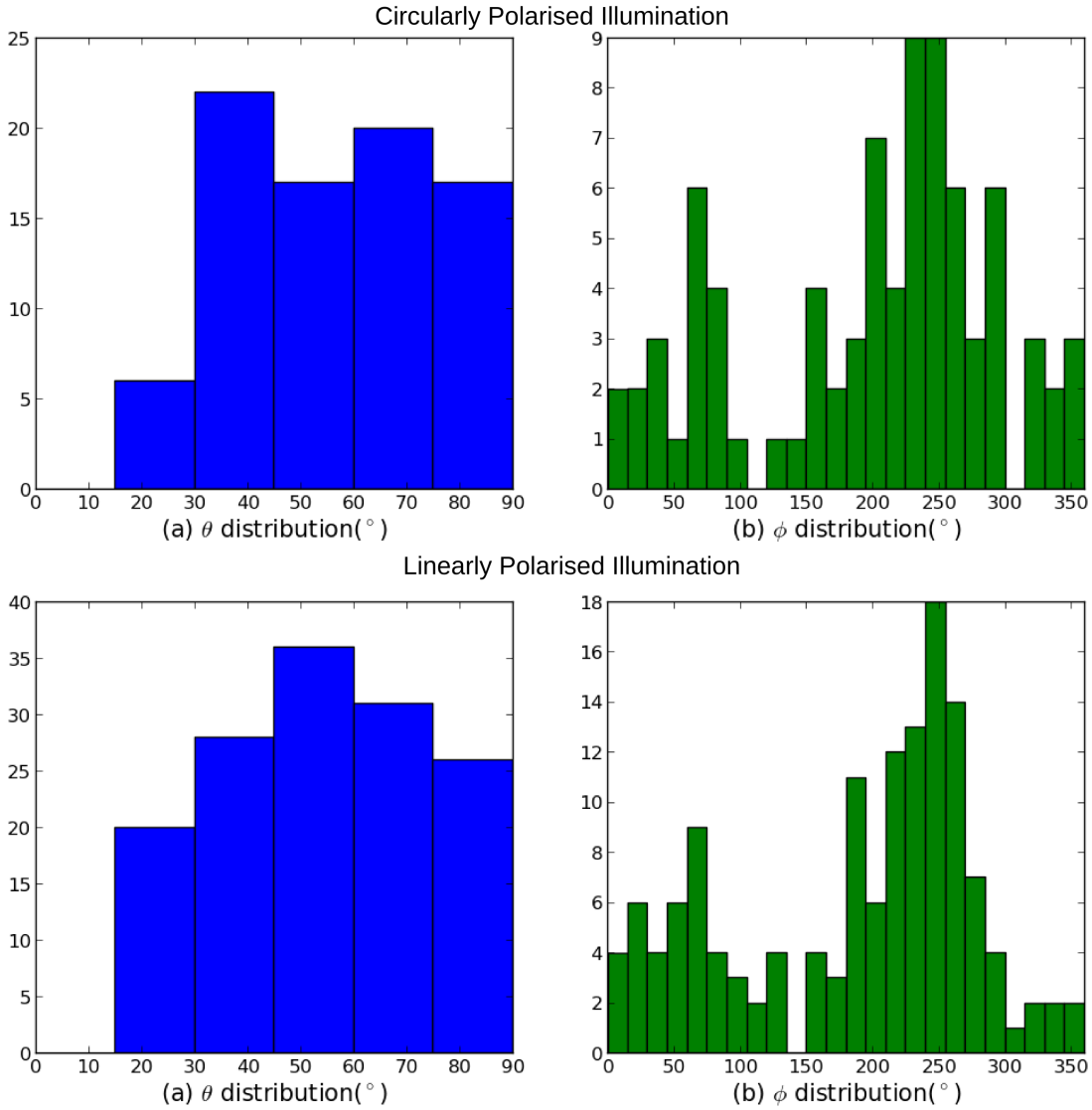

Figure 5.5.: ϕ and θ distributions of DilC molecules embedded in PMMA illuminated by circularly and linearly polarised laser light

TIRF illumination involves the use of an objective TIRF instrument to illuminate a polymer-covered glass surface at the highest possible incident angle. Since the polymer layer is so close in refractive index to the cover slip, a 1.49NA objective is still unable to provide a beam at a high enough angle to get complete TIRF between the cover slip and the polymer layer. Therefore part of the incident beam reflects off the glass-polymer interface and the rest of the bean is reflected off the

polymer-air interface. This creates a very complicated polarisation picture in the polymer layer, but one with a stronger z-axis component. Luckily, quasi-TIRF is a lot simpler to implement since the imaging system in already makes use of an objective TIRF module.

In order to test out the difference between epifluorescence and TIRF illumination, the same sample was reused and the objective TIRF module adjusted to shift the position of the laser so that it no longer arrived at the centre of the back aperture of the objective, but instead arrived at the side. This led to a laser beam coming out of the objective at angle (60°) to the surface that was greater than the critical angle of the PMMA/air interface, leading to internal reflection off the interface[97,98] and a highly angled beam illuminating the PMMA layer in a way that should have illuminated molecules oriented closer to the z-axis. As with the first set of tests, linearly (p-polarised) and circularly polarised light were used to illuminate the sample and the results analysed as before.

The ϕ histograms for Figure 5.6 show that quasi-TIRF illumination provides more even coverage than linear excitation. It seems that the nature of polarisation matters less for quasi-TIRF illumination than it does for normal epifluorescence illumination. Examining the θ histograms between Figures 5.5 and 5.6 however, did not show that using quasi-TIRF excitation appears to excite more molecules polarised at high angles. Assuming that the DilC molecules were evenly distributed throughout the sample, the θ angle distribution should have been close to $sin(\theta)$. However instead, all the distributions looked the same. Relatively even at all angles except for 0° - 15°. However, there is already evidence that the orientation distribution of fluorescent molecules in polymer thin films is affected by film thickness[96] and so the 10 nm film thickness could have had an effect on the θ distribution.

Habuchi et.al. also proposed and tested a three laser illumination setup as an alternative to epifluorescence imaging.[96] The proposed setup can be seen in Figure 5.7 and works by adding side illumination from two extra lasers at 40° tilt angles in order to result in a more uniform probability for the excitation of fluorescent

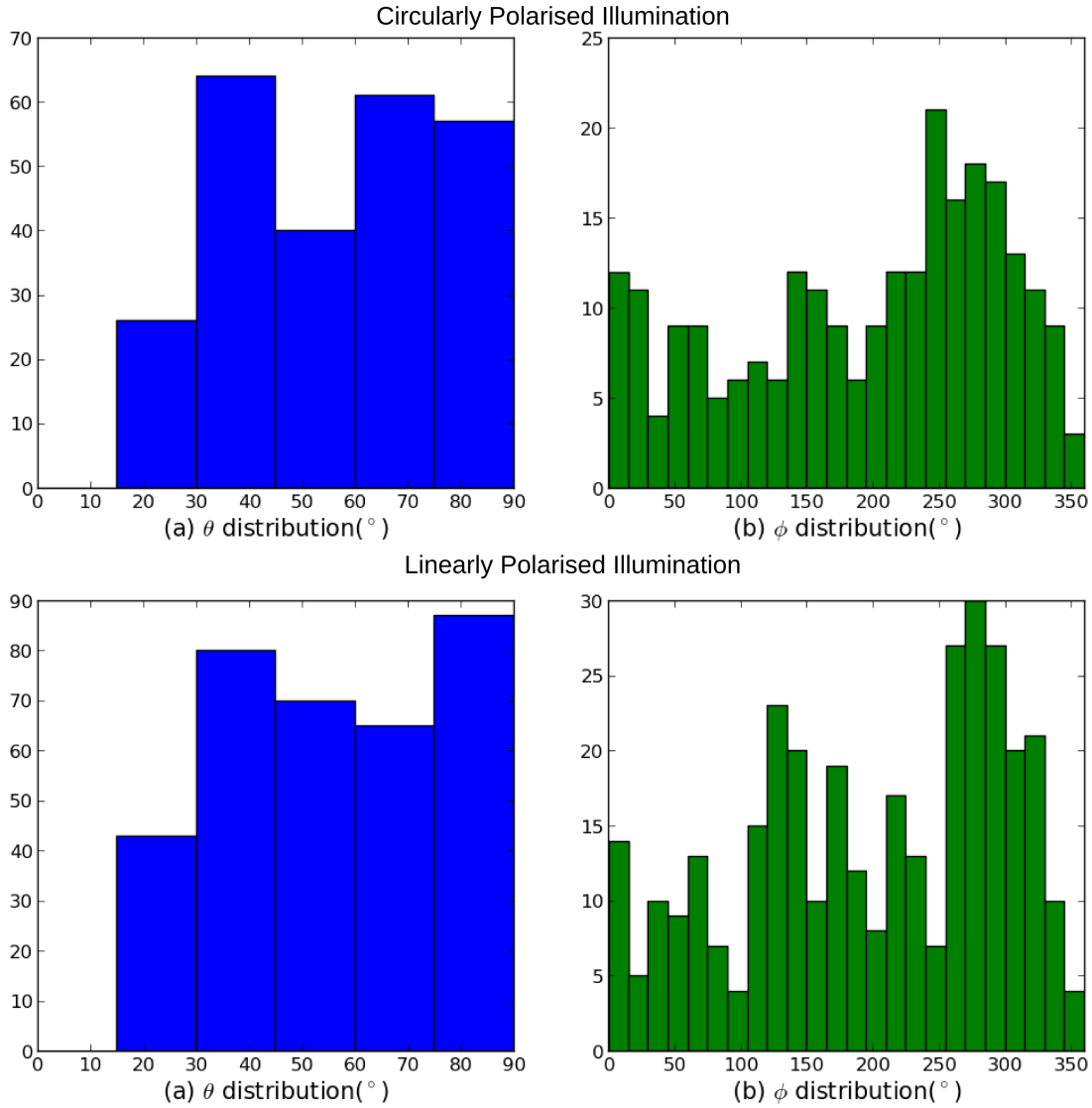

Figure 5.6.: ϕ and θ distributions of DilC molecules embedded in PMMA illuminated in TIRF configuration by circularly and linearly polarised laser light

molecules regardless of orientation. Unfortunately, it was not a system that we could fit into the microscope. It is definitely worthy of investigation though.

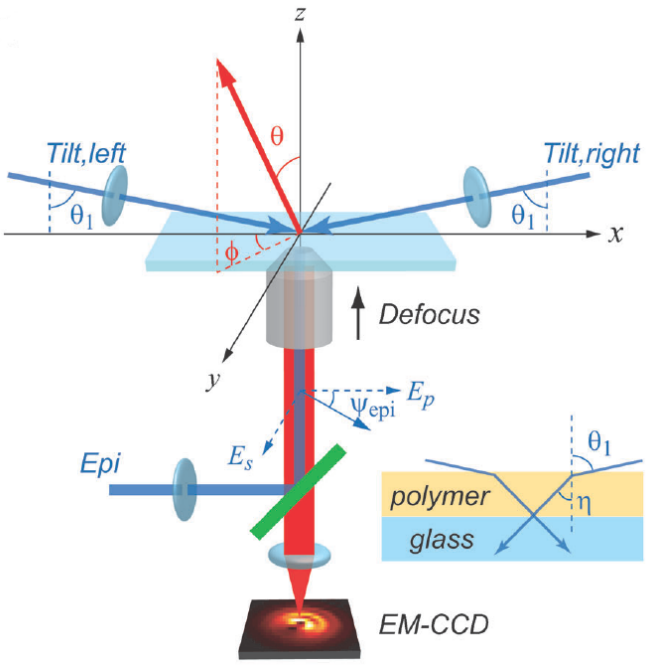

Figure 5.7.: Proposed three-angle laser illumination setup[96]

5.1.5. Ideal Integration Times

I was also interested in quantifying how much time was actually needed to produce good patterns on this particular test system. To determine this, a new test slide was produced identical to the ones used in the dye-PMMA characterisation experiments. The slide was then placed on the inverted microscope and illuminated by a circularly polarised 532 nm laser normal to its surface. The resulting fluorescence signal was filtered and focused on the EMCCD camera. The stage was used to defocus the image by moving the sample 600 nm closer to the objective. The resulting defocused patterns were then recorded with exposure intervals ranging from 100 ms to 10 s at 10 randomly chosen points on the surface of the sample. Since all 10 points were on the same sample, the imaged areas on the surface should all have roughly the same number of fluorophores present in the field of view (82 µm × 82 µm). An example of a defocused pattern at different integration times can be seen in Figure 5.8

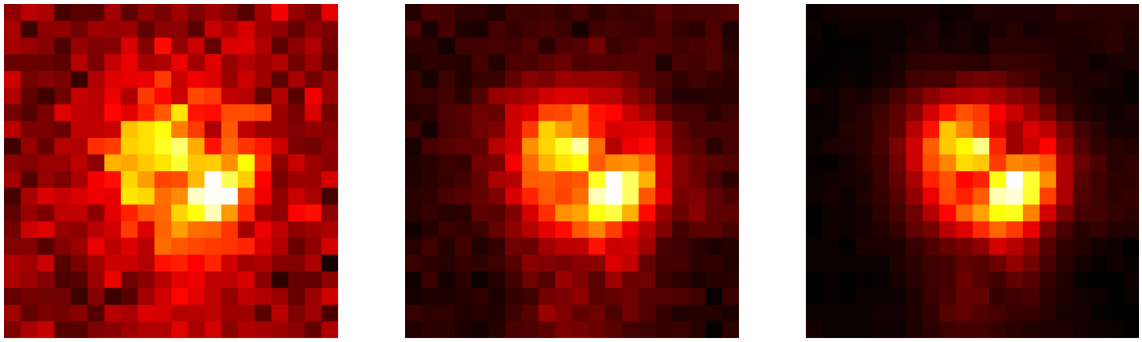

Figure 5.8.: Defocused imaging of Dil molecules embedded in PMMA at different integration times

The obtained images were then processed through the pattern recognition algorithm. The position, orientation and least-squares error values for each pattern were recorded. The collected data was then used to calculate the mean number of detected patterns and the mean least-squares error per integration time per sample region. The least-squares error value of an individual fitted pattern is of limited use, since it has already passed the threshold for fitting. Examining their distribution

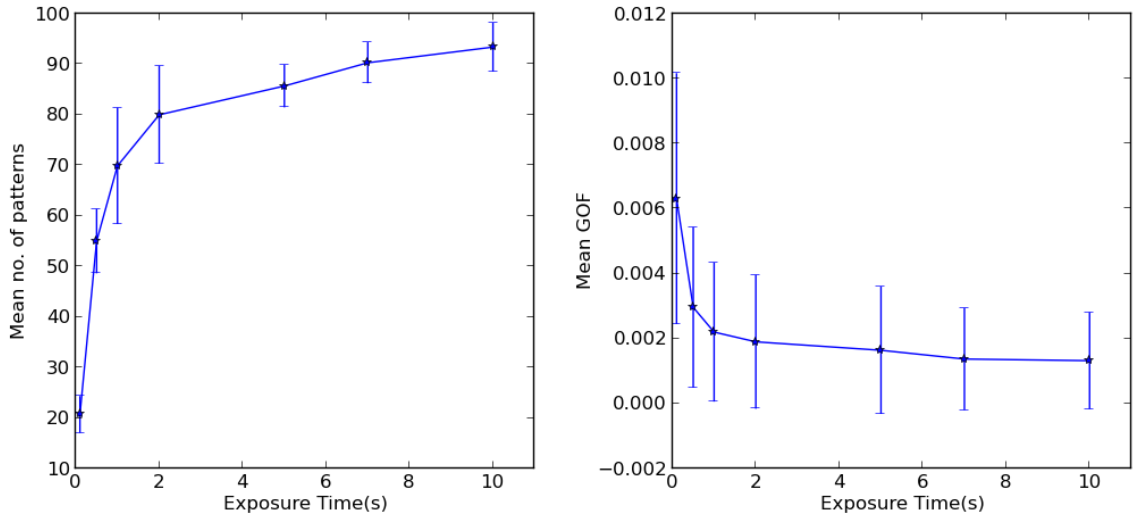

Figure 5.9.: Graphs of number of detected fluorescence patterns and mean least squares error against integration time. The error bars represent the standard deviation across 10 measurements

As can be seen from Figure 5.9 the least squares error of our detected fluorophores begins to asymptotically approach a minimum at about 0.5s - 1s of integration time. The mean number of detected patterns asymptotically approaches the maximum number of detectable patterns in the field of view in the same time scale.

From the results it appears that in order to obtain a reasonable number of patterns that can be detected with consistently low least-squares error values, it is necessary to employ integration times of 500 ms or more, making that the physical limit for the current experimental system. Longer integration times will yield more patterns, but long exposures will also lead to the bleaching out of molecules.

5.2. Orientation Measurements in Lipid Thin Films

Individual lipid molecules are amphiphilic molecules that are hydrophobic on one end and hydrophilic on the other.[99] Lipid bilayers therefore form in solution from two monolayers with the hydrophobic ends facing inwards and the hydrophilic ends facing the water. They are of interest primarily because of their ubiquity in cell membranes.

Several methods have been employed in the study of lipid monolayers and bilayers. These include Atomic Force Microscopy (AFM),[100,101] X-ray crystallography,[102] Nuclear Magnetic Resonance (NMR), molecular modelling[103] and, most relevant for the purposes of this thesis, fluorescence microscopy. Fluorescence imaging of the lipid bilayers generally involves either the use of dyes whose molecular structure allows them to attach themselves to lipid bilayers or lipid molecules functionalized with dye molecules on their hydrophilic head groups. Since the introduction of dye molecules into a bilayer in bulk may alter its structure in a significant way, the reaction of lipids to different dye molecules has been a subject of investigation.[104–106] Fluorescence imaging has also been used to investigate the rate of movement of dyes in a lipid bilayer to determine the dynamics of internal molecular transport.[107,108]

All of the previous experiments were performed as bulk measurements on bilayers. Those measurements, while useful, are not necessarily sensitive enough to measure changes taking place in very small volumes of the bilayer, plus there remains the disorder resulting from the introduction of dye molecules into the bilayer. The ability to use single molecule measurements instead has the advantage of being able to detect those small area effects while simultaneously reducing the potential effect the fluorophores have on bilayer ordering.[109] With the emphasis on tracking the local ordering of bilayers, the ability to measure the orientation of the embedded dye molecules is clearly relevant.

Defocused single molecule orientation measurements have already been used via TIRF imaging to examine the orientations of very low concentrations of dye (DilC, BODIPY-PC) introduced into DPPC bilayers (1,2-dipalmitoyl-sn-glycero-3-phosphocholine) and Langmuir-Blodgett films. In the case of the monolayers they were used to examine the changes in ordering caused by subjecting them to varying levels of pressure during creation. Cholestrol, ergosterol and lanosterol were also introduced to the monolayers and bilayers to see what effect it had on their local ordering.[36,37] Ordering changes in DPPC bilayers as a function of changes in humidity have also been investigated using defocused fluorescence orientation measurements[38] In all cases, the changes in ordering could be detected from the changes in individual fluorophore orientation.

DilC, the dye used in the previous section, is a lipophilic dye and is used in fluorescence experiments specifically because of its tendency to bind selectively to the lipid molecules in a cell membrane in an orientation-specific manner.[110] This has been confirmed experimentally on more than one occasion, the first being by the use of fluorescence polarisation microscopy to show that DilC molecules in red blood cell membranes attached themselves with their emission dipoles close to parallel with the surface of the cell membranes.[51]

The interactions between DilC molecules and lipid bilayers has also been subject to investigation via both experimentation and molecular modelling.[111,112] Molecular dynamics simulations have been used to model the interaction between DilC molecules and DPPC lipid bilayers (Molecular structures in Figure 5.10). The

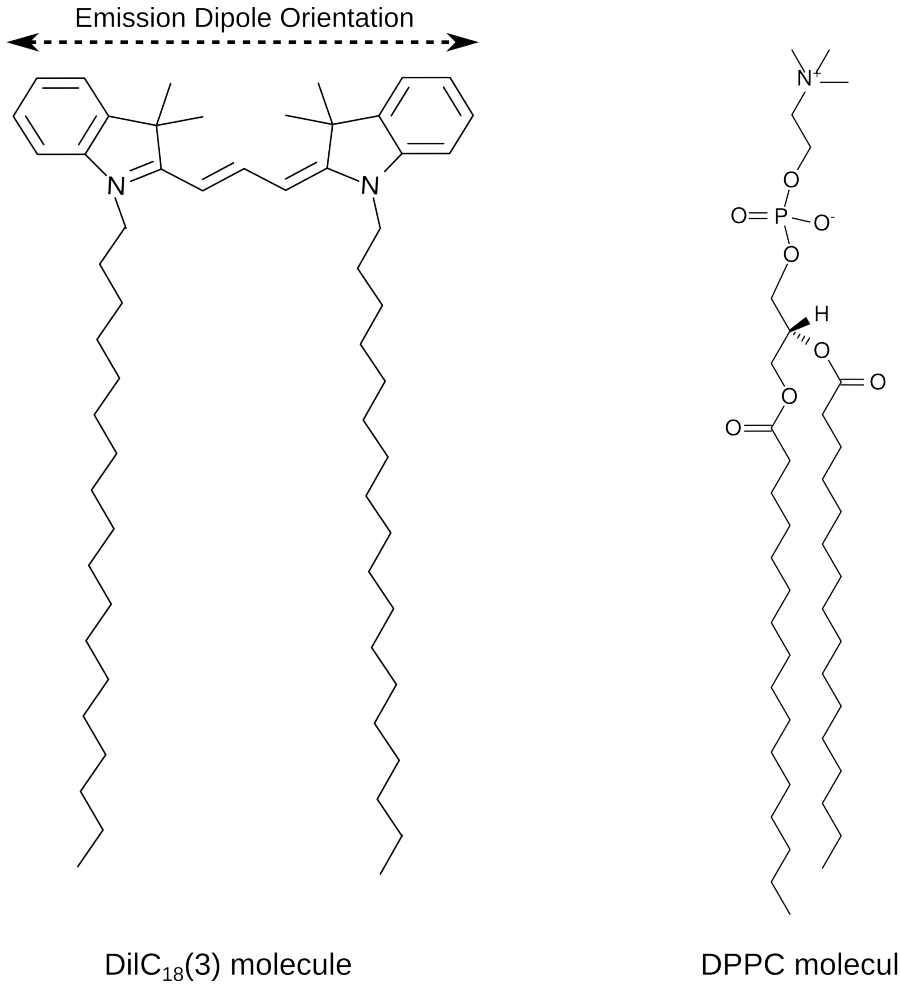

Figure 5.10.: The molecular structures of $DilC_{18}(3)$ and DPPC molecules

simulation results agree that the DilC molecules insert themselves into the space in between the two monolayers below the lipid-water interface with their head groups almost parallel to the bilayer surface (Figure 5.11). An attempt was also made to quantify the exact orientation of the dye molecule in the membrane with the results predicting an angle of $77° \pm 17°$ relative to the normal of the bilayer.[111] This presents us with a possible system that should be fairly simple to investigate.

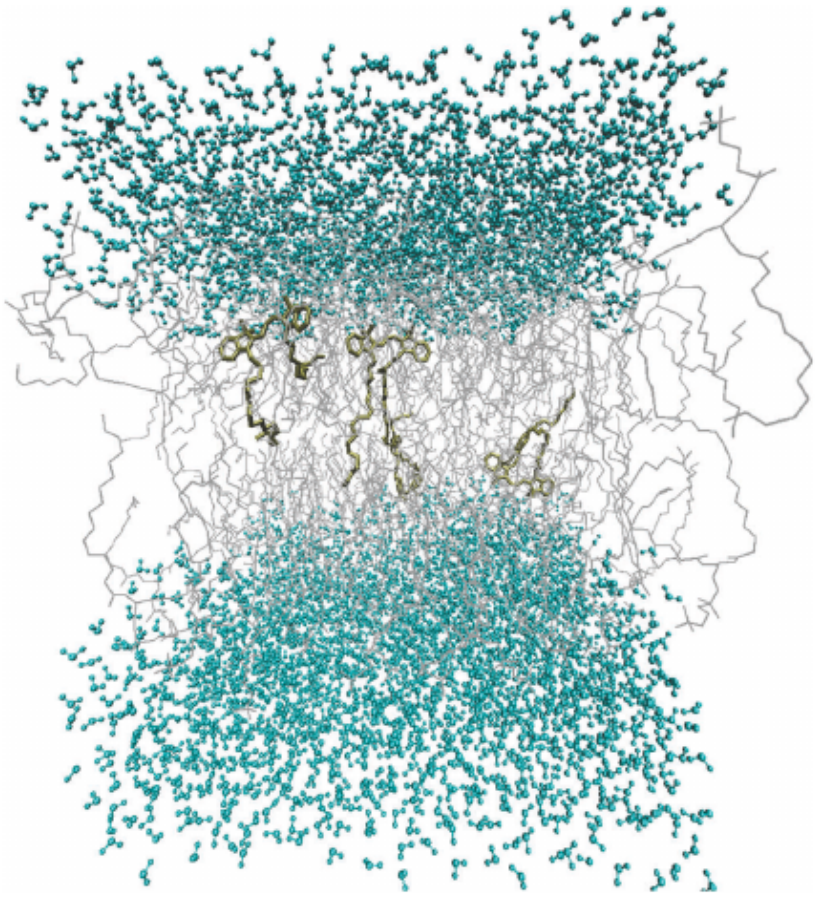

Figure 5.11.: A simulated thin film containing 4 DilC molecules, 128 DPPC molecules and water. The Dil molecules are all below the lipid-water barrier with their head groups almost parallel with the bilayer surface[111]

5.2.1. Creating Synthetic Lipid Thin Films

In order to investigate the ordering of lipid bilayers, it was first necessary to be able to make fairly continuous synthetic bilayers on glass cover slips embedded with low concentrations of fluorescent molecules. Essentially similar samples to what we'd produced in for use with PMMA, but this time on a thin film sample whose nature should force the θ orientation of the fluorophores into a very small range.

The lipid creation process is similar to the one used by Jascindra Ravi and Paulina Rakowska of the National Physical Laboratory's biotechnology group . The lipid molecule used in this case is DPPC, purchased in powder form from Avanti Polar Lipids Inc. Small amounts of the lipid were dissolved in a 3:1 mixture of chloroform and methanol. The mixture was then dried in a stream of argon gas leaving a thin film on the sides of the container. The container was then left to completely dry in a vacuum chamber/dessicator. Enough Milli-Q water was added to make up a $4\,\mathrm{mg\,ml^{-1}}$ mixture of lipid to water. The solution was then vortexed for 30 minutes before being sonicated in a 30 °C water bath for another 40 minutes. This resulted in a mostly clear suspension of the lipid vesicles in water. In order to properly disperse the dye molecules, 100 ml of 1×10^{-10} mol dye dissolved in ethanol was added to the water prior to sonicating.

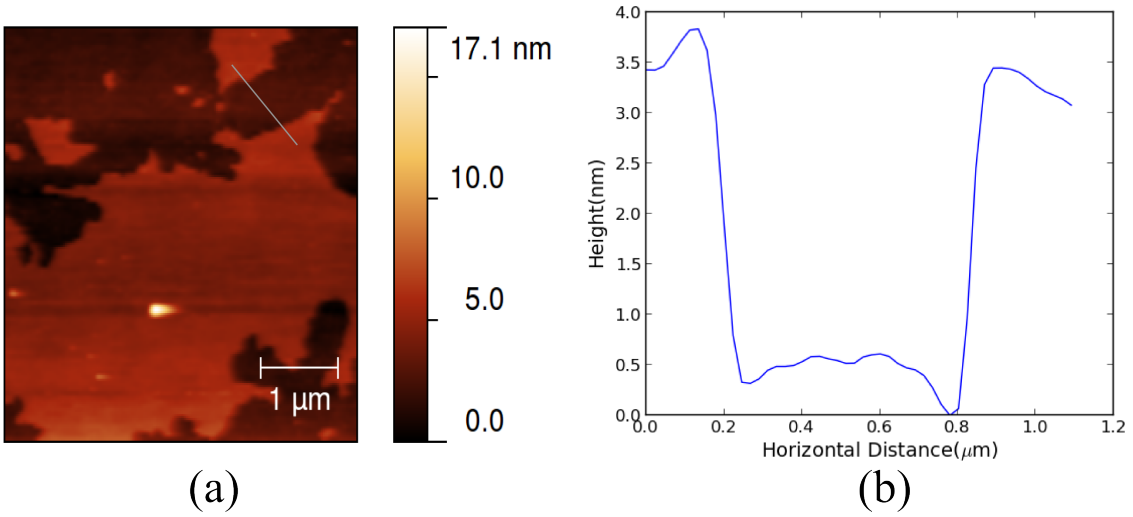

Figure 5.12.: AFM scan (a) and height profile (b) of lipid bilayer on a glass cover slip. The grey line indicates the source of the profile

The glass slides were cleaned for 15 minutes in a saturated solution of KOH in isopropanol. They were then sonicated for 10 minutes in an ethanol bath and dried under a stream of argon gas. Each slide was placed into a container, covered with the lipid suspension and left for 2 hours while the lipids self-assembled on the surface of the glass. After 2 hours, each slide was rinsed off in Milli-Q water and placed back in its container, which was filled up with water and sealed. The sealed containers were flash frozen in liquid Nitrogen and left to dry under

a vacuum pump with an attached condenser. The vacuum caused the melting ice to immediately evaporate off the surface of the slide leaving behind a dried continuous lipid bilayer on top of the glass slide.AFM scans performed on the resulting samples showed continuous bilayer patches on the order of a few square microns in area separated by short distances. An example of this can be seen in Figure 5.12. The height of the layers was consistent with that of a single bilayer.

5.2.2. The Orientation of DilC Molecules in DPPC Thin Films

The lipid samples were imaged in exactly the same way as the PMMA samples. They were mounted on the microscope and illuminated via a collimated, circularly polarised beam normal to the surface of the slide. The resulting fluorescence was then filtered through a dichroic and a low pass filter before being focused on the cooled EMCCD camera. The images were again loaded into the MATLAB pattern recognition routine and analysed using the same parameters as those used for the PMMA layer, except using a refractive index of 1.47 for the DPPC bilayer.

The polar distribution of DilC molecules in phospholipid bilayers has long been predicted by both experiments and molecular modelling to be close to $\theta \approx 90°$, however, as can be seen in Figure 5.13 the lipid orientation clusters around a mean of 41° and a standard deviation of 16°. This is a rather significant deviation from the expected results.

The best explanation currently available comes from work done by collaborators at the Karlsruhe Institute of Technology to make lipid bilayer nanostructures with DilC embedded in them. Repeatedly it was found that the DilC molecules would migrate outside the lipid bilayer structures self assembled on glass slides in a similar manner to the continuous bilayers under investigation. They are currently looking for a solution by changing the kind of glass used in the slides. Assuming the same phenomenon is happening with the lipid layers, that would imply the DilC molecules being imaged have migrated out of the lipid layer and are on the edge of the layer or the glass slide. This would explain how the polar

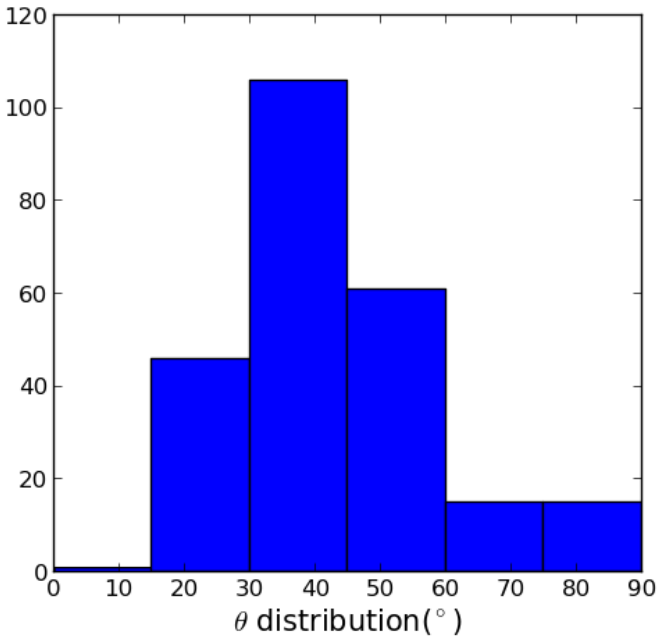

Figure 5.13.: The polar angle distribution of DilC molecules embedded in synthetic DPPC bilayers

angular distribution can remain as constrained as would be expected, but be oriented closer to vertical than to be horizontal.

5.3. A Novel Method of Single Molecule Orientation Measurements

From the first set of observations, it can be seen that the amount of time required to collect enough photons to obtain a reliable defocused fluorescence image with a reasonable signal/noise ratio using wide field illumination ranges from 1 s to 5 s. This is too slow for observing orientation changes and other physical and chemical activities that happen at substantially faster rates. The ability to obtain orientation data even faster would therefore open up a wider range of problems where defocused fluorescence imaging could be used.

A way to possibly speed up the acquisition process and reduce the amount of background fluorescence was proposed. This involved focusing specifically on a single molecule using the microscope in manner closer to a confocal setup than one used for wide field illumination. In this setup, the confocal light path was used to focus the beam into a diffraction-limited spot on the surface of the sample. The EMCCD camera was first used to observe the position of the spot on a cleaned blank slide. After this a standard sample slide of DilC embedded in a PMMA layer was mounted on the microscope. TIRF illumination was then used to locate a fluorophore and move it within the diffraction limited spot. The 532 nm confocal laser was then used to illuminate the sample, the stage was defocused by 1 nm and the single defocused pattern recorded on the EMCCD camera. The images were then fed to the MATLAB pattern recognition routine to provide the orientation of the single recorded pattern

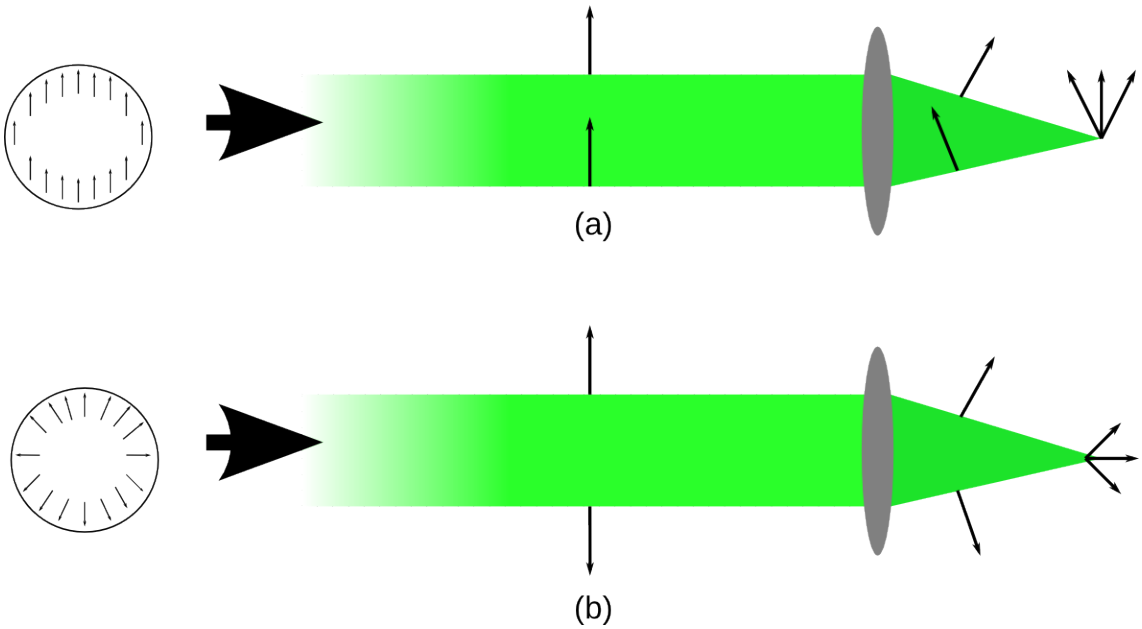

Figure 5.14.: A comparison of in-focus polarization between linearly (a) and radially (b) polarised laser beams

In order to ensure that the incoming focused beam would be capable of stimulating the DilC molecules regardless of their orientation, it was necessary to radially polarise the input laser beam. As can be seen in Figure 5.14, a linearly

polarised beam is only capable of stimulating molecules with absorption dipoles oriented parallel to its direction of polarisation and has had little, if any, z-axis polarisation. By contrast, the radially polarised beam allows for the stimulation of molecules with absorption dipoles oriented in any direction including along the z-axis.

The radially polarized beam was initially produced using a custom polarisation converter fashioned from four half-wave plates glued together. This was later replaced with a liquid crystal polarisation converter purchased from Arcoptics.

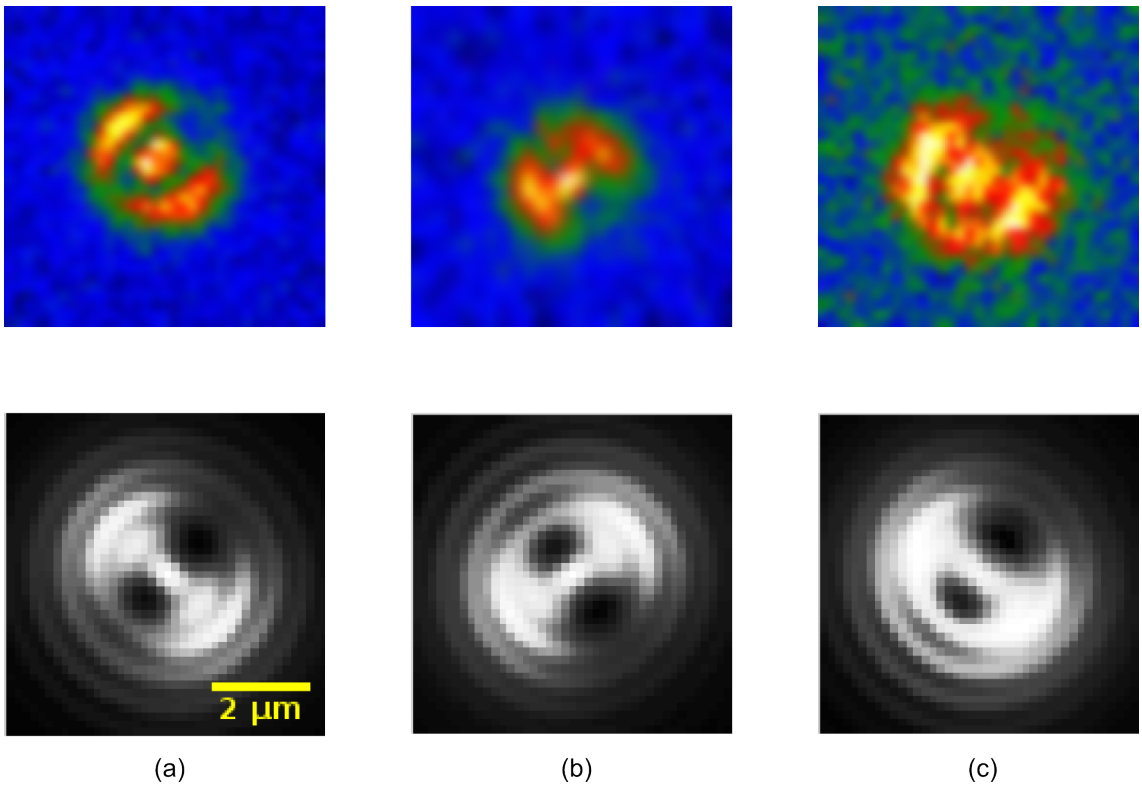

Figure 5.15.: Single defocused fluorescence images and their matching patterns Pattern (a) fits an orientation of θ =80°, ϕ = 130°, pattern (b) fits an orientation of θ =60°, ϕ =230° and pattern (c) fits an orientation of θ =70°, ϕ = 130°

Because only a single molecule was fluorescing and being imaged at a given time, there wasn't as much background fluorescence. This coupled with the substantially higher intensity produced by focusing the laser to a diffraction limited spot resulted in acquisition times on the order of 50 ms to 100 ms. Examples

of imaged patterns can be seen in Figure 5.15. Pattern (a) represents an orientation of θ =80°, ϕ =130° while pattern (b) θ =60°, ϕ =230° and pattern (c) is θ =70°, ϕ =130°.

This technique is of limited use in the long run, because while it allows for acquisition times to be reduced by half or better, it only allows for the measuring and tracking of a fluorophore within a space slightly larger than the diameter of a diffraction limited laser spot. The increased intensity of the laser beam also makes the molecules blink faster and bleach quicker, making it harder to track orientation changes over long periods of time. For fast measurements of a single molecule confined to a small space though, it does provide advantages.

5.4. Summary

The defocused orientation measurements of dye molecules embedded in PMMA and lipid thin films is the main focus of this chapter. Initially the well-researched sample of DilC molecules immobilised in a 10 nm PMMA thin film is utilised to enable us to determine the differences in orientation distribution that occur for linearly p-polarised and circularly polarised laser light used to illuminate a sample either normal to its surface or via TIRF illumination. The results are strongly suggest that TIRF illumination is slightly more effective than illumination normal to the surface in exciting molecules of arbitrary orientation. I also discuss the process of creating thin PMMA films and embedding dilute fluorophores in them. Finally, I attempt to quantify the minimum amount of time required on my microscope accumulate enough photons patterns that can be detected with low error values. The results seemed to indicate that integration time of greater than 0.5 s results in patterns with consistently low least-squares error values.

I then discuss the process of creating synthetic lipid (DPPC) thin films, inserting DilC molecules and then measuring the orientation of those dye molecules. While the general understanding of how DilC interacts with lipid layers should have resulted in a dye orientation with $\theta \approx 90°$, the experimental results showed a distribution with mean 41° and standard deviation 16°. The best explanation I

have for this, from similar experiments, is that the dye molecules were migrating outside the lipid bilayers.

A novel wide-field/confocal hybrid system was also proposed to probe the orientations of single molecules in the hopes that it would reduce the background noise and thus the acquisition time required for a single pattern. The technique appeared to work, but had the same disadvantage as single molecule polarisation techniques. Namely, the ability to only measure one molecule at a time and only if it remains within a diffraction limited spot.

Chapter 6.

Orientation Measurements On Densely Labelled Samples

6.1. Imaging A Densely Labelled Fluorophore Sample

Resolving the signals from fluorescent molecules closer to each other than the diffraction limit (≈250 nm diameter) when in focus is problematic. Similarly, determining the orientation of fluorescent molecules closer than the diameter of a defocused pattern (≈1 µm in diameter) can be an issue. If the patterns overlap significantly then the pattern recognition algorithm ceases to be able to resolve them. As a result any attempt to determine the orientation of individual fluorescent molecules can only be done on samples with extremely sparse distributions, which is not always practical.

A possible solution to this is proposed by Simonson[113] and involves the use of the blinking and bleaching characteristics of fluorescent molecules. Between those two characteristics, it can be expected that the absolute difference between any two successive frames will reveal the patterns left behind by molecules starting to fluoresce or blinking off in between the frames. For cases where the revealed patterns overlap, the pattern matching algorithm will usually be unable to produce a good fit, but for individual, isolated patterns, it will be possible to fit it and determine the orientation of that molecule. Experimentally, this is done by

continuously illuminating the entire sample with circularly polarised laser light as the fluorescent molecules bleach out over time until there are only enough visible patterns to allow pattern matching on the last frame. First fit the patterns in the last frame, then fit the patterns visible on the absolute difference between that frame and the previous frame, and then continue fitting the absolute difference between adjoining frames. The molecules that either blink or bleach between frames are left behind creating an image sparse enough for orientation estimation to be performed. While this technique will not capture the orientation of every single fluorophore in a dense sample, it will provide a lot of orientation information. Dedecker et.al. propose a very similar technique they term SPIDER microscopy.[26]

Due to the nature of the least squares fit routine, it also provides the coordinates of the central pixel in the pattern, which, depending on the magnification of the imaging objective, can also provide sub-diffraction limit estimation of the position of the molecule (160 nm in this experiment, 62 nm in later ones).

For in-focus molecules, fitting a 2D gaussian to the fluorescence pattern can be used to provide the location of a fluorophore to sub-10 nm precision. In theory, it might be possible to achieve the same result by first obtaining the orientation of the fluorophore via pattern matching, then fitting the 2D function associated with that orientation over the experimentally obtained pattern. This is a more difficult proposal than it appears at first thought, for reasons best illustrated by Figure 3.4. Depending on the defocus distance and orientation of the particle, its 2D function can appear quite different. This means that, unlike a 2D gaussian fit where the standard error provides an estimate of position, there is no intuitively obvious way to determine the area at the centre of the fit that represents a good estimate for the position of the fluorophore. There may exist solutions to this problem, but for my purposes the ability to estimate position to less than the diffraction limit while obtaining orientation data was good enough.

6.1.1. Imaging Dense Fluorophores in PMMA

The first step in validating this technique involved applying it to a standard sample of dye-embedded PMMA. Except, in this case, the concentration of Dil embedded in the PMMA layer was high enough for the single molecule patterns to overlap (1×10^{-9} mol). A sample consisting of a glass cover slip with fluorescent molecules embedded in a clear polymer spin coated on its surface. The surface was brought into focus, then slightly defocused by moving the sample towards the objective by 600 nm. Defocused images were then acquired by the cooled EMCCD camera placed in the image plane.

Data was then taken continuously at a rate of 5 s per frame for sets of 120 frames at a time. If there was still detectable fluorescence after the first set of data then another set of data was taken until there were just enough fluorophores left to allow for orientation estimation. Starting from the last frame, a MATLAB routine was used to work backwards from the last frame taking the absolute difference between frame n and frame n-1. Each of the difference frames was then passed on to the pattern recognition routine to provide the position and orientation of the visible fluorescent patterns. A graphical illustration of the process can be seen in Figure 6.1 and shows the process of extracting individual defocused patterns from a densely labelled sample.

By analysing each frame, it is possible to end up with position and orientation information for a substantial number of the molecules in the field of view, even those that overlap. The location of the centre of each pattern also allows for the position estimation of each fluorescing molecules to within the width of a single pixel.

A reasonable concern would be whether the patterns that are left behind between frames actually represent the fluorescence patterns produced by a single molecule or could be the result of overlapping patterns produced by multiple molecules switching on and off in the same area, especially with such long integration times. The pattern matching algorithm appears to be unable to match a pattern produced by two overlapping fluorophores of similar intensity unless

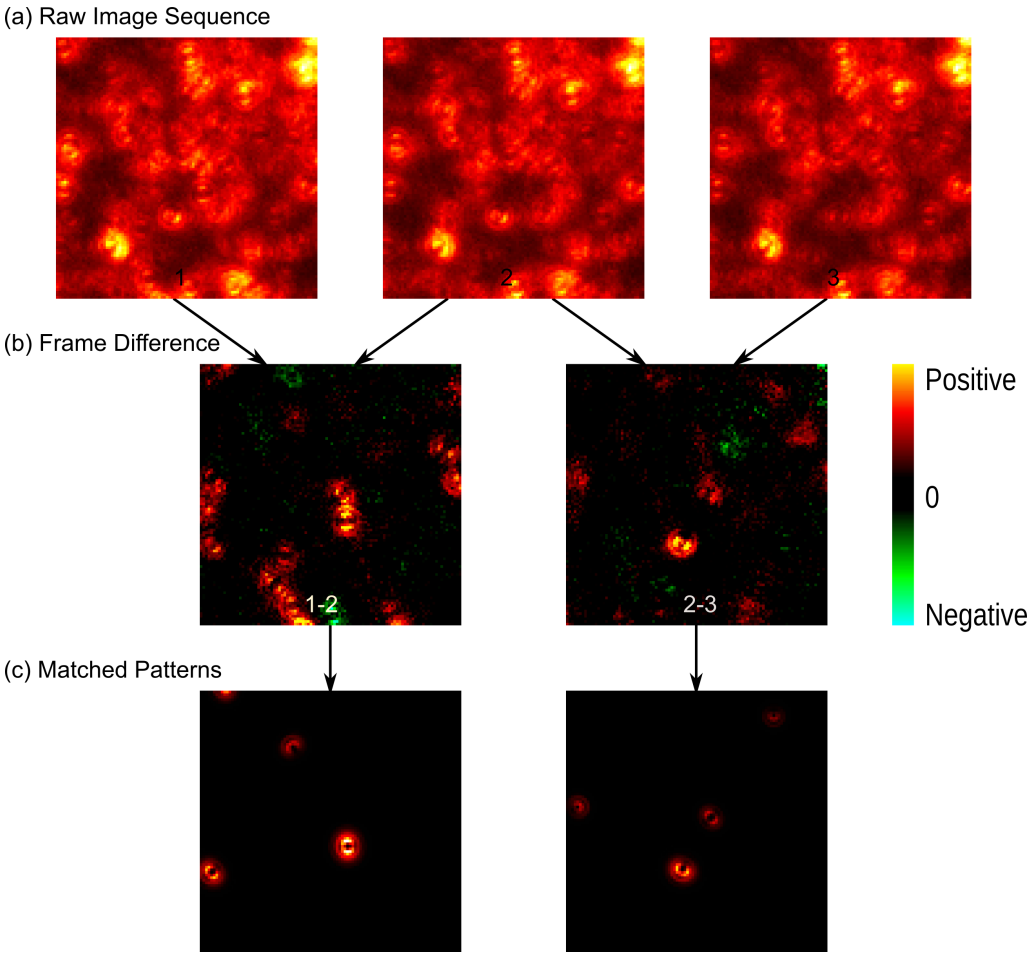

Figure 6.1.: A graphical illustration of the process of retrieving data from densely labelled PMMA samples. The difference between two adjacent frames shows patterns that disappear (in red) and ones that appear (in green). By applying the pattern matching algorithm to the difference frames, we can recover the orientation data for the blinking fluorophores

they are both centred in the same pixel and oriented in the same direction, which prevents this from becoming a major issue.

6.2. Densely Labelled Lipid Gratings

An extension of the orientation imaging on lipids involved imaging fluorescent molecules embedded in nanoscale synthetic lipid bilayer structures. These structures were produced by Dr. Michael Hirtz of the Karlsruhe Nano Micro Facility (KNMF), a division of the Karlsruhe Institute of Technology(KIT) using a technique known as dip-pen nanolithography (DPN).[114–116]

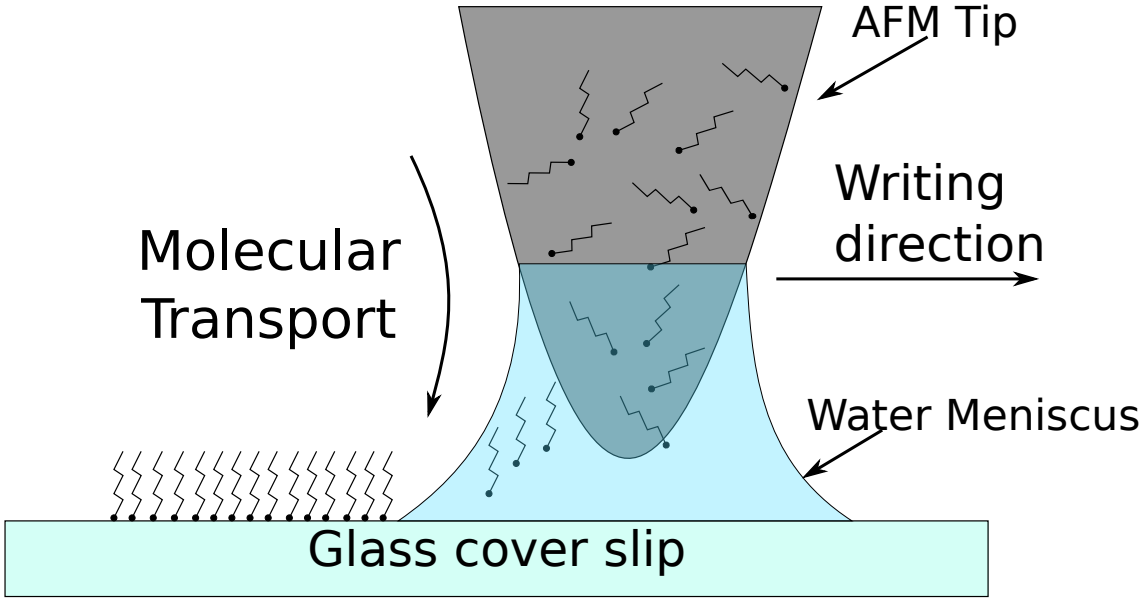

Figure 6.2.: Dip-Pen Nanolithography

DPN is a process that uses an AFM tip as the equivalent of a quill pen. In place of ink, the tip is dipped in a solution of lipid molecules suspended in water. By bringing the tip in close proximity to a hydrophilic surface, a meniscus is formed between the tip and the surface as shown in Figure 6.2. Capillary action then causes the lipid molecules to be transferred to the surface where they self-organise. The water then dries leaving behind a lipid layer on the surface. The AFM tip can therefore be directed to draw any structure on the surface. Additionally, controlling the humidity during the patterning process has been shown to affect the thickness of the lipid structure left behind. This allows for the creation of structures that average a single bilayer in thickness to ones that are several bilayers thick. For the purposes of these experiments, single bilayer structures were very

much preferred. The lipids used for our nanostructures were made of DOPC (1,2-Dioleoyl-sn-glycero-3-phosphocholine). By adding small amounts of dye to the DOPC solution it is possible to make lipid patterns with dye molecules embedded in them. For this experiment, the dye used was R6G (Rhodamine-6G, ethyl 2-[(6Z)-3-ethylamino-6-ethylimino-2,7-dimethyl-xanthen-9-yl]benzoate hydrochloride) functionalized DPPE (1,2- dipalmitoyl-sn-glycero-3-phosphoethanolamine).

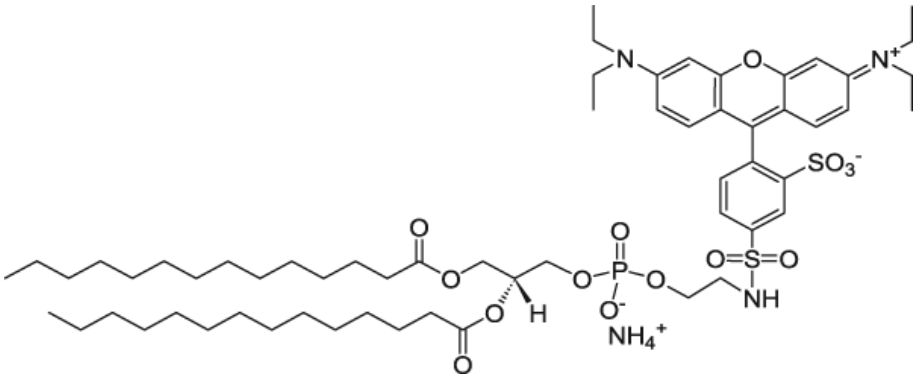

Figure 6.3.: R6G-functionalized DPPE molecular structure

Two kinds of samples were produced. The first set of samples can be seen in Figure 6.4. They consisted of gratings formed by laying down parallel lipid lines on a glass slide. Each slide had gratings with pitch spacings of 0.25 µm, 0.5 µm and 1 µm and included 1% R6G functionalized DPPE. The gratings were placed on the microscope with the lines oriented along the $\phi = 90°$ and 270° line.

Data was taken from multiple gratings on the same slide in order to obtain as much orientation information from as many Rhodamine-PE molecules as possible to determine the angular distribution of fluorescent molecules in the lipid bilayers. The results from the lipid gratings can be seen in Figure 6.5.

From these results it can be seen that the Rhodamine molecules embedded in the gratings appear to display preferences in both a polar and azimuthal orientation. The polar orientation appears to have a tightly constrained distribution with a mean value of 33° a standard deviation of 10°. A search through the literature found a reasonably comparable molecular modelling prediction on the orientation of R6G functionalized DPPE in a DPPC bilayer.[117] It also showed the

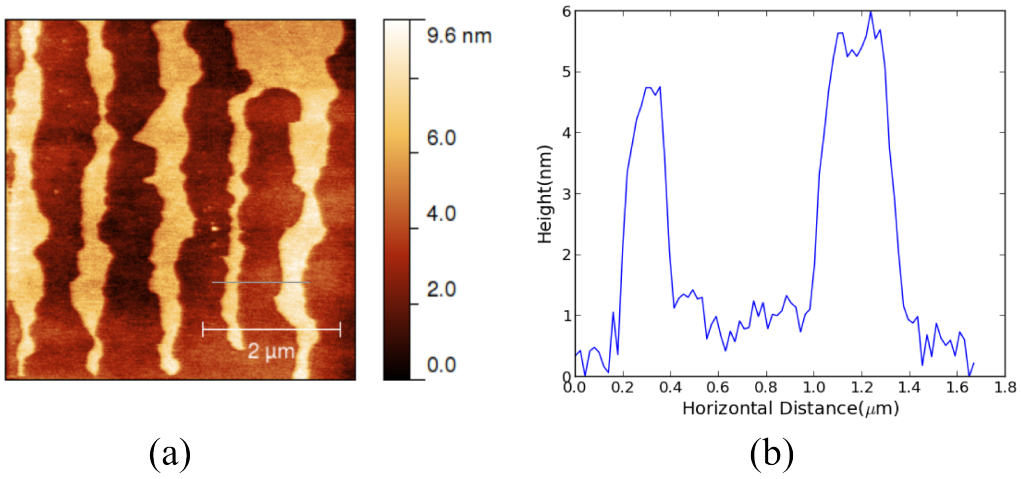

Figure 6.4.: An AFM scan (a) and height profile (b) of a lipid grating. The height profile is of the grey line on the AFM image.

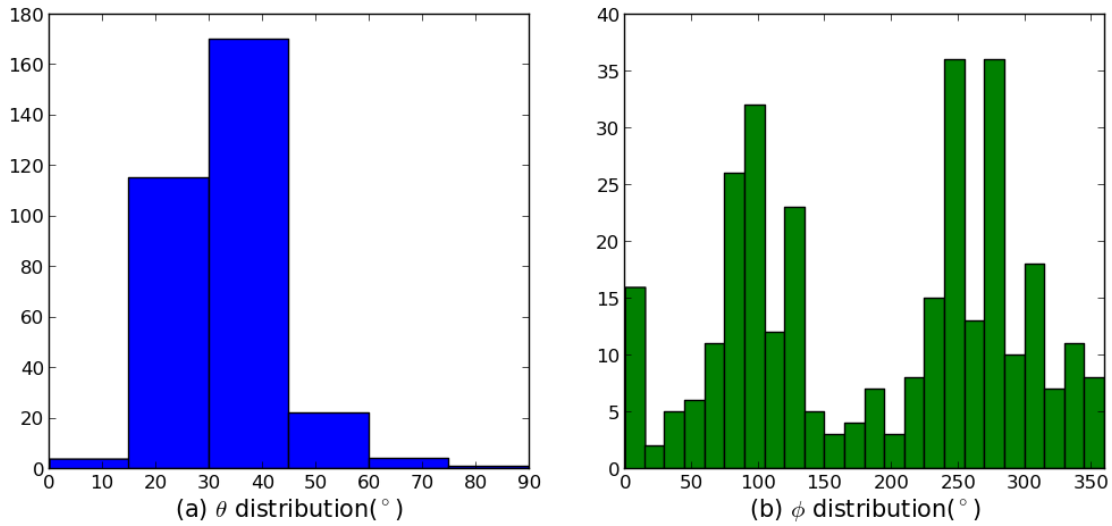

Figure 6.5.: θ and ϕ orientation distributions of Rho-PE functionalized lipid molecules embedded in DOPC gratings

R6G molecules were constrained in polar orientation to a mean of 44° standard deviation of 8° (image in Figure 6.6). The distribution of fluorescent molecule orientations from our experiment and the error bars from the simulations appear to overlap.

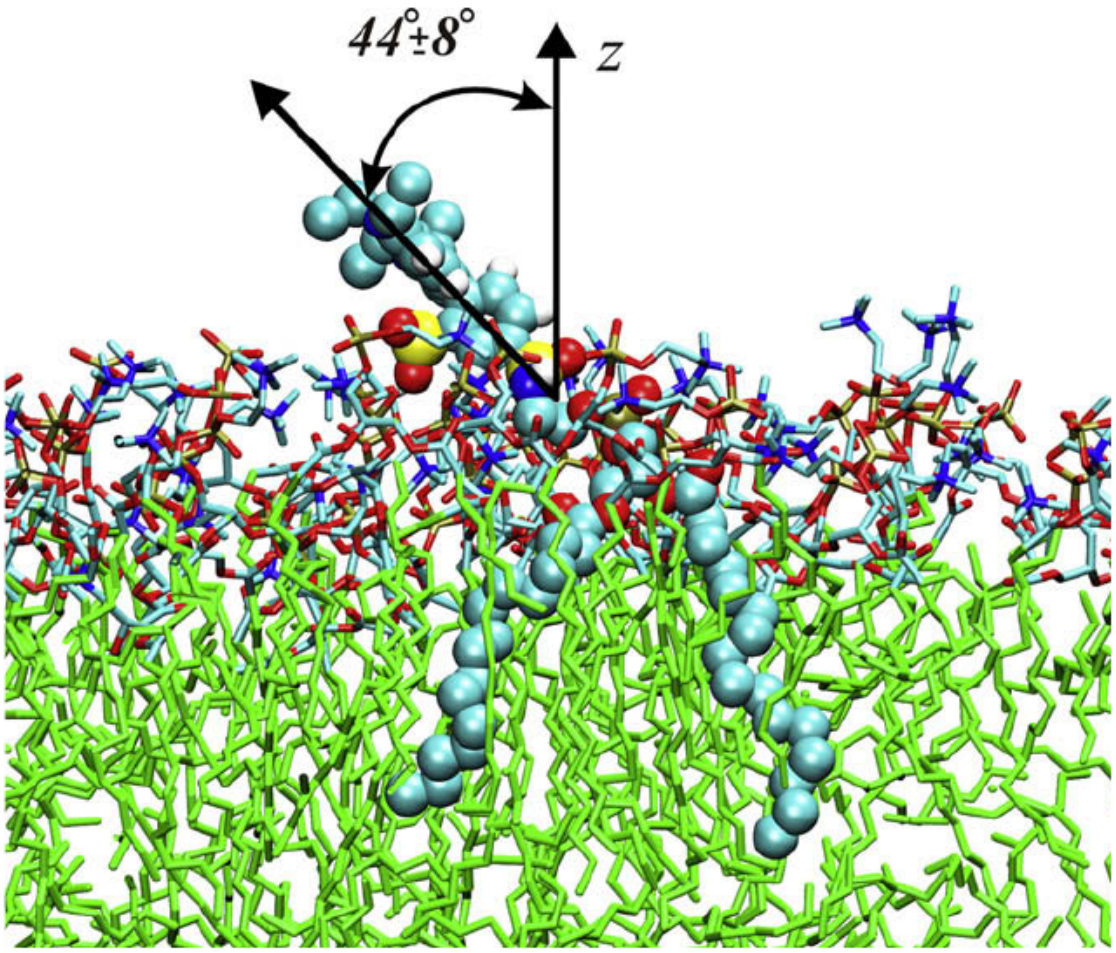

Figure 6.6.: Molecular dynamics simulation of R6G-labelled DPPE in a DPPC bilayer showing the predicted orientation of the molecule[117]

A more unexpected result showed up in the distribution of the azimuthal orientations of the detected fluorophores. As can be seen from Figure 6.5, the gratings were oriented vertically in our field of view. The azimuthal orientations of the detected fluorophores ended up clustered around 2 peaks. Fitting a double Gaussian to the data gave us one peak with a mean of 88° and a standard deviation of 41° and another with a mean of 270° standard deviation of 41°, which corresponded to molecules aligned parallel to the lines. This would seem to imply strongly that the Rhodamine molecules are oriented in the same direction as the lines. The thin film orientation measurements in Chapter 5, however, mean that this could simply be

an artefact of an elliptically polarised beam. In order to be sure that these results were not purely a result of the illumination polarisation being uneven, a new set of DPN structures were fabricated by Michael Hirtz at KNMF.

The new samples were of star shaped structures constructed with lipid bilayer spokes roughly 45° apart (Fluorescence and AFM images as well as a line profile shown in Figure 6.7). Like the lipid gratings, they were produced using an AFM tip dipped in DOPC solution to individually write each star on the surface of the cover slip. Again, they included 1% - 5% Rhodamine functionalized DPPE. Defocused imaging was performed in the same way as the lipid gratings.

These samples were made to follow up on the possibility that the preferential azimuthal orientation of the fluorophores seen with the gratings. After they were imaged, molecules centred around the straight lines were isolated from the results and their orientations examined. The results can be seen on Figure 6.8. The vertical sections of the star are labelled blue, the horizontal parts in green and the diagonal sections in red and yellow.

Initially, the results from each individual spoke were examined separately. However both spokes in the same direction had the same orientation distribution, so it made more sense to combine the results from opposite spokes. Those results can be seen in Figure 6.9. For the single molecule distributions in the vertically and diagonally oriented spokes, they tended to be clustered around two peaks roughly 180° apart. A double Gaussian was then fitted to each distribution. It is likely that the reason the distribution for the horizontally aligned spokes couldn't be clear is because of the preferential illumination seen in Chapter 5.

Results were obtained for the vertical lines labelled (a) (mean 88° with standard deviation 24° and mean 266° with standard deviation 31°), the red diagonal lines labelled (b) (mean 69° with standard deviation 38° and mean 250° with standard deviation 28°), and the yellow diagonal lines labelled (d) (mean 102° with standard deviation 40° and mean 281° and standard deviation 34°).

The results seem to imply that the orientation of the R6G-DPPE lipids are arranged in line with the direction in which they are written. The messiness of the

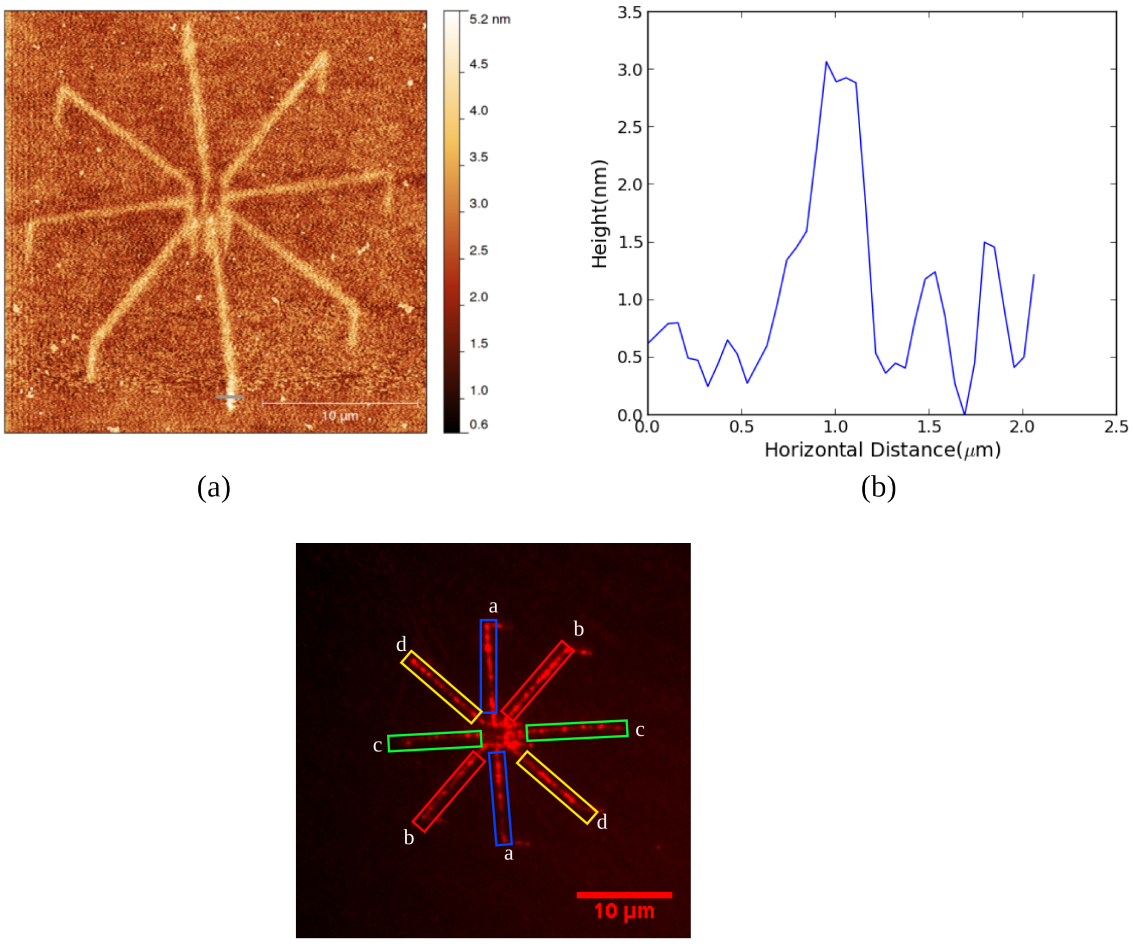

Figure 6.7.: AFM image and height profile (a) and (b) as well as fluorescence image (c) of star shaped lipid nanostructures. The coloured and labelled boxes represent the sections of the structure where data was taken. The line profile was taken from the grey line on the AFM

data on for the horizontally oriented lines would make sense if we assumed the fluorophores were arranged along the line of the lipid structure and the excitation beam was eliptically polarized along the vertical axis. If the fluorescent molecules were randomly arranged and the orientation effects showing in the data were purely a result of the orientation of the excitation beam, the horizontal line data would also show a vertical orientation distribution. The horizontal data is instead almost flat with a minimum at $\phi \approx 150°$, which could be explained by assuming

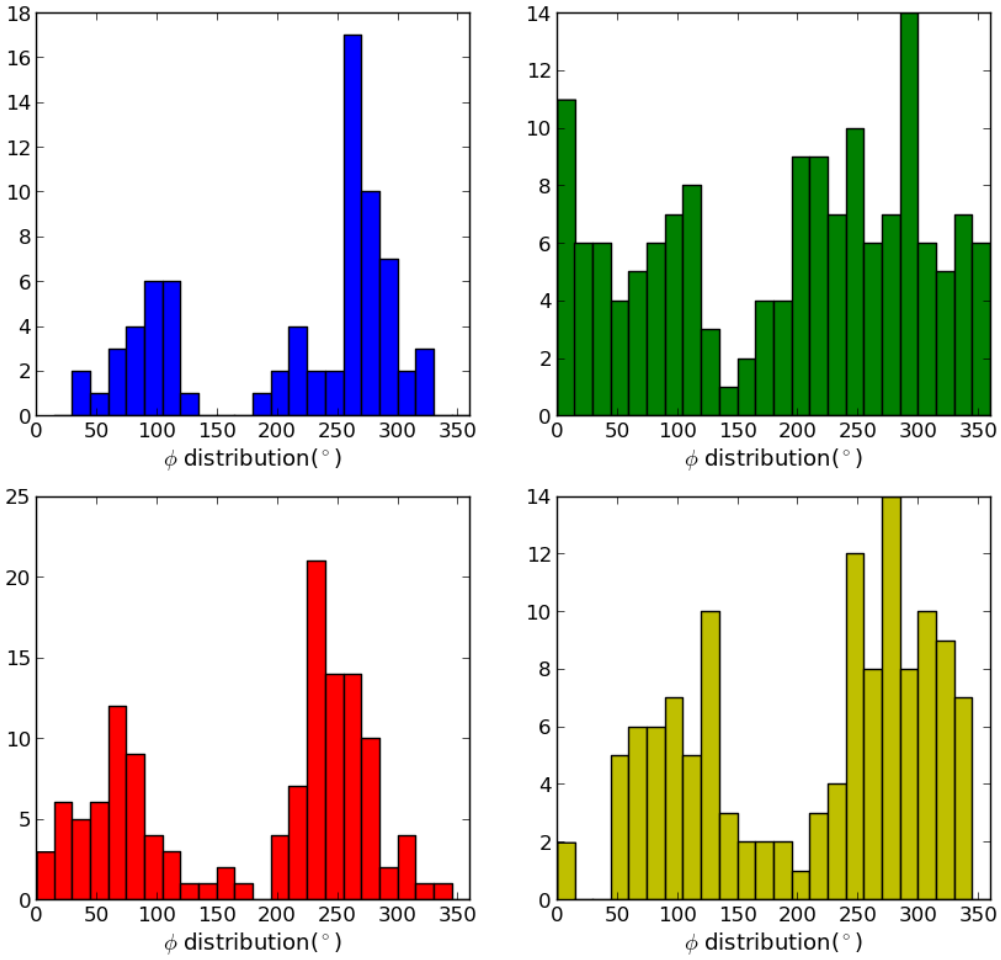

Figure 6.8.: ϕ orientation distribution of the R6G-functionalized DPPE molecules embedded in a star shaped lipid nanostructure. The graphs are labelled such that the vertical sections of the star are labelled blue, the horizontal parts in green and the opposing diagonal sections are in red and yellow

that the horizontally oriented fluorophores are barely excited by the incident laser and all that can be seen is the smaller population of diagonally and vertically oriented fluorophores.

In order to confirm the hypothesis about the orientation of fluorescent molecules in DPN nanostructures, it would be useful to also perform fluorescence anisotropy imaging of the star shaped structures to show if they also indicate differing average dye orientations for each spoke.

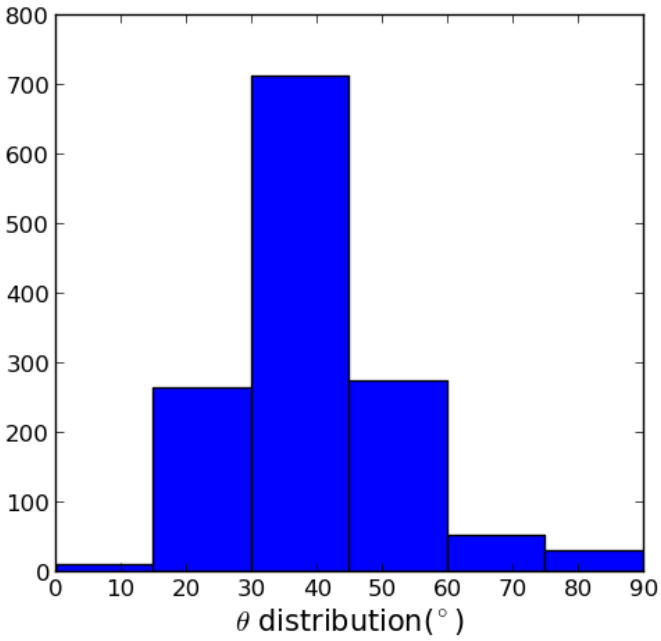

Figure 6.9.: θ orientation distribution of Rhodamine-functionalized DPPE molecules embedded in a star shaped lipid nanostructure.

6.3. Summary

In this chapter, I propose the adaptation of existing fluorescence techniques that make use of the blinking and bleaching characteristics of dye molecules to isolate fluorescence patterns in densely labelled samples. The first step is the confirmation of this technique by applying it to a test sample of relatively high concentrations of DilC dye embedded in PMMA thin films.

After proving that the technique works on polymer thin films, it was then applied to lipid nanostructures produced by dip-pen lithography and containing reasonably small concentrations of of Rhodamine-labelled DPPE. The results of imaging these nanostructures appears to suggest both that the dye-labelled lipid molecules self-assemble in line with the direction of its writing by DPN and that the polar orientation of the dye molecules (mean 33° with standard deviation

10°) match up fairly closely to the predicted polar orientation distribution of dye molecules found by molecular dynamics simulations ($44° \pm 8°$).

These experiments are reasonably good as proof of concept that the technique actually works and can therefore allow us to expand the use of defocused fluorescence imaging to determine the superresolution position and the orientation samples that are not extremely sparsely labelled, thus possibly opening up the classes of problems defocused imaging can be applied to.

Chapter 7.

Exploring Superresolution Position Estimation

7.1. Superresolution Position Estimation

As was mentioned in Chapter 1, the MATLAB pattern matching algorithm attempts to locate the central pixel of the pattern in addition to the 3-D orientation it represents. This implies that the technique can provide the location of the fluorophore within the area represented by a single pixel.

Since the area represented by a pixel in the image is usually substantially smaller than the diffraction limit, this would imply that the defocused fluorescence estimation technique should provide superresolution position estimation in addition to orientation estimation. This does not appear to have been explicitly tested though. The study of the limits of the technique in Chapter 3 implies that, given enough collected photons, the patterns can be located to within the area of the central pixel (160 nm x 160 nm). Some proof that this works can be seen in the position information obtained from the Rhodamine molecules embedded in the lipid nanostructures discussed in Chapter 6. As can be seen in Figure 7.1, the molecular positions all fell within the area occupied by the nanostructures, which were all about 500 nm to 700 nm thick.

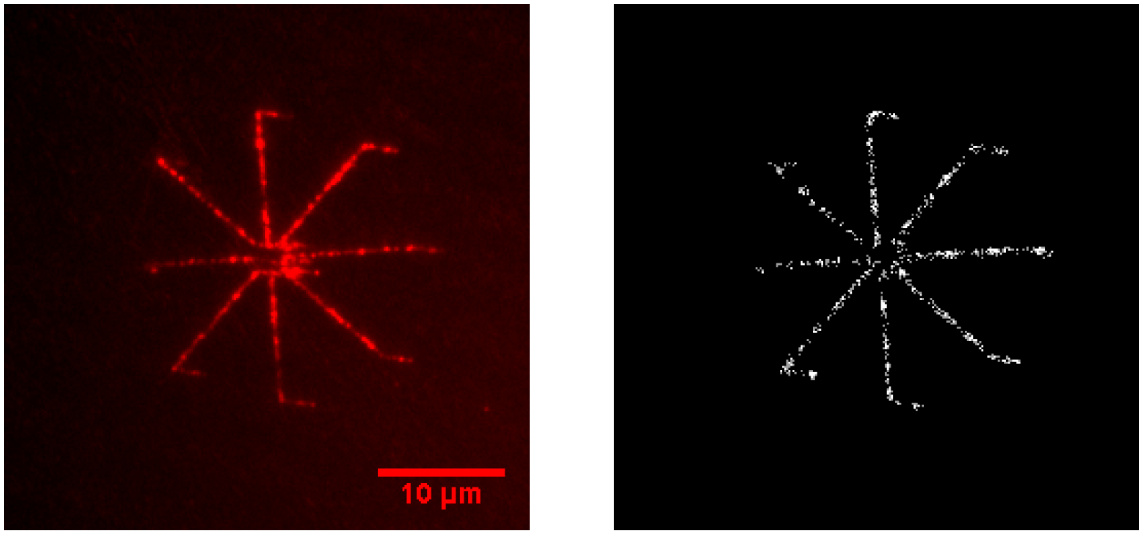

(a) Fluorescence Image (b) Position Information

Figure 7.1.: Fluorescence image and processed location data from star shaped lipid structures. Each dot epresents the location of a single fluorescent molecule isolated to within a 160 nm x 160 nm pixel.

7.2. Confirming Superresolution Position Estimation

In order to further confirm the position estimation works as expected, a new kind of sample was needed. The idea behind the new sample was to produce a system in which one or more fluorescent molecules could be reliably isolated in a space smaller than the size of a single pixel.

7.2.1. Sample Creation

To make an isolated test sample, the first step was to obtain polystyrene nanoparticles capped with PEG and functionalized with Rhodamine-6G molecules. These were obtained from the Biotechnology group at NPL. The particles were ≈ 60 nm in diameter and obtained in aqueous suspension.

Fixing the particles to the slides was achieved by mixing the nanoparticle suspension with a 1% solution of Polyvinyl Alcohol (PVA, 13,000Mw to 23,000Mw,

Sigma Aldritch) in water. The diluted solution was then spun on a cleaned glass slide at 2000RPM for 5 minutes. The choice of PVA was made because of its solubility in water and the fact that it shares a similar refractive index with polystyrene. Because polystyrene dissolves in most organic solvents, the polymer of choice could not be one that required an organic solvent. The closeness in refractive indices between PVA and polystyrene mean that the thin film with the beads embedded can be treated as a uniform layer. These two characteristics made PVA a perfect choice.

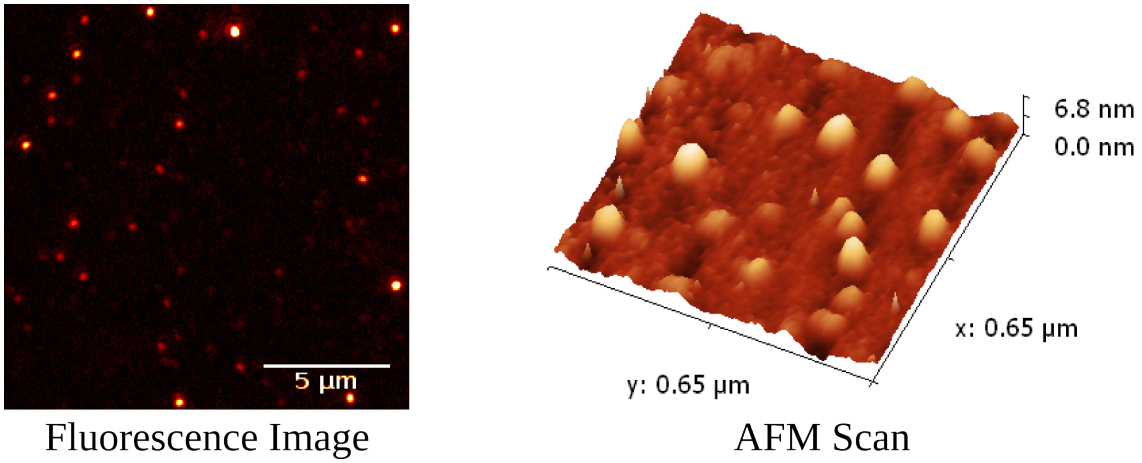

Figure 7.2.: AFM scan and fluorescence image of nanoparticle sample

The resulting sample had a 50 nm thick PVA layer with polystyrene beads embedded in it. This served to both hold the beads in place and keep the attached molecules from changing orientation while they were being imaged. An AFM scan and a fluorescence image of a representative sample can be seen in Figure 7.2. Since each nanoparticle had a diameter of 60 nm, the resolution of the camera was improved by fitting a 2.5x beam expander from Nikon on the side port of the microscope and coupling it to the EMCCD camera. The addition of the beam expander changed the size of the pixel from 160 nm x 160 nm to 64 nm x 64 nm.

7.2.2. Sample Imaging

The magnified camera was then tested by placing a standard test sample of Dil molecules distributed in a 10 nm PMMA layer on the microscope, illuminating it with circularly polarized 532 nm laser light, filtering the fluorescence and then focusing it it through the beam expander on the cooled EMCCD camera. Images were then captured with 2 seconds of integration time and introduced to the MATLAB routine with all the same parameters as were used in Chapter 5 except for a pixel size of 64 nm and a larger corresponding number of pixels for pattern matching. The results can be seen in Figure 7.3 and it shows fairly clearly that the beam expander still works as expected.

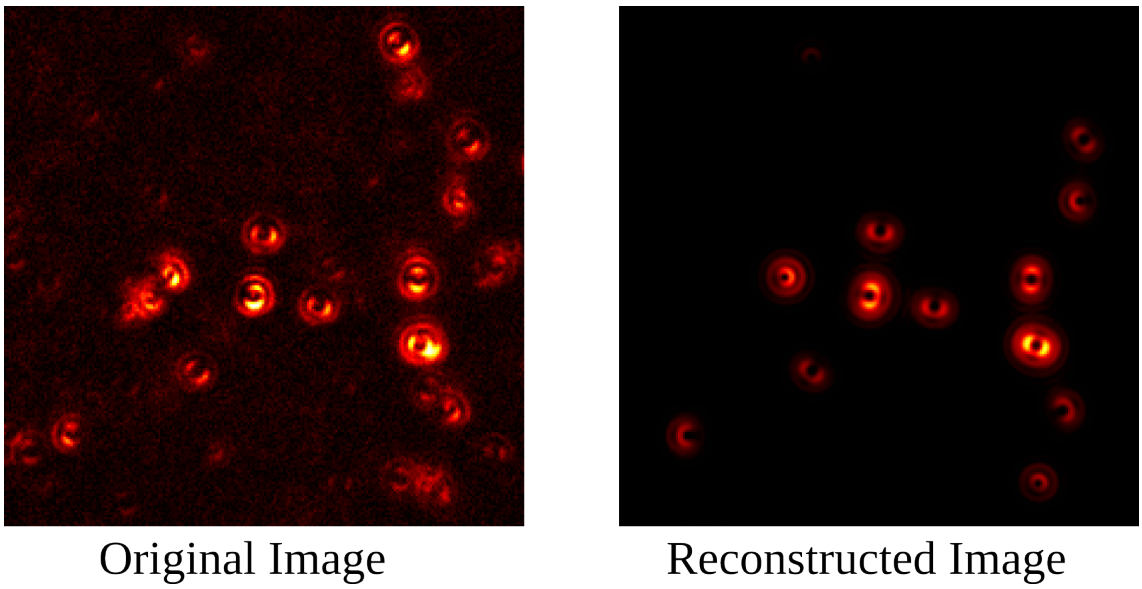

Figure 7.3.: Magnified defocused fluorescence image and its reconstruction from matched patterns

Once it was confirmed that the expander worked as expected, The nanoparticle sample was then mounted on the inverted microscope, and illuminated with circularly polarized 532 nm laser light normal to the sample from the attached TIRF module. The PI stage was then defocused by 500 nm. The fluorescence was filtered, magnified by 2.5x via the image expander, and then focused on the EMCCD camera. An image was recorded every second until all fluorescence

activity stopped. The same procedure was repeated at several points on the surface of several samples.

The images were then imported into MATLAB and an image showing the difference between adjoining frames was calculated and then fed to the pattern recognition algorithm using the same process used in Chapter 6. This time, the layer was assumed to be 60 nm thick, the defocus distance was set to 500 nm and the refractive index to 1.55. The pixel size was kept at 64 nm.

7.2.3. Results

Visual inspection of the fluorescence images showed some interesting behaviour. The functionalization process produced nanoparticles with a range of Rhodamine molecules attached to them. Some of the nanoparticles appeared to have no attached fluorophores, the majority of them appeared to only have one fluorophore attached since only one distinct pattern could be observed. A few of them appeared to have more than one attached fluorescent molecule, implied by multiple patterns that were superimposed over the same central spot and individually blinked on and off before bleaching out. For the cases of more than one fluorophore, fluorescence behaviour of the Rodamine molecules attached to the nanoparticles was very different from the way they behave as single molecules embedded in polymer. There were long dark periods and periods of switching between different molecules attached to the same nanoparticle.

An explanation of the strange fluorescence lifetime behaviour of Rhodamine molecules can be provided by the fact that Rhodamine in high concentrations ($> 1 \times 10^{-3}$ mol) changes fluorescence lifetime behaviour. One possible explanation for the lifetime changes is that Rhodamine molecules form dimers and the process of dimerization leads to the formation of new triplet states that make nonradiative decay more probable and thus change the fluorescence lifetime.[118]

In addition to the unusual blinking and quenching behaviour of the fluorophores, enough information was also observed to provide superresolution position data. The results can be seen in Figures 7.4 and 7.5. In both figures, the

difference images were used to show both the disappearing (red component) and reappearing (green component) parts of the image.

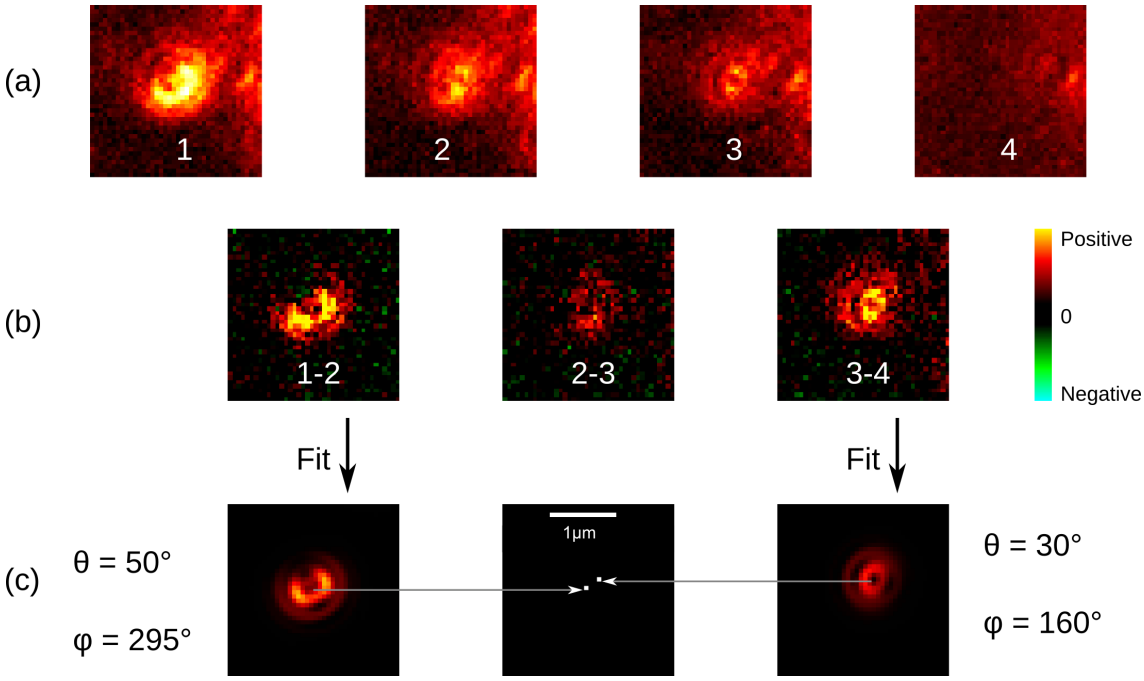

Figure 7.4.: Resolution of the overlapping patterns produced by two functionalized nanoparticles each isolated to a 64 nm x 64 nm square and separated by 230 nm. The image sequence in (a) is the original data obtained from the camera, (b) shows the data obtained by taking the difference between two adjacent frames with dissapearing patterns in read and appearing ones in green. Fitting the patterns in the difference images results in the position and orientation data visible in (c)

Figure 7.4 shows the how the progressive bleaching of the sample allowed the detection of overlapping patterns from 2 fluorescent molecules closer together than the diffraction limit and the two individual patterns. The two patterns had orientations of θ =30°, ϕ =160° and θ =50°, ϕ =295° and were each isolated in a 64 nm x 64 nm space, 230 nm apart. For both θ and ϕ, the error The most obvious interpretation would be that the patterns are from molecules attached to different nanoparticles. Since the two nanoparticles were closer together than the diameter of a diffraction limited spot, this is a strong indication that the technique can be used to resolve two patterns at superresolution accuracy.

Likewise, Figure 7.5 shows the changes in patterns created by the switching behaviour as a result of the superimposition of two distinct patterns representing different orientations(θ =85°, ϕ =195° and θ =55°, ϕ =256°) but centred on the same pixel. In this case, the best interpretation is that the two molecules are both attached to the same nanoparticle. This shows that the technique works well enough that two molecules closer together than the space occupied than a single pixel will both be centred on the same pixel when they are imaged.

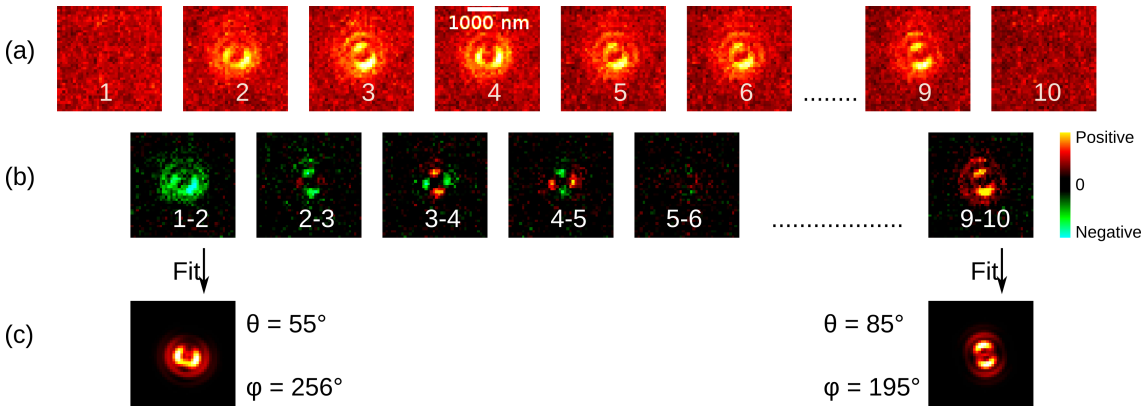

Figure 7.5.: The defocused pattern produced by two fluorescent molecules attached to the same 60 nm nanoparticle, resolved by finding the difference between the first and second patterns. Again, the image sequence as obtained from the camera is shown in (a), (b) shows the data obtained by taking the difference between two adjacent frames with dissapearing patterns in red and appearing ones in green. Fitting the patterns in the difference images results in the position and orientation data visible in (c)

7.3. Summary

First, we produced fluorescent samples at roughly about the same size as the effective pixel size of the CCD (≈60 nm) camera by functionalizing polystyrene nanoparticles with Rhodamine-6G molecules. By performing defocused imaging pattern matching on the difference images, we have shown that the process of locating the central pixel of a defocused pattern can be reliably used to isolate the position of a fluorophore to the area represented by the effective size of the pixel.

This technique therefore confirms that defocused fluorescence imaging is useful both for directly measuring the orientation of a fluorophore and providing superresolution position estimation.

Chapter 8.

Orientation Measurements On Dyes In Cell Membranes

Prior to this section, defocused orientation imaging has been primarily applied applied to fluorophores embedded in thin polymer films or artificial lipid bilayers. There exists no reason, however, not to apply the same technique to more complex systems. In this case, the technique is being applied to lipophilic dyes embedded in cell membranes.

DilC_{18}(3) is a commercial lipophyllic fluorophore that binds itself to the lipid layers, is used extensively for cell imaging and has been shown in both molecular dynamics simulations[111,112] and bulk cell measurements[51,119] to orient itself with its emission dipole parallel or close to parallel with lipid bilayers when introduced into them.

Generally defocused wide field orientation imaging is achieved using epifluorescence microscopy. For looking at molecules in thin films this works well since all the fluorophores are effectively in one plane. With cells though, illuminating the entire cell leads to a situation where the attempt to defocus the plane of interest merely leads to focusing on fluorophores in a plane $\approx$1 µm higher in the cell. Since the illumination produced by the in-focus fluorophores is greater than the illumination produced by the out-of-focus fluorophores whose patterns are

required for the technique, it makes the location of those patterns impossible to determine.

The solution is to illuminate the bottom of the cell membrane by use of Total Internal Reflection Microscopy (TIRF). Because TIRF relies on an evanescent field that extends ≈100 nm above the glass/glycerol interface the fluorophores stimulated are all in the lower cell membrane. Defocusing the image does therefore not result in focusing on stimulated fluorophores in a different plane of the cell.

The importance of this measurement lies both in the fact that it provides proof that defocused wide field orientation measurements can be performed using TIRF illumination and it is possible to follow image the orientation of fluorophores in the cell membrane and thus follow any processes to which they are attached.

8.1. Defocused TIRF on Cells

For the purposes of measuring molecular orientation in cell membranes, the cells used were MG-63 bone cancer cells (Abcam) obtained from Nilofar Farqui of the the biotechnology division of the National Physical Laboratory. She thawed out cells frozen in liquid nitrogen and then seeded them with low density on a petri dish with a 10 mm diameter 0.17 mm thick cover slip dimple in its centre. The cover slip centre was necessary because the small working distance of the high NA objective prevent the cells from being imaged through a standard petri dish.

After being seeded, the cells were left to incubate for 12 hours in order to attach themselves fully to the glass surface. After a phase contrast microscope was used to confirm that the cells were properly attached to the surface, Nilofar fixed the cells using 4% paraformaldehyde solution. This was done to prevent biological processes in the cell from moving around the fluorphore in its membrane faster than it would be possible to image them. The fixed cells were then passed on to me for further preparation and imaging.

The cells were covered in DI water and 40 µl of 1×10^{-8} mol in ethanol was added to the petri dish. The dish was then left to sit for an hour in order to allow

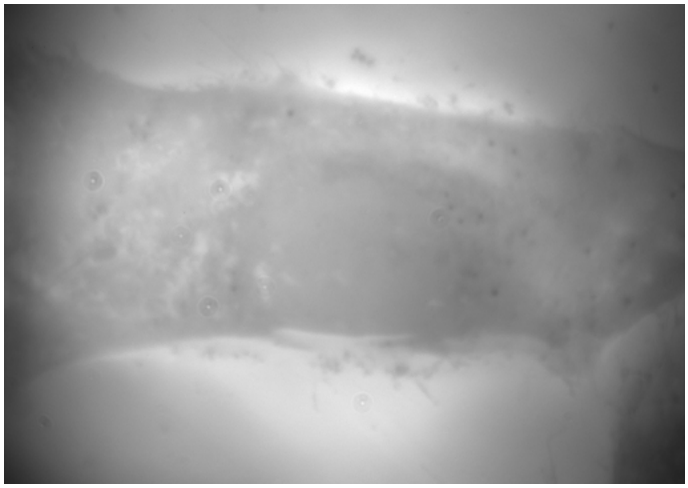

Figure 8.1.: White light epifluorescence image of a cell attached to the surface of a petri dish

the fluorophores to diffuse into the cell membrane. After an hour the petri dish was washed repeatedly about 6 times with DI water to remove the fluorophores not in the cell membrane. The dimple in the petri dish was then filled with glycerol, a clean cover slip was placed over it and the sides were sealed with clear nail varnish to keep oxygen away from the cells and allow the fluorophores to last for as long as possible. The petri dish was fixed on the PI stage above the microscope. Prior to beginning fluorescence imaging, the white light LED source was used to provide epifluorescence images of the bottom of the petri dish. The stage was then manually moved around to locate a cell and place it as close as possible to the centre of the image.

The cell was then illuminated via the circularly polarized 532 nm laser fibre coupled into the Nikon objective TIRF module. The fibre position in the module was adjusted to focus the beam along one side of the back aperture of the objective, causing the beam to then arrive at the bottom of the petri dish at the critical angle to allow total internal reflection at the glass/glycerol interface. This resulted in an evanescent field extending $\approx$100 nm into the sample to stimulate the fluorophores in the bottom membrane of the cells. As usual the surface of the sample was first brought into perfect focus and then the stage was displaced towards the objective by $\approx$600 nm.

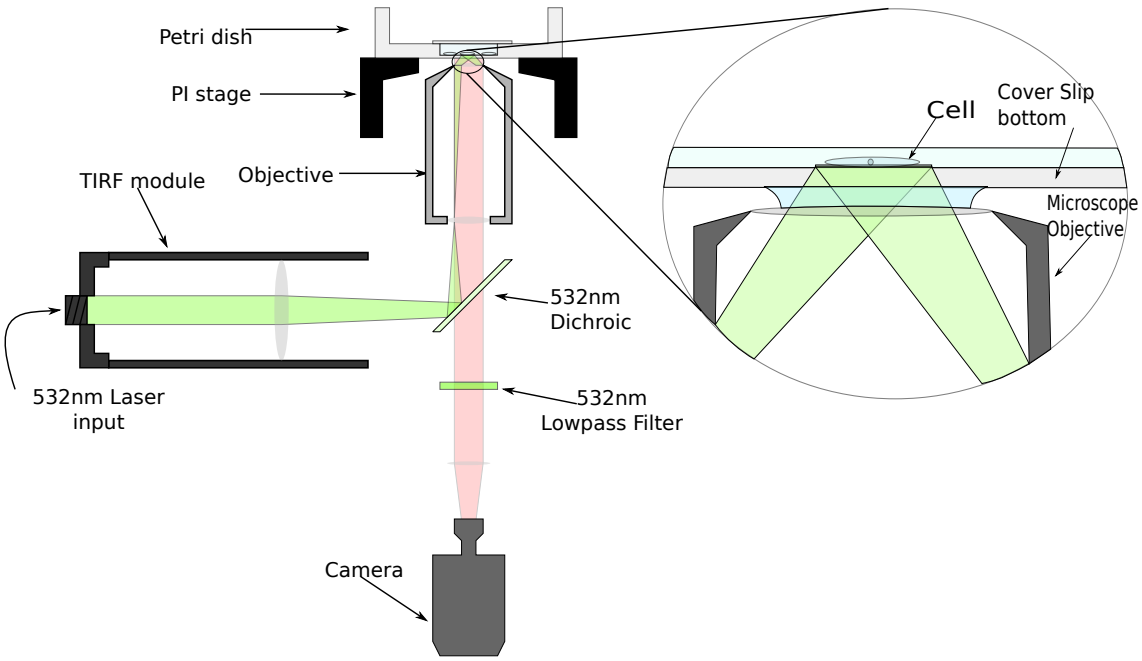

Figure 8.2.: Instrumental setup for cell TIRF

Data was then taken continuously at a rate of 1 s per frame for a set of 60 frames at a time. The set of 60 frames was then imported into the ImageJ™ software package and the standard deviation of the sequence was taken, revealing the fluorescence pattern of the blinking/bleaching molecules while filtering out the fairly constant autofluorescence from the cell membrane. Each of the processed images was then passed on to the MATLAB pattern recognition routine to provide the position and orientation of the visible fluorophores. This process was repeated for multiple cells on each of the petri dishes in order to obtain enough data to arrive at a reasonable value for the angular distribution of DilC$_{18}$(3) molecules in a cell membrane.

8.1.1. Results

By imaging the membranes of 6 different fixed cells attached to the bottom of the petri dish with individual dye molecules embedded in them, I ended up with the orientations of several fluorophores. As can be seen in Figure 8.3, the resulting

mean polar angle came to $\theta = 58°$ with a standard deviation of 31°). There did not appear to be any strong azimuthal preference when looking at the data for individual cells or when combining them.

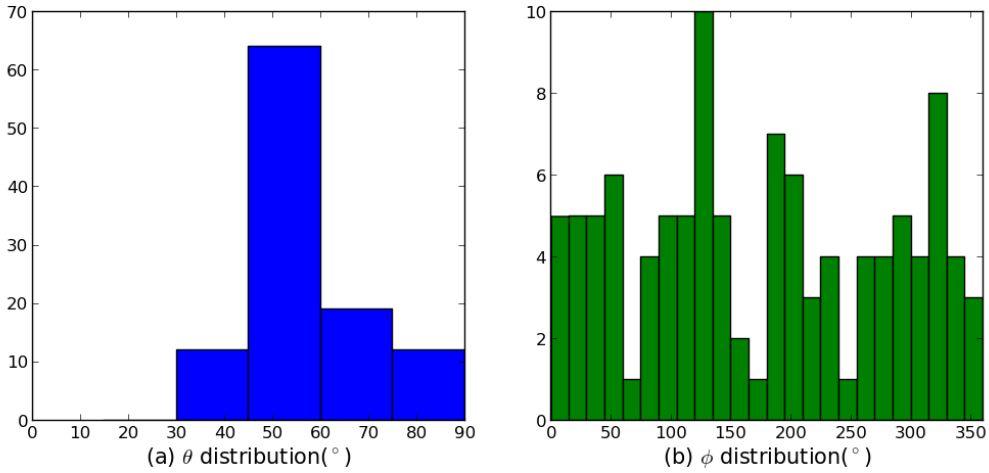

Figure 8.3.: θ (a) and ϕ (b) orientation distributions of DiL molecules embedded in the cell membrane. The θ distribution has a mean of 58° with a standard deviation of 31°

As mentioned in Chapter 5, theoretical and experimental data usually usually have the Dil molecules aligned close to parallel with the lipid bilayer. Molecular Dynamics simulations of Dil molecules in a DPPC bilayer predicted a polar orientation value of $\theta = 77° \pm 13°$.[112]

While the mean value for θ is higher than the value predicted by simulation, the mean value from the simulations falls within one standard deviation of the experimental data. Accounting for the fact that it is highly unlikely that the cell membranes attach to the glass in a perfectly smooth manner with no ripples or deformations, it is reasonable to conclude that the experimental data confirms previous ideas about the orientation of DilC molecules in a cell membrane.

8.2. Summary

We now have a proof of concept experiment showing that it is possible to insert low concentrations of lipophilic dye molecules into the membrane of immobilised calls and, using TIRF on thin-bottomed petri dishes, directly measure the orientation of those molecules in the part of the membrane attached to the glass surface. The measures orientations follow a polar angle distribution of mean $\theta = 58°$, standard deviation = 31°. The predicted orientation of DilC molecules in lipid bilayers obtained my molecular dynamics simulations falls within one standard deviation of the experimentally obtained results, implying that my results are in line with the expected behavior of these fluorophores in cell membranes.

Chapter 9.

Conclusion and Further Work

Owing to the fact that defocused fluorescence measurement is a relatively new microscopy technique, there remain a lot of questions both about its fundamental nature and about possible applications to physical systems that remain to be answered.

The experiments on lipid layers in Chapter 5 showed DilC molecules embedded in lipid layers orient themselves in a very narrow range of polar angles, as expected, but not in the expected range of orientations. The best explanation for this is that the DilC molecules were migrating outside the DPPC bilayer. It would be useful to confirm this and, following on from that, come up with a better means to immobilise DilC molecules by creating the lipid layers in a different manner or on different kind of glass. Once that is done, the next step would be to use the dye molecules to probe the static and dynamic nature of lipid thin films.

It would also be useful to reexamine the polarisation optics attached to the TIRF module in order to achieve a properly circularly polarised beam and thus proper ϕ orientation distribution. Examining differing illumination modes for improving θ orientation would also be worthwhile.

I also experiment with a system for isolating defocused patterns in densely labelled samples and verify it on both dye molecules immobilised in polymer thin films and dye-labelled lipid molecules added to lipid nanostructures created by Dip-Pen Nanolithography (Chapter 6). The average azimuthal orientation of

the dye-labelled lipid molecules seem to strongly imply that the nanostructures align themselves with the direction in which they are written. These findings can be verified via the use of polarisation microscopy. It would be interesting to see if the construction of the lipid nanostructures (thickness of structures, humidity, type of substrate, type of lipid molecules etc.) affects their ordering as probed by embedded dye.

The other interesting proof of concept experiment was in Chapter8 where I showed that defocused fluorescence imaging coupled with TIRF can be used to image single fluorophores embedded in the cell membrane and accurately measure both position and orientation. Since the concept has now been proven, it is now worth applying it first to live cells and then to more complex problems.

In terms of fundamental questions, the simulations performed in Chapter 3 provided some insight into the behaviour of the pattern matching algorithm, under ideal circumstances, and for the addition of a fairly simple noise profile is included (a Poisson distribution with mean $\lambda = 300$) for effective pixel sizes of 50 nm, 100 nm, 150 nm. The results of these simulations were recorded in terms of mean photon count required to fit a pattern with polar angle accuracy ($\pm 5°$)Interestingly enough, there was a fairly substantial difference between the distribution of mean photon count per angle for the ideal and noisy systems. Most importantly for practical purposes, the mean photon count remains almost constant with respect to polar angles and the S/N ratio for an accurate fit in terms of position and orientation is on the order of 5%.

This analysis can be improved by varying the noise level, creating more complicated noise profiles, change the polar angle accuracy, and also examine different physical models (refractive indices, thickness, number of layers, number and relative orientation of emission dipoles) to see if the S/N ratio is an intrinsic feature or varies with some of the parameters. All of these would increase our understanding of the physical limitations of defocused fluorescence.

It is also worth examining the possibility of improving the superresolution localisation process investigated in Chapter 7. One of the ways this could be achieved is by first identifying the best fitting pattern and then fitting a more

general version of the equation and see if that will allow for a more accurate localisation of the centre of the pattern.

In conclusion, there is a massive amount of metrology that can be performed on this technique and probably several ways it can be explored and improved.

Appendix A.

Pattern matching MATLAB code

The MATLAB package works by first calculating what the defocused images will look like for a dipole embedded in a dielectric and at the interface of a different dielectric with surrounding system that has a well-defined geometry and imaged through a well defined system. The geometry of the system is defined using the variables listed below.

`z` The position of the emitter above the bottom of its layer in μm

`NA` The numerical aperture of the objective

`n1` A vector of the refractive indices of the stack below the layer the molecule is embedded in

`n` The refractive index of the layer the molecule is embedded in

`n2` A vector of the refractive indices of the stack above the layer the molecule is embedded in

`d1` A vector of the thickness of the layers below the layer the molecule is embedded in

`d` The thickness of the layer the molecule is embedded in

`d2` A vector of the thickness of the layers above the layer the molecule is embedded in

lamem The emission wavelength in μm

mag The image magnification

focus The distance by which the objective is moved towards the sample in μm

atf The correction vector for for coverslip thickness effects. empty if there are no corrections or a 2 element vector of thickness and deviation in μm

ring Optional parameter for a potential phase plate (default[])

pixel side length of a single detector pixel (μm)

nn Image size is 2*nn+1 $\times$ 2*nn+1 pixels (default = 10)

be_res polar angle increment(default = 10°)

al_res azimuthal angle increment(default = 10°)

pic The calculated images are shown in a figure if this value is nonzero and non-empty (default 0)

After setting the variables, the program then returns a struct called **model** containing three arrays of equal length

model.mask An array of images for the calculated patterns for all possible combinations of molecular orientation

model.theta An array of polar angles corresponding to the polar angles of the images

model.phi An array of azimuthal angles corresponding to the polar angles of the images

The next step is to import the image file to be examined and pass that to the MATLAB package along with the stack of calculated images (model.mask) a support matrix unmasking the parts of the image that shall be occupied by the patterns(in this case, a circle) represented by **sup** and a background matrix (**bck**, usually the same as **sup**) used to compensate for any background noise that may be present in the image.

The output shall be:

`len` A variable representing the number of matched patterns

`sc` An array containing an index matching the pattern to the image and orientation of the generated patterns

`xc, yc` An array representing the x- and y-coordinates of the detected patterns

`err` An image of the least squares error. It is used to generate an array of error values for each recognized pattern

`imm` A reconstructed image replacing the matched patterns with their calculated values

After pattern recognition has been completed, a custom MATLAB script is used to save a text file with tab-separated values containing the number of patterns, xc,yc,θ,ϕ and the error. An example of the structure of the data file can be found in Figure A.1.

count	x_coord	y_coord	theta	phi	error
1	277	243	30	100	0.007
2	279	238	70	328	0.005
3	358	412	50	157	0.002
4	430	262	85	285	0.01

Figure A.1.: An example of the structure of the data file generated when matching a defocused pattern image file

For image sequences, a different file was generated for each frame. Data analysis was then performed by reading the text files and manipulating the values in them using either MATLAB or Python.

Appendix B.

Analysing Simulation Results

The simulations performed in Chapter 3 were all performed in the same manner. The MATLAB pattern generation program produced predicted patterns in 10° degree intervals of θ and ϕ. The intensity distribution on the predicted pattern was then used to generate a 2D matrix was where every pixel was assigned a probability relative to the brightness of that pixel in the original image. A thousand random numbers were then generated and the pixel corresponding to each random number was incremented by one. The resulting image was then compared to the patterns in the library. If the pattern matched the central pixel and the orientation, the simulation ended. If not, another thousand photons were added to the random image and pattern matching was performed again until the right fit was achieved.

Theta = 10	Phi = 300				
photons	x_coord	y_coord	theta	phi	error
1000	17	16	20	210	0.007
2000	16	17	20	90	0.009
3000	16	16	10	300	0.001

Figure B.1.: An example of the structure of the data file generated when matching a randomly generated defocused pattern

Each randomly generated image was given its own tab-separated text file with the same structure as Figure B.1. The first line of the file was a header line with the

θ and ϕ values of the pattern that the probability matrix was based on. For each thousand photons, the number of photons, the central pixel x- and y-coordinates and the best fit orientation and the goodness of fit were recorded. Once a fit for position and orientation was found, the file was closed, a new file was opened a new probability grid generated and the entire process was repeated.

Once the simulations were done, what remained was a folder full of text files that could be processed to provide information about the strengths of defocused orientation imaging.

List of figures

Bibliography

[1] G. Stokes, "On the change of refrangibility of light," *Philosophical Transactions of the Royal Society of . . .*, vol. 143, no. Ii, pp. 385–396, 1852.

[2] B. Valeur, *Molecular Fluorescence: Principles and Applications*, vol. 8. Wiley-VCH, 2001.

[3] Wikipedia, "Fluorescence Microscopy," 2012. [Online; accessed 03-January-2013].

[4] L. a Bagatolli and E. Gratton, "Two photon fluorescence microscopy of coexisting lipid domains in giant unilamellar vesicles of binary phospholipid mixtures.," *Biophysical journal*, vol. 78, pp. 290–305, Jan. 2000.

[5] J. R. Lakowicz and B. R. Masters, *Principles of Fluorescence Spectroscopy, Third Edition*, vol. 13. Springer, 2008.

[6] P. Suppan, *Chemistry and light*. Cambridge: Royal Society of Chemistry, 1994.

[7] A. Gilbert and J. Baggott, *Essentials of Molecular Photochemistry*. CRC Press, 1991.

[8] W. Moerner and L. Kador, "Optical detection and spectroscopy of single molecules in a solid," *Physical Review Letters*, vol. 62, no. 21, pp. 2535–2538, 1989.

[9] M. Orrit and J. Bernard, "Single pentacene molecules detected by fluorescence excitation in a p-terphenyl crystal," *Physical Review Letters*, vol. 65, pp. 2716–2719, Nov. 1990.

[10] S. Nie, D. T. Chiu, and R. N. Zare, "Probing individual molecules with

confocal fluorescence microscopy," *Science*, vol. 266, pp. 1018–1021, Nov. 1994.

[11] D. Patra, "Application and New Developments in Fluorescence Spectroscopic Techniques in Studying Individual Molecules," *Applied Spectroscopy Reviews*, vol. 43, pp. 389–415, Sept. 2008.

[12] B. Moomaw, "Camera Technologies for Low Light Imaging : Overview and Relative Advantages," *Cell*, vol. 81, no. 06, pp. 251–283, 2007.

[13] J. Hohlbein, K. Gryte, M. Heilemann, and A. N. Kapanidis, "Surfing on a new wave of single-molecule fluorescence methods.," *Physical biology*, vol. 7, p. 031001, Jan. 2010.

[14] G. Schütz, H. Gruber, H. Schindler, and T. Schmidt, "Fluorophores for single molecule microscopy," *Journal of luminescence*, vol. 72, pp. 18–21, 1997.

[15] C. Joo, H. Balci, Y. Ishitsuka, C. Buranachai, and T. Ha, "Advances in single-molecule fluorescence methods for molecular biology.," *Annual review of biochemistry*, vol. 77, pp. 51–76, Jan. 2008.

[16] M. Böhmer and J. Enderlein, "Fluorescence Spectroscopy of Single Molecules under Ambient Conditions: Methodology and Technology," *ChemPhysChem*, vol. 4, pp. 792–808, Aug. 2003.

[17] E. Braeken, A. Deres, F. C. D. Schryver, H. Uji-i, J. Hofkens, D. Wöll, and F. C. De Schryver, "Polymers and single molecule fluorescence spectroscopy, what can we learn?," *Chemical Society reviews*, vol. 38, pp. 313–28, Feb. 2009.

[18] G. Hinze, T. Basché, R. a L Vallée, and R. A. L. Valle, "Single molecule probing of dynamics in supercooled polymers.," *Physical chemistry chemical physics : PCCP*, vol. 13, pp. 1813–8, Feb. 2011.

[19] W. E. Moerner and M. Orrit, "Illuminating Single Molecules in Condensed Matter," *Science*, vol. 283, pp. 1670–1676, Mar. 1999.

[20] M. Heilemann, "Fluorescence microscopy beyond the diffraction limit.," *Journal of biotechnology*, vol. 149, pp. 243–51, Sept. 2010.

[21] J. A. Veerman, S. A. Levi, F. C. J. M. V. Veggel, D. N. Reinhoudt, and N. F. V. Hulst, "Near-Field Scanning Optical Microscopy of Single Fluorescent Dendritic Molecules," *Molecules*, pp. 11264–11270, 1999.

[22] W. E. Moerner, "A dozen years of single-molecule spectroscopy in physics, chemistry, and biophysics," *The Journal of Physical Chemistry B*, vol. 106, pp. 910–927, Feb. 2002.

[23] N. Walter, C. Huang, A. Manzo, and M. Sobhy, "Do-it-yourself guide: how to use the modern single-molecule toolkit," *Nature methods*, vol. 5, no. 6, pp. 475–489, 2008.

[24] X. Michalet and S. Weiss, "Single-molecule spectroscopy and microscopy," *Comptes Rendus Physique*, vol. 3, pp. 619–644, Jan. 2002.

[25] M. Böhmer, J. Enderlein, and M. Bo, "Orientation imaging of single molecules by wide-field epifluorescence microscopy," *Journal of the Optical Society of America B*, vol. 20, no. 3, p. 554, 2003.

[26] P. Dedecker, A. Deres, H. Uji-i, J. ichi Hotta, M. Sliwa, J. philippe Jean-phillipe Jean-Philippe Soumillion, M. Klaus, J. J. Enderlein, B. Muls, K. Müllen, J. Hofkens, B. P. Dedecker, and K. Mu, "Defocused Wide-field Imaging Unravels Structural and Temporal Heterogeneity in Complex Systems," *Advanced Materials*, vol. 21, pp. 1–8, Mar. 2009.

[27] D. Patra, I. Gregor, and J. J. Enderlein, "Image Analysis of Defocused Single-Molecule Images for Three-Dimensional Molecule Orientation Studies," *The Journal of Physical Chemistry A*, vol. 108, pp. 6836–6841, Aug. 2004.

[28] H. U. i Ania, D. Benoit, and M. Sergey, "Defocused Imaging in Wide-field Fluorescence Microscopy," *Fluorescence of Supermolecules Polymers and Nanosystems*, no. September 2007, pp. 257–284, 2008.

[29] H. Uji-i, S. M. Melnikov, A. Deres, G. Bergamini, F. De Schryver, A. Herrmann, K. Müllen, J. Enderlein, J. Hofkens, F. D. Schryver, and K. Mu, "Visualizing spatial and temporal heterogeneity of single molecule rotational diffusion in a glassy polymer by defocused wide-field imaging," *Polymer*,

vol. 47, pp. 2511–2518, Mar. 2006.

[30] A. Deres, G. a. Floudas, K. Müllen, M. Van der Auweraer, F. De Schryver, J. Enderlein, H. Uji-i, and J. Hofkens, "The Origin of Heterogeneity of Polymer Dynamics near the Glass Temperature As Probed by Defocused Imaging," *Macromolecules*, vol. 44, pp. 9703–9709, Dec. 2011.

[31] S. Ito, T. Kusumi, H. Miyasaka, and S. Takei, "Diffusion processes of single fluorescent molecules in a polymer-based thin material with three-dimensional network.," *Chemical communications (Cambridge, England)*, pp. 6165–7, Nov. 2009.

[32] H. Aoki, T. Takahashi, and S. Ito, "Segmental orientation of a single polymer chain in Langmuir–Blodgett films studied by defocus fluorescence imaging," *Polymer Journal*, vol. 43, pp. 218–221, Dec. 2010.

[33] Z. Zheng, F. Kuang, and J. Zhao, "Direct Observation of Rotational Motion of Fluorophores Chemically Attached to Polystyrene in Its Thin Films," *Macromolecules*, vol. 43, pp. 3165–3168, Apr. 2010.

[34] K. P. Ghiggino, T. D. M. Bell, and E. N. Hooley, "Synthetic polymers for solar harvesting," *Faraday Discussions*, vol. 155, p. 79, 2012.

[35] J. Taguchi, T. Yano, S. Habuchi, M. Vacha, and S. Shibata, "Control of orientation of rhodamine 6G in organic–inorganic hybrid film by capillary electrophoresis doping technique," *Thin Solid Films*, vol. 519, pp. 6106–6109, July 2011.

[36] P. W. Livanec and R. C. Dunn, "Single-molecule probes of lipid membrane structure.," *Langmuir : the ACS journal of surfaces and colloids*, vol. 24, pp. 14066–73, Dec. 2008.

[37] P. W. Livanec, H. a Huckabay, and R. C. Dunn, "Exploring the effects of sterols in model lipid membranes using single-molecule orientations.," *The journal of physical chemistry. B*, vol. 113, pp. 10240–8, July 2009.

[38] H. a Huckabay and R. C. Dunn, "Hydration Effects on Membrane Structure

Probed by Single Molecule Orientations.," *Langmuir : the ACS journal of surfaces and colloids*, pp. 2658–2666, Feb. 2011.

[39] P. W. Livanec, H. a. Huckabay, and R. C. Dunn, "Reduced single molecule photobleaching in fumed Langmuir–Blodgett films," *Thin Solid Films*, vol. 520, pp. 6233–6237, July 2012.

[40] H. Park, E. Toprak, and P. R. Selvin, "Single-molecule fluorescence to study molecular motors.," *Quarterly reviews of biophysics*, vol. 40, pp. 87–111, Feb. 2007.

[41] J. G. Reifenberger, E. Toprak, H. Kim, D. Safer, H. L. Sweeney, and P. R. Selvin, "Myosin VI undergoes a 180 degrees power stroke implying an uncoupling of the front lever arm.," *Proceedings of the National Academy of Sciences of the United States of America*, vol. 106, pp. 18255–60, Oct. 2009.

[42] E. Toprak, J. Enderlein, S. Syed, S. a Mckinney, R. G. Petschek, T. Ha, Y. E. Goldman, and P. R. Selvin, "Defocused orientation and position imaging (DOPI) of myosin V.," *Proceedings of the National Academy of Sciences of the United States of America*, vol. 103, pp. 6495–9, Apr. 2006.

[43] S. Syed, G. E. Snyder, C. Franzini-armstrong, P. R. Selvin, Y. E. Goldman, and R. Selvin, "Adaptability of myosin V studied by simultaneous detection of position and orientation.," *The EMBO journal*, vol. 25, pp. 1795–803, May 2006.

[44] S. M. Melnikov, E. K. L. Yeow, H. Uji-i, M. Cotlet, K. Müllen, F. C. De Schryver, J. Enderlein, J. Hofkens, K. Mu, and F. C. D. Schryver, "Origin of simultaneous donor-acceptor emission in single molecules of peryleneimide-terrylenediimide labeled polyphenylene dendrimers.," *The journal of physical chemistry. B*, vol. 111, pp. 708–19, Feb. 2007.

[45] D. Patra, I. Gregor, J. Enderlein, M. Sauer, and D-Jülich, "Defocused imaging of quantum-dot angular distribution of radiation," *Applied Physics Letters*, vol. 87, no. 10, p. 101103, 2005.

[46] R. Schuster, M. Barth, A. Gruber, and F. Cichos, "Defocused wide field

fluorescence imaging of single CdSe/ZnS quantum dots," *Chemical Physics Letters*, vol. 413, pp. 280–283, Sept. 2005.

[47] X.-J. Chen, Y. Xu, S. Lan, Q. feng Dai, X.-S. Lin, Q. Guo, and L.-J. Wu, "Rotation of defocused wide-field fluorescence images after blinking in single CdSe/ZnS core-shell quantum dots," *Physical Review B*, vol. 79, pp. 1–6, Mar. 2009.

[48] T. Li, Q. Li, Y. Xu, X.-J. Chen, Q.-F. Dai, H. Liu, S. Lan, S. Tie, and L.-J. Wu, "Three-dimensional orientation sensors by defocused imaging of gold nanorods through an ordinary wide-field microscope.," *ACS nano*, vol. 6, pp. 1268–77, Feb. 2012.

[49] J. W. Ha, K. Marchuk, and N. Fang, "Focused orientation and position imaging (FOPI) of single anisotropic plasmonic nanoparticles by total internal reflection scattering microscopy.," *Nano letters*, vol. 12, pp. 4282–8, Aug. 2012.

[50] A. Cyphersmith, A. Maksov, K. D. Mccarthy, and M. D. Barnes, "Defocused Emission Patterns from Chiral Fluorophores : Application to Chiral Axis Orientation Determination," *Simulation*, pp. 661–665, 2011.

[51] D. Axelrod, "Carbocyanine dye orientation in red cell membrane studied by microscopic fluorescence polarization.," *Biophysical journal*, vol. 26, pp. 557–73, June 1979.

[52] C. Reznik, N. Estillore, R. C. Advincula, and C. F. Landes, "Single molecule spectroscopy reveals heterogeneous transport mechanisms for molecular ions in a polyelectrolyte polymer brush.," *The journal of physical chemistry. B*, vol. 113, pp. 14611–8, Nov. 2009.

[53] L. Deschenes and D. Bout, "Heterogeneous dynamics and domains in supercooled o-terphenyl: A single molecule study," *The Journal of Physical Chemistry B*, vol. 106, no. 44, pp. 11438–11445, 2002.

[54] L. a Deschenes and D. a Vanden Bout, "Molecular motions in polymer films near the glass transition: a single molecule study of rotational dynamics.,"

The journal of physical chemistry. B, vol. 110, p. 9362, May 2006.

[55] R. Zondervan, F. Kulzer, G. C. G. Berkhout, and M. Orrit, "Local viscosity of supercooled glycerol near Tg probed by rotational diffusion of ensembles and single dye molecules.," *Proceedings of the National Academy of Sciences of the United States of America*, vol. 104, pp. 12628–33, July 2007.

[56] J. N. Forkey, M. E. Quinlan, M. A. Shaw, J. E. T. Corrie, and Y. E. Goldman, "Three-dimensional structural dynamics of myosin V by single-molecule fluorescence polarization.," *Nature*, vol. 422, pp. 399–404, Mar. 2003.

[57] H. Sosa, E. J. G. Peterman, W. E. Moerner, and L. S. B. Goldstein, "letters ADP-induced rocking of the kinesin motor domain revealed by single- molecule fluorescence polarization microscopy," *Group*, vol. 8, no. 6, pp. 6–10, 2001.

[58] C. yaung Lu, D. a Vanden Bout, and D. A. Vanden, "Analysis of orientational dynamics of single fluorophore trajectories from three-angle polarization experiments.," *The Journal of chemical physics*, vol. 128, p. 244501, June 2008.

[59] J. T. Fourkas, "Rapid determination of the three-dimensional orientation of single molecules.," *Optics letters*, vol. 26, pp. 211–3, Feb. 2001.

[60] I. Chung, K. T. Shimizu, and M. G. Bawendi, "Room temperature measurements of the 3D orientation of single CdSe quantum dots using polarization microscopy.," *Proceedings of the National Academy of Sciences of the United States of America*, vol. 100, pp. 405–8, Jan. 2003.

[61] J. Hohlbein and C. G. HuÌĹbner, "Simple scheme for rapid three-dimensional orientation determination of the emission dipole of single molecules," *Applied Physics Letters*, vol. 86, no. 12, pp. 1–3, 2005.

[62] J. Hohlbein and C. G. Hübner, "Three-dimensional orientation determination of the emission dipoles of single molecules: the shot-noise limit.," *The Journal of chemical physics*, vol. 129, p. 094703, Sept. 2008.

[63] M. M. R. Foreman, C. M. C. Romero, and P. Török, "Determination of the three-dimensional orientation of single molecules," *Optics letters*, vol. 33,

no. 9, pp. 1020–1022, 2008.

[64] M. R. Foreman and P. Török, "Fundamental limits in single-molecule orientation measurements," *New Journal of Physics*, vol. 13, p. 093013, Sept. 2011.

[65] Z. Sikorski and L. M. Davis, "Engineering the collected field for single-molecule orientation determination.," *Optics express*, vol. 16, pp. 3660–73, Mar. 2008.

[66] C.-Y. J. Wei, C. yaung Lu, Y. H. Kim, D. a Vanden Bout, and D. A. V. Bout, "Determining if a system is heterogeneous: the analysis of single molecule rotational correlation functions and their limitations.," *Journal of fluorescence*, vol. 17, pp. 797–804, Nov. 2007.

[67] P. Dedecker, B. Muls, J. Hofkens, J. Enderlein, and J. ichi Hotta, "Orientational effects in the excitation and de-excitation of single molecules interacting with donut-mode laser beams," *Optics Express*, vol. 15, no. 6, p. 3372, 2007.

[68] B. Sick, B. Hecht, and L. Novotny, "Orientational imaging of single molecules by annular illumination," *Physical review letters*, vol. 85, pp. 4482–5, Nov. 2000.

[69] H. Ishitobi, T. Kai, K. Fujita, Z. Sekkat, and S. Kawata, "On fluorescence blinking of single molecules in polymers," *Chemical Physics Letters*, vol. 468, pp. 234–238, Jan. 2009.

[70] H. Ishitobi, I. Nakamura, N. Hayazawa, Z. Sekkat, and S. Kawata, "Orientational imaging of single molecules by using azimuthal and radial polarizations.," *The journal of physical chemistry. B*, vol. 114, pp. 2565–71, Mar. 2010.

[71] R. M. Dickson, D. J. Norris, and W. E. Moerner, "Simultaneous Imaging of Individual Molecules Aligned Both Parallel and Perpendicular to the Optic Axis," *Physical Review Letters*, vol. 81, pp. 5322–5325, Dec. 1998.

[72] A. P. Bartko and R. M. Dickson, "Three-Dimensional Orientations of Polymer-Bound Single Molecules," *The Journal of Physical Chemistry B*, vol. 103, pp. 3053–3056, Apr. 1999.

[73] A. P. Bartko and R. M. Dickson, "Imaging Three-Dimensional Single Molecule Orientations," *The Journal of Physical Chemistry B*, vol. 103, pp. 11237–11241, Dec. 1999.

[74] A. P. Bartko, K. Xu, and R. M. Dickson, "Three-Dimensional Single Molecule Rotational Diffusion in Glassy State Polymer Films," *Physical Review Letters*, vol. 89, pp. 1–4, June 2002.

[75] M. a Osborne, "Real-time dipole orientational imaging as a probe of ligand-protein interactions.," *The journal of physical chemistry. B*, vol. 109, pp. 18153–61, Sept. 2005.

[76] M. A. Lieb, J. M. Zavislan, and L. Novotny, "Single-molecule orientations determined by direct emission pattern imaging," *Journal of the Optical Society of America B*, vol. 21, no. 6, p. 1210, 2004.

[77] W. Lukosz, "Light emission by magnetic and electric dipoles close to a plane dielectric interface. II. Radiation patterns of perpendicular oriented dipoles," *JOSA*, pp. 1615–1619, 1977.

[78] W. Lukosz and R. E. Kunz, "Light emission by magnetic and electric dipoles close to a plane interface I Total radiated power," *Journal of the Optical Society of America*, vol. 67, p. 1607, Dec. 1977.

[79] W. Lukosz, "Light emission by magnetic and electric dipoles close to a plane dielectric interface III Radiation patterns of dipoles with arbitrary orientation," *Journal of the Optical Society of America*, vol. 69, p. 1495, Nov. 1979.

[80] J. Enderlein, T. Ruckstuhl, and S. Seeger, "Highly efficient optical detection of surface-generated fluorescence.," *Applied optics*, vol. 38, pp. 724–32, Feb. 1999.

[81] O. Letters and J. Enderlein, "Theoretical study of detection of a dipole emitter through an objective with high numerical aperture.," *Optics letters*, vol. 25, pp. 634–6, May 2000.

[82] J. J. Enderlein, "Electrodynamics of Fluorescence," pp. 1–32, 2003.

[83] E. H. Hellen and D. Axelrod, "Fluorescence emission at dielectric and metal-film interfaces," *Journal of the Optical Society of America B*, vol. 4, p. 337, Mar. 1987.

[84] A. B. Richards and E. Wolf, "Electromagnetic Diffraction in Optical Systems . II . Structure of the Image Field in an Electromagnetic diffraction in optical systems II . Structure of the image field in an aplanatic system," *Structure*, vol. 253, no. 1274, pp. 358–379, 2009.

[85] M. R. Foreman, S. S. Sherif, T. Peter, and P. Török, "Photon statistics in single molecule orientational imaging.," *Optics express*, vol. 15, pp. 13597–606, Oct. 2007.

[86] A. V. Abraham, S. Ram, J. Chao, E. S. Ward, and R. J. Ober, "Quantitative study of single molecule location estimation techniques.," *Optics express*, vol. 17, pp. 23352–73, Dec. 2009.

[87] R. J. Ober, S. Ram, and E. S. Ward, "Localization Accuracy in Single-Molecule Microscopy," *Biophysical Journal*, vol. 86, no. 2, pp. 1185–1200, 2004.

[88] R. E. Thompson, D. R. Larson, and W. W. Webb, "Precise Nanometer Localization Analysis for Individual Fluorescent Probes," *Biophysical Journal*, vol. 82, pp. 2775–2783, May 2002.

[89] J. J. Enderlein, E. Toprak, and P. R. Selvin, "Polarization effect on position accuracy of fluorophore localization.," *Optics express*, vol. 14, pp. 8111–20, Sept. 2006.

[90] K. B. W. Harpsoe, M. I. Andersen, and P. Kjægaard, "Bayesian Photon Counting with EMCCDs," *Astronomy & Astrophysics*, pp. 1–11, 2011.

[91] D. Nečas and P. Klapetek, "Gwyddion: an open-source software for SPM

data analysis," *Central European Journal of Physics*, vol. 10, Nov. 2011.

[92] M. D. Abramoff, P. J. Magelhaes, and S. J. Ram, "Image Processing with ImageJ," *Biophotonics International*, vol. 11, no. 7, pp. 36–42, 2004.

[93] J. Hunter, "Matplotlib: A 2D graphics environment," *Computing in Science & Engineering*, pp. 90–95, 2007.

[94] D. B. Hall, P. Underhill, and J. M. Torkelson, "Spin coating of thin and ultrathin polymer films," *Polymer Engineering & Science*, vol. 38, pp. 2039–2045, Dec. 1998.

[95] C. B. Walsh and E. I. Franses, "Ultrathin PMMA films spin-coated from toluene solutions," *Thin Solid Films*, vol. 429, pp. 71–76, Apr. 2003.

[96] S. Habuchi, T. Oba, and M. Vacha, "Multi-beam single-molecule defocused fluorescence imaging reveals local anisotropic nature of polymer thin films.," *Physical chemistry chemical physics : PCCP*, vol. 13, pp. 7001–7, Apr. 2011.

[97] E. Hecht, *Optics 4th edition*, vol. 1. Addison Wesley, 2001.

[98] S. Lord, H. Lee, and W. Moerner, "Single-molecule spectroscopy and imaging of biomolecules in living cells," *Analytical chemistry*, vol. 82, no. 6, pp. 2192–2203, 2010.

[99] O. Maier, V. Oberle, and D. Hoekstra, "Fluorescent lipid probes: some properties and applications (a review).," *Chemistry and physics of lipids*, vol. 116, pp. 3–18, June 2002.

[100] Z. V. Leonenko, a Carnini, and D. T. Cramb, "Supported planar bilayer formation by vesicle fusion: the interaction of phospholipid vesicles with surfaces and the effect of gramicidin on bilayer properties using atomic force microscopy.," *Biochimica et biophysica acta*, vol. 1509, pp. 131–47, Dec. 2000.

[101] Z. V. Leonenko, E. Finot, H. Ma, T. E. S. Dahms, and D. T. Cramb, "Investigation of temperature-induced phase transitions in DOPC and DPPC phospholipid bilayers using temperature-controlled scanning force microscopy.," *Biophysical journal*, vol. 86, pp. 3783–93, June 2004.

[102] P. Shushkov, S. Tzvetanov, M. Velinova, A. Ivanova, and A. Tadjer, "Structural aspects of lipid monolayers: computer simulation analyses.," *Langmuir : the ACS journal of surfaces and colloids*, vol. 26, pp. 8081–92, June 2010.

[103] M. Pasenkiewicz-Gierula, "Structure and Dynamics of lipid bilayer membranes - Comparison of EPR and Molecular Dynamics Simulation results," *Curr. Top. Biophys*, 1996.

[104] M. M. Lapinski and G. J. Blanchard, "The role of phospholipid headgroups in mediating bilayer organization. Perturbations induced by the presence of a tethered chromophore.," *Chemistry and physics of lipids*, vol. 150, pp. 12–21, Nov. 2007.

[105] J. Oreopoulos and C. M. Yip, "Combined scanning probe and total internal reflection fluorescence microscopy.," *Methods (San Diego, Calif.)*, vol. 46, pp. 2–10, Sept. 2008.

[106] K. Kachel, E. Asuncion-Punzalan, and E. London, "The location of fluorescence probes with charged groups in model membranes.," *Biochimica et biophysica acta*, vol. 1374, pp. 63–76, Sept. 1998.

[107] R. a Badley, W. G. Martin, and H. Schneider, "Dynamic behavior of fluorescent probes in lipid bilayer model membranes.," *Biochemistry*, vol. 12, pp. 268–275, Jan. 1973.

[108] G. B. Melikyan, B. N. Deriy, D. C. Ok, and F. S. Cohen, "Voltage-dependent translocation of R18 and DiI across lipid bilayers leads to fluorescence changes," *Biophysical journal*, vol. 71, pp. 2680–2691, Dec. 1996.

[109] G. J. Schutz, W. Baumgartner, H. J. Gruber, and H. Schindler, "Characterization of Photophysics and Mobility of Single Molecules in a Fluid Lipid Membrane," pp. 17662–17668, 1995.

[110] M. G. Honig and R. I. Hume, "Dil and diO: versatile fluorescent dyes for neuronal labelling and pathway tracing.," *Trends in neurosciences*, vol. 12, pp. 333–5, 340–1, Sept. 1989.

[111] R. R. Gullapalli, C. Demirel, P. J. Butler, and M. C. Demirel, "Molecular dynamics simulations of DiI-C18(3) in a DPPC lipid bilayer.," *Physical chemistry chemical physics : PCCP*, vol. 10, pp. 3548–60, June 2008.

[112] H. S. Muddana, R. R. Gullapalli, E. Manias, P. J. Butler, and D. A. Links, "Atomistic simulation of lipid and DiI dynamics in membrane bilayers under tension.," *Physical chemistry chemical physics : PCCP*, vol. 13, pp. 1368–78, Jan. 2011.

[113] P. D. Simonson, E. Rothenberg, and P. R. Selvin, "Single-molecule-based super-resolution images in the presence of multiple fluorophores.," *Nano letters*, vol. 11, pp. 5090–6, Nov. 2011.

[114] S. Lenhert, P. Sun, Y. Wang, H. Fuchs, and C. A. Mirkin, "Massively parallel dip-pen nanolithography of heterogeneous supported phospholipid multilayer patterns.," *Small (Weinheim an der Bergstrasse, Germany)*, vol. 3, pp. 71–5, Jan. 2007.

[115] R. D. Piner, J. Zhu, F. Xu, and S. Hong, ""Dip-Pen" Nanolithography," *Science*, vol. 283, no. January, pp. 661–663, 1999.

[116] S. Lenhert, F. Brinkmann, T. Laue, S. Walheim, C. Vannahme, S. Klinkhammer, M. Xu, S. Sekula, T. Mappes, T. Schimmel, and H. Fuchs, "Lipid multilayer gratings.," *Nature nanotechnology*, vol. 5, pp. 275–9, Apr. 2010.

[117] A. Kyrychenko, "A molecular dynamics model of rhodamine-labeled phospholipid incorporated into a lipid bilayer," *Chemical Physics Letters*, vol. 485, pp. 95–99, Jan. 2010.

[118] D. Setiawan, A. Kazaryan, M. A. Martoprawiro, and M. Filatov, "A first principles study of fluorescence quenching in rhodamine B dimers: how can quenching occur in dimeric species?," *Physical chemistry chemical physics : PCCP*, vol. 12, pp. 11238–44, Oct. 2010.

[119] D. Axelrod, "Cell-substrate contacts illuminated by total internal reflection fluorescence.," *The Journal of cell biology*, vol. 89, pp. 141–5, Apr. 1981.

[120] D. Dussault, "Noise performance comparison of ICCD with CCD and EM-CCD cameras," *Proceedings of SPIE*, 2004.

[121] L. Novotny, M. R. Beversluis, K. S. Youngworth, and T. G. Brown, "Longitudinal Field Modes Probed by Single Molecules," *Physical Review Letters*, vol. 86, pp. 5251–5254, June 2001.

[122] S. Habuchi, T. Oba, and M. Vacha, "Multi-beam single-molecule defocused fluorescence imaging reveals local anisotropic nature of polymer thin films.," *Physical chemistry chemical physics : PCCP*, vol. 13, pp. 7001–7, Apr. 2011.

[123] M. Vacha and M. Kotani, "Three-dimensional orientation of single molecules observed by far- and near-field fluorescence microscopy," *The Journal of Chemical Physics*, vol. 118, no. 12, p. 5279, 2003.

[124] V. Sample, R. H. R. Newman, and J. Zhang, "The structure and function of fluorescent proteins," *Chem. Soc. Rev.*, vol. 38, pp. 2852–64, Oct. 2009.

[125] A. Debarre, R. Jaffiol, C. Julien, and D. Nutarelli, "Quantitative determination of the 3D dipole orientation of single molecules," *The European Physical*, vol. 77, pp. 67–77, 2004.

[126] A. E. Wolf, E. WolfJ, and E. Wolf, "Electromagnetic diffraction in optical systems. I. An integral representation of the image field," *Proceedings of the Royal Society of*, vol. 253, pp. 349–357, Dec. 1959.

[127] D. L. Snyder, C. W. Helstrom, A. D. Lanterman, M. Faisal, and R. L. White, "Compensation for readout noise in CCD images," *Journal of the Optical Society of America A*, vol. 12, p. 272, Feb. 1995.

[128] M. Hashimoto, K. Yamada, and T. Araki, "Proposition of Single Molecular Orientation Determination Using polarization Controlled Beam by Liquid Crystal Spatial Light Modulators," *Optical Review*, vol. 12, pp. 37–41, Jan. 2005.

[129] D. Nishimura, Y. Takashima, H. Aoki, T. Takahashi, H. Yamaguchi, S. Ito, and A. Harada, "Single-molecule imaging of rotaxanes immobilized on

glass substrates: observation of rotary movement.," *Angewandte Chemie (International ed. in English)*, vol. 47, pp. 6077–9, Jan. 2008.

[130] K. A. Lidke, B. Rieger, D. S. Lidke, and T. M. Jovin, "The Role of Photon Statistics in Fluorescence Anisotropy Imaging," *Image (Rochester, N.Y.)*, vol. 14, no. 9, pp. 1237–1245, 2005.

[131] A. Anantharam, B. Onoa, R. H. Edwards, R. W. Holz, and D. Axelrod, "Localized topological changes of the plasma membrane upon exocytosis visualized by polarized TIRFM.," *The Journal of cell biology*, vol. 188, pp. 415–28, Feb. 2010.

[132] J. R. Swedlow and M. Platani, "Live Cell Imaging Using Wide-Field Microscopy and Deconvolution Cell engineering for in vivo fluorescence imaging," *Cell Structure and Function*, vol. 341, no. 5, pp. 335–341, 2002.

[133] B. Richards and E. Wolf, "Electromagnetic diffraction in optical systems. II. Structure of the image field in an aplanatic system," *Proceedings of the Royal*, 1959.

[134] S. Geissb, M. Iwan, T. Lasser, F. Aguet, S. Geissbühler, I. Märki, and M. Unser, "Super-resolution orientation estimation and localization of fluorescent dipoles using 3-D steerable filters," *Optics Express*, vol. 17, p. 6829, Apr. 2009.

[135] T. P. Burghardt, M. P. Josephson, and K. Ajtai, "Single myosin cross-bridge orientation in cardiac papillary muscle detects lever-arm shear strain in transduction.," *Biochemistry*, vol. 50, pp. 7809–21, Sept. 2011.

[136] H. Piwonski, a. Hartschuh, N. Urbanska, H. Piwoński, N. Urbańska, M. Pietraszkiewicz, J. Sepioł, a. J. Meixner, and J. Waluk, "Polarized Spectroscopy Studies of Single Molecules of Porphycenes: Tautomerism and Orientation âĂă," *The Journal of*, vol. 113, pp. 11514–11519, July 2009.

[137] W. E. Moerner and D. P. Fromm, "Methods of single-molecule fluorescence spectroscopy and microscopy," *Review of Scientific Instruments*, vol. 74, no. 8, p. 3597, 2003.

[138] S. E. Sund, J. A. Swanson, and D. Axelrod, "Cell membrane orientation visualized by polarized total internal reflection fluorescence.," *Biophysical journal*, vol. 77, pp. 2266–83, Oct. 1999.

[139] X. Wang, S. Chang, L. Lin, L. Wang, and S. Hao, "Elimination of fluorescence intensity difference in orientation determination of single molecules by highly focused generalized cylindrical vector beams," *Optik - International Journal for Light and Electron Optics*, vol. 122, pp. 773–776, July 2010.

[140] J. Enderlein and M. Böhmer, "Influence of interface-dipole interactions on the efficiency of fluorescence light collection near surfaces.," *Optics letters*, vol. 28, pp. 941–3, June 2003.

[141] I. Rasnik, T. French, K. Jacobson, and K. Berland, "Electronic Cameras for Low-Light Microscopy," *Cell*, vol. 81, no. 06, pp. 219–249, 2007.

[142] K. R. Spring, "Cameras for Digital Microscopy," *Cell*, vol. 81, no. 06, pp. 171–186, 1998.

[143] a. Mehta, P. Kumar, M. D. Dadmun, J. Zheng, R. M. Dickson, T. Thundat, B. G. Sumpter, and M. D. Barnes, "Oriented Nanostructures from Single Molecules of a Semiconducting Polymer: Polarization Evidence for Highly Aligned Intramolecular Geometries," *Nano Letters*, vol. 3, pp. 603–607, May 2003.

[144] M. R. Hammond, R. J. Kline, A. A. Herzing, L. J. Richter, D. S. Germack, H.-W. Ro, C. L. Soles, D. a Fischer, T. Xu, L. Yu, M. F. Toney, and D. M. Delongchamp, "Molecular order in high-efficiency polymer/fullerene bulk heterojunction solar cells.," *ACS nano*, vol. 5, pp. 8248–57, Oct. 2011.

[145] G. J. Schütz, M. Sonnleitner, P. Hinterdorfer, H. Schindler, and G. Schutz, "Single molecule microscopy of biomembranes (review).," *Molecular membrane biology*, vol. 17, no. 1, pp. 17–29, 2000.

[146]